

On the neutral gas puff as a tokamak edge diagnostic

A THESIS SUBMITTED TO THE DEPARTMENT OF PHYSICS
OF THE UNIVERSITY OF STRATHCLYDE
FOR THE DEGREE OF DOCTOR OF PHILOSOPHY.

Iain D. Paton

October 2005

© Copyright 2005

The copyright of this thesis belongs to the author under the terms of the United Kingdom Copyright Acts as qualified by University of Strathclyde Regulation 3.51. Due acknowledgement must always be made of the use of any material contained in, or derived from, this thesis.

Research Supervisor: Prof. Hugh Summers
Department of Physics
University of Strathclyde
Glasgow, G4 0NG
United Kingdom

External Examiner: Dr Lorne Horton
Max-Planck-Institut für Plasmaphysik
Boltzmannstraße 2
D-85748 Garching bei München
Germany

Internal Examiner: Dr Adrian Cross
Department of Physics
University of Strathclyde
Glasgow, G4 0NG
United Kingdom

Initial Submission: October 14th, 2005

Oral Examination: December 6th, 2005

Final Submission: December 17th, 2005

Abstract

The thesis examines the effectiveness of spectral emission from a neutral helium gas puff at the periphery of the tokamak plasma for diagnosis of spatially resolved electron temperature and density. The study specifically relates to the Mega Ampère Spherical Tokamak, MAST, for which extensive independent support diagnostic measurements are available, but the analysis is designed to be of general applicability to all magnetic fusion devices.

The work commences with an appraisal of the fundamental atomic data required for modelling the helium spectral line emission. It is shown that electron collision data are key to the analysis, but that the existing data required extension, and the utilisation of the data required reappraisal in light of the complexities introduced by resonance structure. These data are completely reworked and their uncertainties analysed.

A comprehensive model for the evolution of the populations of helium atoms penetrating the plasma was developed, which included full generalised collisional-radiative modelling of both ground and metastable states and their relative influence on the formation of excited populations and consequential spectral emission. It is shown how the differential character of collision cross-section data for different transitions enables a sensitivity to both electron temperature and density. The model is extended to include the spatial variation in the tokamak, the angular spread of the gas puff, and the influence of observational lines-of-sight.

A set of experiments were carried out on the MAST tokamak using the HELIOS experimental multi-chord spectroscopic setup and combined with Thomson scattering measurements of electron temperature and density at the plasma edge. A unifying model was set up, including parametric representations of temperature and density profiles at the plasma edge, and used in globally optimised fitting of the experimental data. The analysis methodologies were combined with spectroscopic measurement to deduce improved electron density/temperature radial profiles. The results substantiated the diagnostic capability of the system and the theoretical models which underlay the analysis.

Deliveries from the work include new comprehensive atomic collision data, derived coefficients for analysis, and a new general analysis methodology for predictive and deductive applications of generalised collisional-radiative (GCR) modelling.

Contents

Abstract	i
Contents	ii
List of Figures	iv
List of Tables	vi
Acknowledgements	vii
1 Introduction	1
1.1 Plasma confinement	2
1.2 Tokamak edge physics	3
1.3 Relevant atomic physics	7
1.4 HELIOS experimental diagnostic	11
1.5 Alternative diagnostic methods	14
1.5.1 Thomson scattering diagnostic	14
1.5.2 Langmuir probe diagnostic	17
1.5.3 D_α emission diagnostic	19
1.5.4 Neutral lithium diagnostic	20
1.6 Thesis outline	20
2 Fundamental data and modelling	22
2.1 R -matrix and RMPS calculations	24
2.2 Interval-averaging method	27
2.2.1 Considering distribution averaging	32
2.3 Merged data analysis	43
2.3.1 Database collision strengths	44
2.3.2 Database uncertainty estimates	46
2.3.3 Data error propagation	50
2.4 Generalised collisional-radiative modelling	51
2.5 Conclusions	58
3 Helium gas puff experiments on MAST	60
3.1 Neutral helium gas injection	61
3.2 HELIOS spectrometer & collection optics	69
3.3 Plasma configuration	76

3.4	Summary of the MAST pulses	82
3.5	Utilising resultant HeII emission	96
3.6	Conclusions	96
4	Prediction and deduction using an emission model for MAST	98
4.1	Computational overview	99
4.2	Functional fitting of non-spectroscopic N_e and T_e profile data	102
4.3	Levenberg–Marquardt algorithm	104
4.4	Calculating spatially resolved metastable populations	112
4.5	Calculating spatially resolved emissivities	116
4.6	Simulating HELIOS lines-of-sight	119
4.7	Temporal variation	125
4.8	Limits on the modelling	128
4.9	Improved deduction of N_e and T_e profiles from measured HELIOS spectra	129
4.10	Conclusions	133
5	Conclusions and future work	135
	Bibliography	I

List of Figures

1.1	Image of a MAST plasma in visible light	4
1.2	The effect of ELMS on the MAST plasma density	6
1.3	Electron-impact excitation cross-section	8
1.4	Ion-impact excitation cross-section	9
1.5	HELIOS spectra for MAST shot #12209	12
1.6	Populating excitation rate coefficients	13
1.7	Diagnostic line ratios	15
1.8	Thomson scattering resolution on MAST	17
1.9	TS edge uncertainty. MAST shot #12209	18
1.10	D_α emission defining plasma edge. MAST shot #12209	19
2.1	R -matrix calculation comparison	23
2.2	Collision strength showing resonances near threshold	26
2.3	Collision strength of He-like sulphur	28
2.4	Resolving the resonance region of neutral helium	29
2.5	Interval-averaged resonance region in neutral helium	31
2.6	Interval-averaged resonance region in neutral helium II	32
2.7	Energy scale lengths of Maxwellian distribution	35
2.8	Energy scale lengths of Maxwellian distribution II	36
2.9	Graphical overview of the interval-averaging process	37
2.10	Scale length comparison for a family of κ distributions	39
2.11	Variation of distribution scale length with κ at $T_{\text{eff}} = 50$ eV	41
2.12	Variation of distribution scale length with κ at $T_{\text{eff}} = 5$ eV	42
2.13	ADAS data set evolution	45
2.14	ADAS spreadsheet data with uncertainties	50
2.15	ADAS collisional-dielectronic ionisation rate coefficient	54
2.16	ADAS collisional-dielectronic recombination rate coefficient	55
2.17	ADAS metastable cross-coupling coefficient	56
2.18	ADAS metastable cross-coupling coefficient II	57
3.1	Throughput evolution in short gas puff	64
3.2	Throughput evolution in longer gas puff	66
3.3	Neutral helium throughput, MAST shot #12209	67
3.4	Plasma termination, MAST shot #12209	68
3.5	Control waveform	69
3.6	Valve-control waveform	70
3.7	HELIOS viewing chord schematic	72
3.8	The white-light image acquired by the CCD	75

3.9	Chord positions on the CCD	77
3.10	HELIOS spectrum taken during MAST shot #12209	78
3.11	Target shot LOS density and D_α emission, shot #12158	79
3.12	Comparison of target shot and early shot plasma radii	80
3.13	EFIT reconstruction of target shot	81
3.14	Spatial and temporal evolution of emission measured by HELIOS	83
3.15	Interaction between plasma & injection nozzle during shot #10502	84
3.16	Optimised plasma configuration during shot #10504	86
3.17	Brief H-mode during MAST shot #10504	87
3.18	First plasmas during first experimental session	88
3.19	Radial D_α profile during MAST shot #12202.	90
3.20	HELIOS spectra taken during MAST shot #12202	91
3.21	Comparison of MAST shot #12241 and #12242	92
3.22	N_e and T_e from HELIOS and TS for MAST shot #12241	95
4.1	Schematic of main body of emission model	100
4.2	Metastable population model	101
4.3	Langmuir RP signals from MAST shot #12245	103
4.4	Edge TS measurements for MAST shot #12209	107
4.5	Fitting edge TS data	107
4.6	Fitting merged TS and RP T_e data	109
4.7	Fitting merged TS and RP N_e data	110
4.8	Predictive model using merged data	111
4.9	Schematic of metastable population and uncertainty calculation	113
4.10	Results of Monte Carlo attenuation modelling	115
4.11	Spatially resolved metastable populations	116
4.12	Radial emission profiles	118
4.13	Spatial variation of the triplet-line emission	120
4.14	Predicted contributions to integrated emission	122
4.15	Effect of collimation factor on line ratios	124
4.16	Revised predicted spatial variation of triplet-line emission	126
4.17	HELIOS-based radial profiles	130
4.18	HELIOS-based radial profiles II	132

List of Tables

1.1	Important ITER parameters	3
1.2	Important MAST parameters	3
1.3	Diagnostically relevant emission lines for HELIOS	11
2.1	Spreadsheet uncertainty estimation	48
2.2	Spreadsheet uncertainty estimation II	48
2.3	Final uncertainty estimation	49
2.4	Final uncertainty estimation II	49
3.1	HeI diagnostic emission lines	61
3.2	Gas flow regimes	63
3.3	Optical values for viewing chords	71
3.4	Steering mirror orientation	73
3.5	Spectrometer bandwidth calculation data	74
4.1	Initial HELIOS-based predictive study	131
4.2	Improved HELIOS-based predictive study	133

Acknowledgements

Firstly, I gratefully acknowledge the ADAS Project for providing funding for this work. Over the last three years it has been my privilege to have worked with a number of people, and I would like to take this opportunity to thank them.

The support of my supervisor, Prof. Hugh Summers, has been a great help to me during this work. He introduced me to the European fusion program as an undergraduate and encouraged me to work in a field of physics I have found stimulating and inspiring. His guidance has been invaluable throughout, however, I particularly thank Hugh for his help and advice while finalising this thesis.

My colleagues in the Department of Physics at the University of Strathclyde have provided support and a source of encouragement throughout the course of my work there. It is with gratitude I thank Dr Allan Whiteford for his assistance and advice in all things computational, Paul Bryans for his collaboration on delivering the atomic data for non-Maxwellian applications and Martin Torney for his wealth of IDL knowledge which proved to be so useful. It is rare that one can count one's colleagues as such good friends, and I thank Allan, Paul and Martin for this and all the laughs and insightful comments over the course of this work.

I would also like to thank Dr Anthony Field for his help and advice during my time at the UKAEA Culham Laboratory. He was willing to spend time discussing the applied aspects of my work, and his knowledge of the practical plasma physics necessary for the experimental studies proved vital to someone who spent the majority of the time as a theorist. The practical side of this work would never have gotten off the ground without Anthony's time, patience and hard work and I am sincerely grateful to him.

The work on the fundamental atomic physics towards the beginning of this work was aided by Prof. Nigel Badnell and Dr Connor Ballance. Nigel continues to be generous with his time and Connor's hard work on the helium R -matrix calculation provided a firm base to pursue the helium data work. His e-mails also gave a useful perspective when it came to my own R -matrix work.

Drs Hendrik Meyer and Michael Walsh were very generous with their time during my visits to Culham and I thank them both; Hendrik's role as Session Leader during my experiments was important in making the plasma behave itself long enough to get the results I needed, and Mike's knowledge of the diagnostics was very beneficial. Prof. Patrick Carolan, as head of the plasma dynamics group, made me feel extremely welcome during my visits and was willing to spend his valuable time discussing the practical aspects of the work, and for that I am grateful. Thanks also go to Dr William Morris who, as head of the experiments division at Culham, allowed me to spend time working within his department. A large thanks is due to Prof. Nicol Peacock for the conversations over the years at Culham and his valuable insight into the early fusion program in the United Kingdom. Andy Cullen's help in the machine hall is acknowledged and greatly appreciated; the second round of experiments would not have taken place without his time and help with the equipment. Dr Glen Counsell's help gathering the reciprocating probe data is gratefully acknowledged. I thank Dr Mathias Brix for his helpful discussions regarding his work with helium on TEXTOR and his thoughts on the improved fundamental data. I am grateful to Dr Martin O'Mullane for his help

during my time in Abingdon. His patience and experience are appreciated and proved to be invaluable. I am also grateful to Kate and Ernie Bell — there aren't many people who could convince me to play cricket on a scorching August afternoon, but more than once Kate and Ernie managed to make it sound like a good idea.

I would like to thank my examiners, Dr Lorne Horton and Dr Adrian Cross. Both took time to read the thesis in detail and provided useful comments and feedback on the work. Their interest in the work discussed in the thesis resulted in a thorough oral examination that was not nearly as bad as the one played out in my over-active imagination.

Acknowledgement also goes to my family: to my parents David and Catherine for their support and provision of cheap accommodation, and to my sister Lynsey for not forcing me out of the house.

A special thanks goes to my fiancée Cynthia Nam for her support and encouragement while writing this thesis. She was always there as a sounding board and I would have been lost without her. I hope I can repay the compliment when it comes time for Cynth to finalise her thesis; although, lying low for a couple of months sounds like a far less stressful option!

— Iain Paton
October 2005.

Chapter 1

Introduction

The spatial and temporal properties and behaviour of the magnetic confinement fusion plasma are fundamental in developing nuclear fusion as a viable energy source. In particular, the temperature and density of the plasma play a key role in the behaviour and stability of the system. Since the early days of experimental plasma fusion physics, a great deal of effort has been committed to developing diagnostic systems to measure these parameters. Modern operating scenarios, including the high confinement mode, or H-mode[1], and Internal Transport Barriers, ITBs[2], have focused this attention on the spatial profiles of the temperature and density at the edge of the plasma and their effect on the confined plasma.

This work pertains to the modelling and measurement of neutral helium emission in the edge plasma. The helium spectral line emission is reactive to electron temperature and density, and so has potential as a diagnostic for the edge — a region in which alternative diagnostic methods have relatively high uncertainties. The thesis provides an in-depth assessment of the application of helium as an edge plasma diagnostic. This chapter introduces background physics relevant to the current study. Section 1.1 details the characteristics of the fusion devices relevant to the work, especially MAST and ITER. The physical regimes used in the experimental studies, and some of the special phenomena modifying the plasma behaviour are discussed in section 1.2. Section 1.3 deals with fundamental atomic processes. Section 1.4 describes the HELIOS experimental diagnostic system on the MAST experiment, which is the basis of the experimental studies of the thesis, and whose effective exploitation as a diagnostic was a main purpose of the thesis. Alternative diagnostic systems used comparatively in the thesis are summarised in section 1.5. Section 1.6 gives more detail of the content of the remainder of the thesis.

1.1 Plasma confinement

A significant step forward in plasma confinement came with the development of the Soviet tokamak in 1968[3, 4, 5]. Contemporary large-scale experiments use devices of the tokamak or stellarator[6] designs, with the tokamak being divided into “conventional” and “spherical” categories, CT and ST. These two classes of tokamak refer to the aspect ratio of the individual devices, defined as the ratio of the major to minor radii. The Mega Ampère Spherical Tokamak, MAST¹, has an aspect ratio of ~ 1.4 compared to the more conventional, ITER-like, aspect ratio of $\sim 3^2$. The spherical tokamak is arguably a plasma confinement configuration with the potential to compete with the performance of the conventional design without the need for large magnetic fields[7].

The theoretical predictions of the spherical tokamak’s advantages led to the development of a number of devices on which these predictions were tested and verified. Earlier machines included: CDX-U³, HIT⁴, MEDUSA⁵, TS-3⁶, and START¹; which were followed by a set of medium-sized devices: ETE⁷, GLOBUS-M⁸, and TST-2⁶; and two larger machines: NSTX³ and MAST. The combination of plasma stability and confinement exhibited by the spherical tokamak allows access to high β operating regimes. Coupled with large current carrying capability due to the natural elongation of the plasma, this allows high performance operation for a relatively low toroidal magnetic field. These performance features have justified extended experimental study and diagnostic analysis of the spherical tokamak. Tables 1.1 and 1.2 give important parameters of ITER and MAST respectively[8, 9].

Figure 1.1 shows an example of a MAST plasma observed in visible light. One can see that the shape of the plasma and its proximity to the central column is very different from that of a conventional tokamak. It is worth noting that extensive work has been carried out at MAST on the merging/compression method, which was developed originally on START[10]. This allows an initial plasma of over 400 kA with no flux from the central solenoid — an important start-up feature for a future power station based on the spherical tokamak design[11]. The bright spot to the left of the central column in figure 1.1 is the mid-plane deuterium injector used to refuel the device. The divertor

¹Culham Science Centre, Oxfordshire, UK

²ITER, the International Thermonuclear Experimental Reactor, is the next generation fusion device to be built at CEA Cadarache in France.

³Princeton Plasma Physics Laboratory, New Jersey, USA.

⁴Helicity Injected Torus, University of Washington, Washington, USA.

⁵University of Wisconsin, Wisconsin, USA.

⁶University of Tokyo, Japan.

⁷National Space Research Institute, Brazil.

⁸Ioffe Institute, St Petersburg, Russia.

Parameter	Value
Plasma minor radius, a	2.0 m
Plasma major radius, R_0	6.2 m
Aspect ratio, R_0/a	3.1
Toroidal magnetic field (core)	5.3 T
Plasma current	15 MA
Aux. heating power	40 MW

Table 1.1: A breakdown of the expected values of important parameters of ITER.

Parameter	Value
Plasma minor radius, a	0.65 m
Plasma major radius, R_0	0.85 m
Aspect ratio, R_0/a	≥ 1.3
Toroidal magnetic field	≤ 0.63 T
Plasma current	≤ 2 MA
Aux. heating power	~ 6.5 MW

Table 1.2: A breakdown of the important parameters of MAST.

strike points are also clearly visible at the top and bottom of the plasma. The edge plasma, the target of the present studies, is evident on both the outboard and inboard side.

Another difference between MAST and conventional devices such as JET⁹ and ASDEX-U¹⁰ is the relatively large vacuum vessel. The distance from the plasma's outer edge to the wall is ~ 50 cm on MAST, compared to ~ 5 – 10 cm on ASDEX-U, giving good diagnostic access to the outboard plasma. This contrasts with the lack of access to the inboard side due to the central column.

1.2 Tokamak edge physics

The experimental studies conducted for this work used thermal injection of helium into the MAST edge plasma from the low-field, outboard side. The edge plasma, as referred to here, is the region between the hot core plasma and the material walls; that is outwards from a few centimetres inside the last closed flux surface on MAST. Some issues regarding the edge plasma are:

- the open magnetic field line region outside of the separatrix is the scrape-off

⁹Joint European Torus, Culham Science Centre, Oxfordshire, UK

¹⁰Axially Symmetric Divertor EXperiment-Upgrade, Max-Planck-Institut für Plasmaphysik, Garching, Germany.

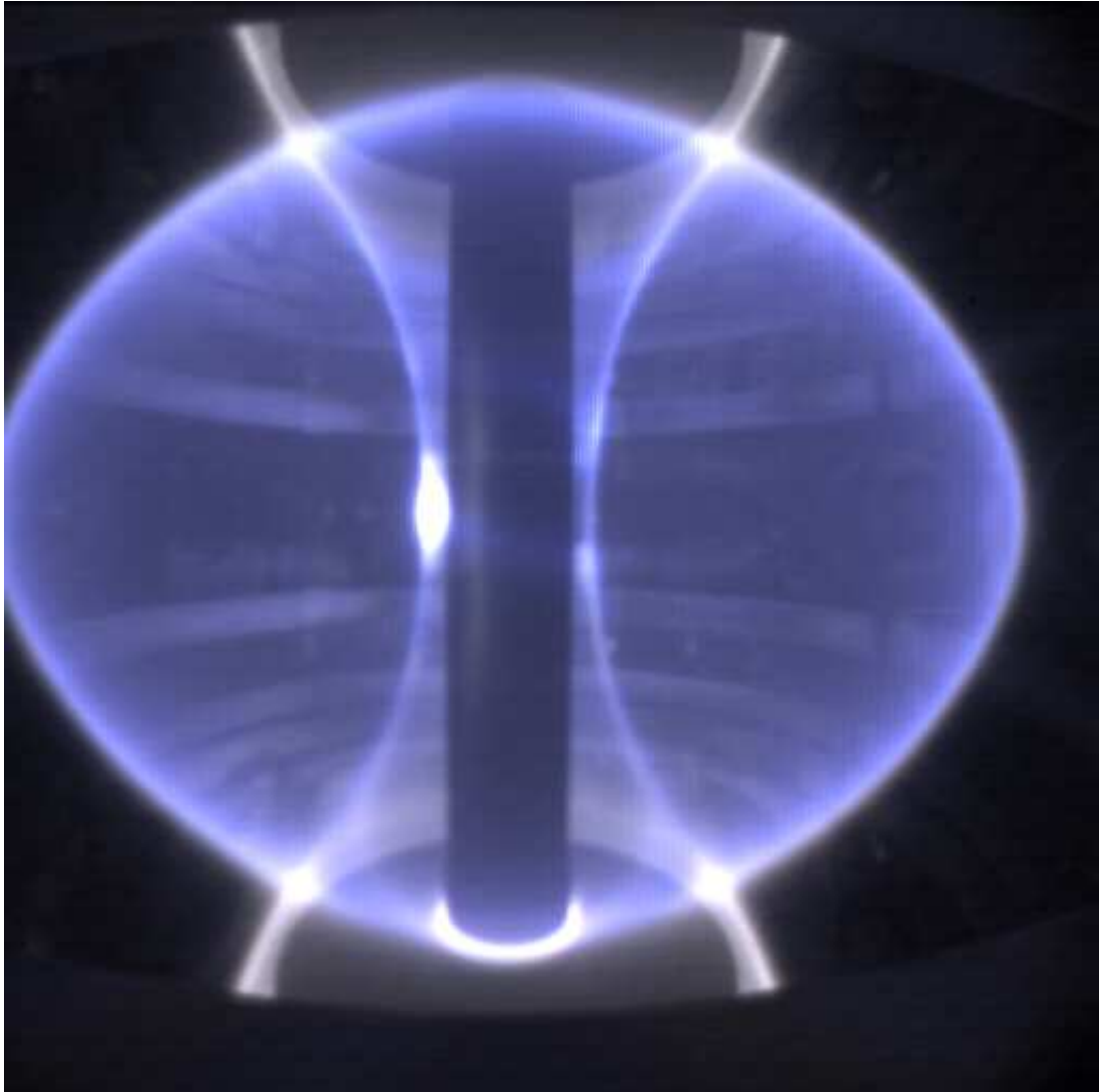


Figure 1.1: The MAST plasma from shot #4211. It can be seen that the small aspect ratio makes the plasma appear spherical rather than the toroidal shape of a conventional tokamak.

layer, or SOL;

- an efflux of particles from the confined plasma propagate along the field lines in the SOL to the divertor target zone;
- flux at the edge determines the balance of impurity species in the confined plasma[12, 13];
- the low density combined with adverse viewing geometry can lead to poor Thomson scattering resolution at the edge[14]. This will be discussed in detail in section 1.5.1;
- the position of the last closed flux surface, or separatrix, can oscillate during ELMy H-mode[15, 16, 17, 18], so it is important in confinement studies;
- since the plasma interacts with the first wall, the SOL is generally turbulent with large variations in the electron temperature and density[19];
- the edge plasma will mediate the removal of helium ash and the recovery of tritium in a working fusion reactor[20, 21].

H-mode is a regime of high confinement that can occur in tokamaks[1, 22] and is routinely accessed by the MAST device[23]. The edge temperature and density gradients in H-mode are steeper than those associated with L-mode, and the differences between these two confinement regimes modifies the behaviour of the confined plasma. The large H-mode edge gradients lead to the onset of a specific magnetic hydrodynamic instability — the Edge Localised Modes, or ELMS — which expel energy and particles from the confined plasma[24]. This adds to the power load on the plasma facing components from the line emission and bremsstrahlung.

Figure 1.2 shows ELM behaviour as observed in the MAST device. The upper plot shows the D_α emission measured as a function of time. When the D_α signal is low there is reduced transport from the core confined plasma to the scrape-off layer and there are peaks in the D_α signal when energy and particles are expelled from the plasma. A comparison of the upper and lower plots in figure 1.2 shows that there is a correlation between the peaks in the D_α signal and dips in the line integrated density, as one would expect if the ELMS acted to remove material and energy from the plasma.

The electron density and temperature of the edge plasma can be modified considerably by the propagation of an ELM. The alteration of the edge parameters during an ELM crash and the effect on helium emission is simulated and discussed in chapter 4.

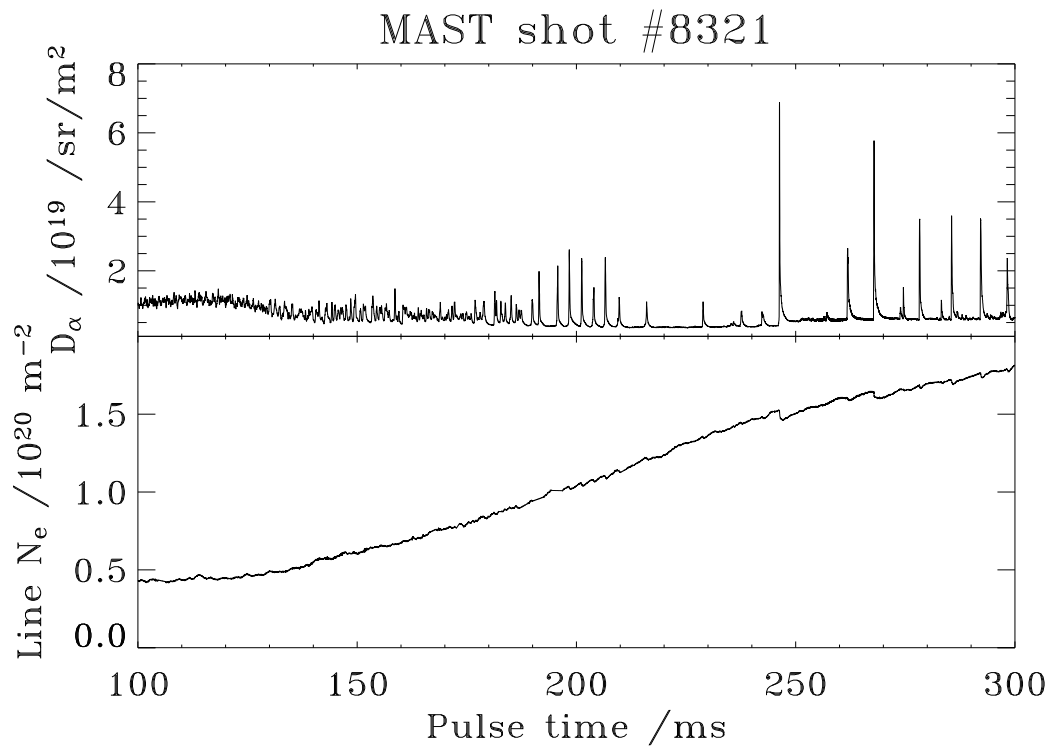


Figure 1.2: The upper plot shows D_α emission during MAST shot #8321 indicating the presence of ELMS. The lower plot shows the corresponding variation of the plasma density characterised by sharp decreases correlated with peaks in the D_α signal.

1.3 Relevant atomic physics

One of the main aims of the work is to determine the viability of using neutral helium emission to deduce local radial electron temperature and density at the outboard edge of the MAST plasma. Consider a helium atom advancing in to the tokamak; atomic processes compete to alter the energy and ionisation state of the particle. The particle will encounter and interact with electrons and ions[25, 26]. The relatively low energy of the helium suggests the most efficient redistribution process will be that driven by the electrons — electron-impact excitation and de-excitation will play a key role, as indicated in figures 1.3 and 1.4[27, 28]. The cross-section for ion-impact excitation is evidently orders of magnitude less than that of electron-impact in the low-energy regime. As the helium moves through the edge plasma it is in a region of increasing electron temperature and density, the electron-driven ionisation will therefore be important in determining the radial attenuation of the neutrals. Recombination of the He^+ to re-form the neutral helium is a lesser effect due to the high temperature.

In the zero density approximation, when an atom or ion is excited, the state will decay radiatively to a lower energy in a period of time independent of the plasma conditions; however, the edge plasma of the tokamak has finite density, sufficiently high to interrupt collisionally the radiating excited states. Thus the population evolution of the system is more complex. Collisional-radiative (CR) theory is the appropriate method to determine such population structure[29].

To obtain the population structure of an atom or ion in the CR regime, it is necessary only to calculate the time dependence of the long-lived, dominant populations. For helium these are the ground and metastable states. The relaxation time for the ordinary (non-metastable) states means they are in instantaneous equilibrium with the metastables. That is:

$$\tau_g \sim \tau_m \gg \tau_o \quad (1.1)$$

where τ_g is the collisional-radiative lifetime of the ground state, τ_m is the lifetime of the metastable states and τ_o is the lifetime of the ordinary excited states.

In principle, helium has a ground state and two excited metastables¹¹: $1s^2\ ^1S$, $1s2s\ ^1S$ and $1s2s\ ^3S$. Two of these states evidently have long lifetimes: $1s^2\ ^1S$ being the ground state and $1s2s\ ^3S$ a state which decays to ground by a very weak spin-change transition[31]. The cross-section for a spin-change transition is relatively small. The different transition types will be discussed in section 2.2.1. In practice, the relaxation

¹¹Throughout the thesis ‘metastable’ will be used for states with a lifetime longer than the ‘ordinary’ states. Therefore the term ‘metastable’ will be used to describe both the ground state and excited metastables.

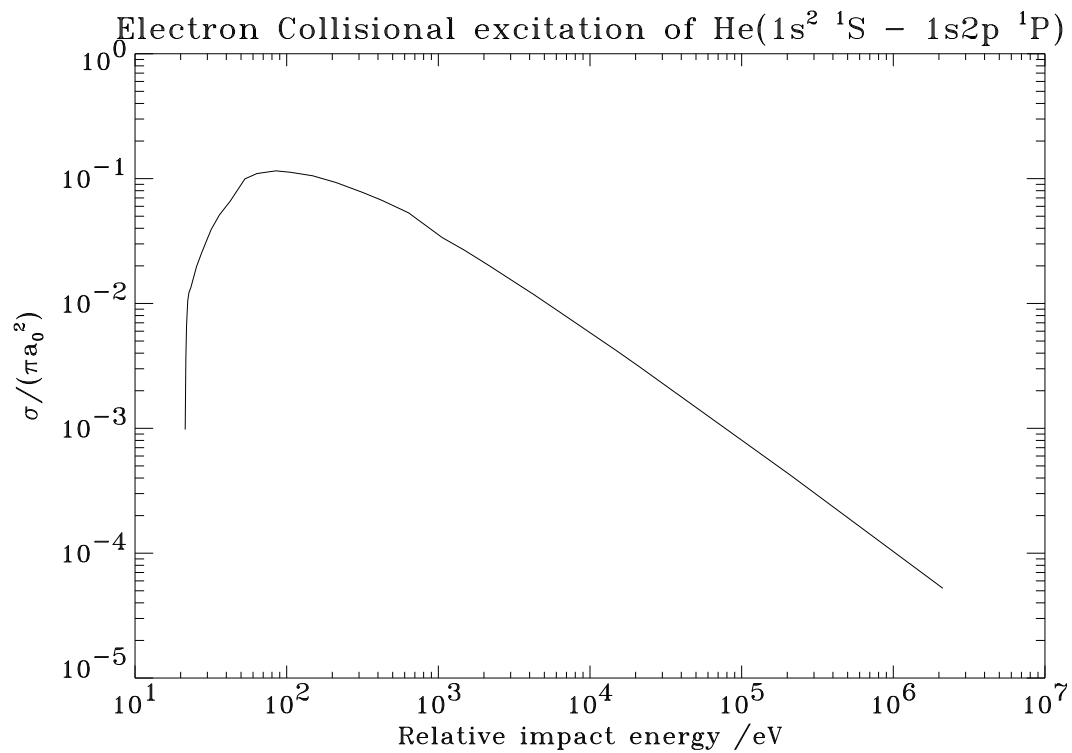


Figure 1.3: The variation of the electron-impact excitation cross-section as a function of relative energy for the He($1s^2\ ^1S - 1s2p\ ^1P$) excitation[27].

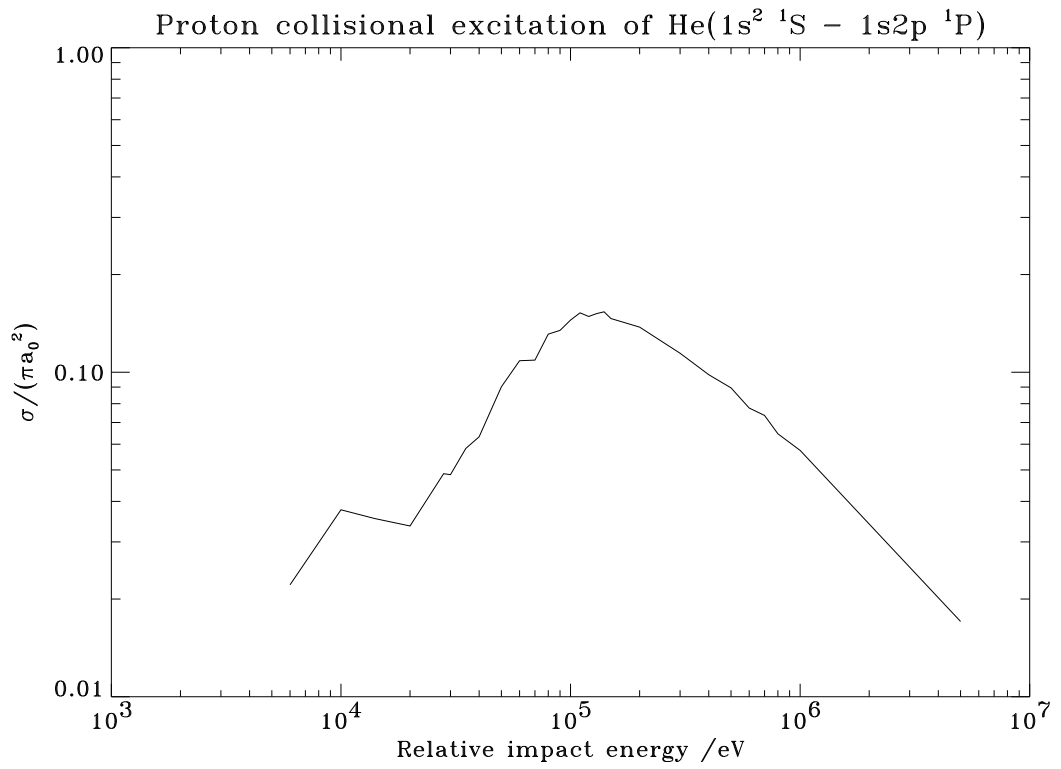


Figure 1.4: The variation of the ion-impact excitation cross-section as a function of relative energy for the He($1s^2\ ^1S - 1s2p\ ^1P$) excitation[30].

time of $1s2s^1S$ at tokamak densities means it does not have to be treated as a metastable. This is because the plasma is of sufficient density such that there is a relatively large collisional coupling between the $1s2s^1S$ and $1s2p^1P$ states. Thus the $1s2s^1S$ drains via the $1s2p^1P$ state, for which there is a large spontaneous decay rate to ground. Therefore this work will only treat the $1s^2^1S$ and $1s2s^3S$ states as metastable and the system of equations describing their population evolution is given by:

$$\frac{dN_\rho}{dr} = -\frac{N_e}{v_{\text{puff}}} [N_\rho S_{\rho \rightarrow +} + N_\rho q_{\rho \rightarrow \rho'} - N_{\rho'} q_{\rho' \rightarrow \rho}]; \quad \rho, \rho' = 1, 2; \rho \neq \rho' \quad (1.2)$$

where ρ, ρ' indicate the metastable or ground and v_{puff} is the effective speed of the helium advancing into the plasma. $S_{\rho \rightarrow +}$ and $q_{\rho \rightarrow \rho'}$ represent the ionisation rate coefficient and metastable cross coupling coefficient between metastable ρ and ρ' respectively.

Generalised Collisional Radiative (GCR) theory[32] deals with modelling the excited populations of ions and the ionisation and recombination to adjacent stages in the presence of long-lived, dynamically evolving metastables. The GCR modelling carried out as part of this work is detailed in chapter 4.

The key issue is to compare the lifetimes given in equation 1.1 to the timescales associated with gross changes in plasma conditions. The scale lengths, λ , for electron temperature and electron density variation in a plasma are given by:

$$\lambda_{T_e}^{-1}(\mathbf{r}) = \frac{1}{T_e(\mathbf{r})} |\nabla T_e(\mathbf{r})| \quad (1.3)$$

$$\lambda_{N_e}^{-1}(\mathbf{r}) = \frac{1}{N_e(\mathbf{r})} |\nabla N_e(\mathbf{r})|$$

where \mathbf{r} is a position within the plasma.

If the speed of an atom or ion across a region described by these scale lengths is v , then:

$$\tau_{T_e} \simeq \frac{\lambda_{T_e}}{v} \quad (1.4)$$

$$\tau_{N_e} \simeq \frac{\lambda_{N_e}}{v}$$

and it is often found that $\tau_g \sim \tau_m \simeq \tau_{T_e} \sim \tau_{N_e} \gg \tau_o$. This is the situation for the helium gas puff. A quantitative discussion of lifetimes and generalised collisional-radiative modelling, including the basis for including and excluding specific processes from the helium modelling, is given in section 2.4.

Line	Wavelength / Å	Transition	Approx. Rel. Int.
—	6560	D ($n = 3 \rightarrow 2$)	~ 10.0
1	6678	He ($1s2p\ ^1P - 1s3d\ ^1D$)	1.0
2	7067	He ($1s2p\ ^3P - 1s3s\ ^3S$)	$\sim 0.3-0.5$
3	7283	He ($1s2p\ ^1P - 1s3s\ ^1S$)	~ 0.1

Table 1.3: Table of diagnostically relevant emission lines in the HELIOS observable spectral region.

1.4 HELIOS experimental diagnostic

As previously stated, one of the main aims of this thesis is to determine whether the helium line emission, which is reactive to electron temperature and density, can form an effective diagnostic for these plasma parameters at the outboard plasma edge. This section will outline the different components of the HELIOS system and the method of deducing diagnostic deliverables.

The HELIOS spectrometer[33] has a bandwidth of $\sim 1100\text{Å}$, see section 3.2, and in normal operation observes a visible spectral region of $\sim (7000 \pm 500)\text{Å}$. This allows the spectrometer to observe three diagnostically useful HeI lines, as well as the D_α line, if required. These transitions are shown in table 1.3.

It is convenient to use the short-hand notation when referring to states of neutral helium. The notation $n\ ^mL$ denotes that there is an implicit $1s$ electron; n is the principal quantum number of the second electron; m is the multiplicity of the system; and L is the total orbital angular momentum[34]. For example, $3\ ^1P$ refers to He($1s3p\ ^1P$).

The diagnostic potential of HELIOS is gained from the variation of spectral line ratios of the different transitions shown in table 1.3; a singlet-to-singlet ratio, lines 1:3, and a singlet-to-triplet ratio, lines 3:2. The approximate relative line intensities given in table 1.3 are taken from a spectrum of MAST shot #12209, shown in figure 1.5.

Differential variation of the 6678Å and 7067Å lines on the different viewing chords, which correspond to different radial positions within the plasma, is evident from figure 1.5. This differential variation can be used to make diagnostic deductions of plasma parameters.

Figure 1.6 shows the excitation rate coefficients from the ground state for the three upper states given in table 1.3. One can see, from a relatively low temperature comparable to that of the SOL, the spin-change excitation diverges from the other two curves. The differential variation with T_e results in temperature sensitivity. It is also evident from figure 1.6 that the excitations to the singlet states behave similarly with temperature. Thus their line ratio is predominantly a function of electron density.

The confrontation of such measured spectroscopic data with the calculated den-

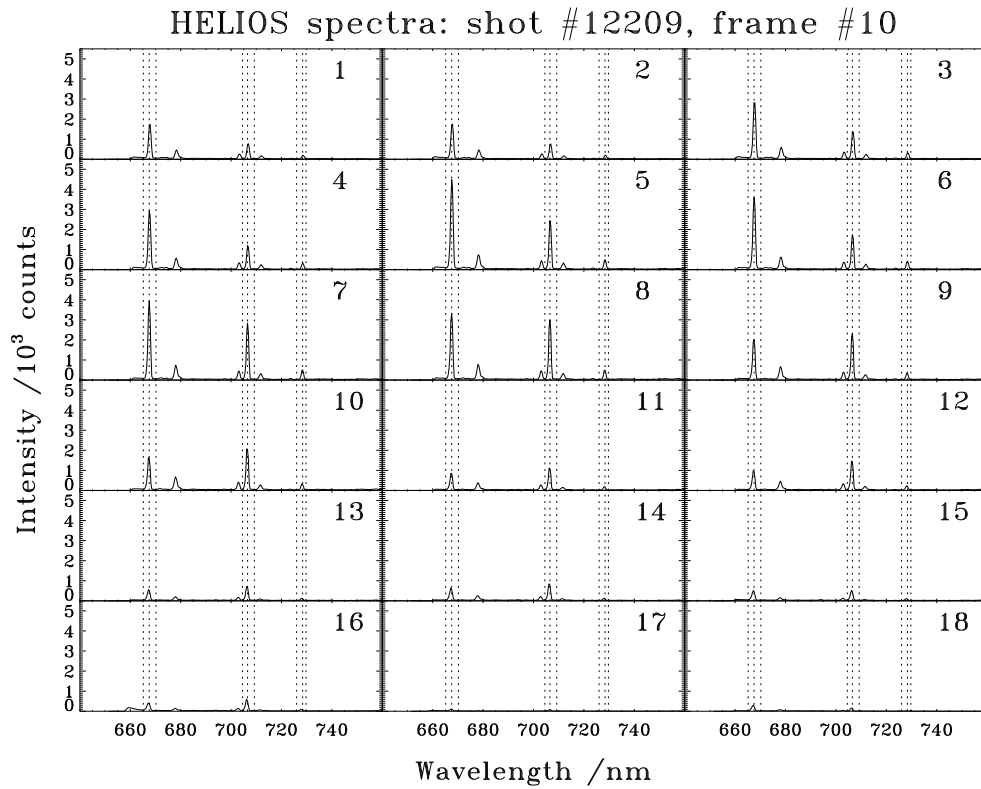


Figure 1.5: The HELIOS spectra from MAST shot #12209, taken on 24th February 2005 during the second experimental period. The approximate relative line intensities can be seen for the 18 viewing chords.

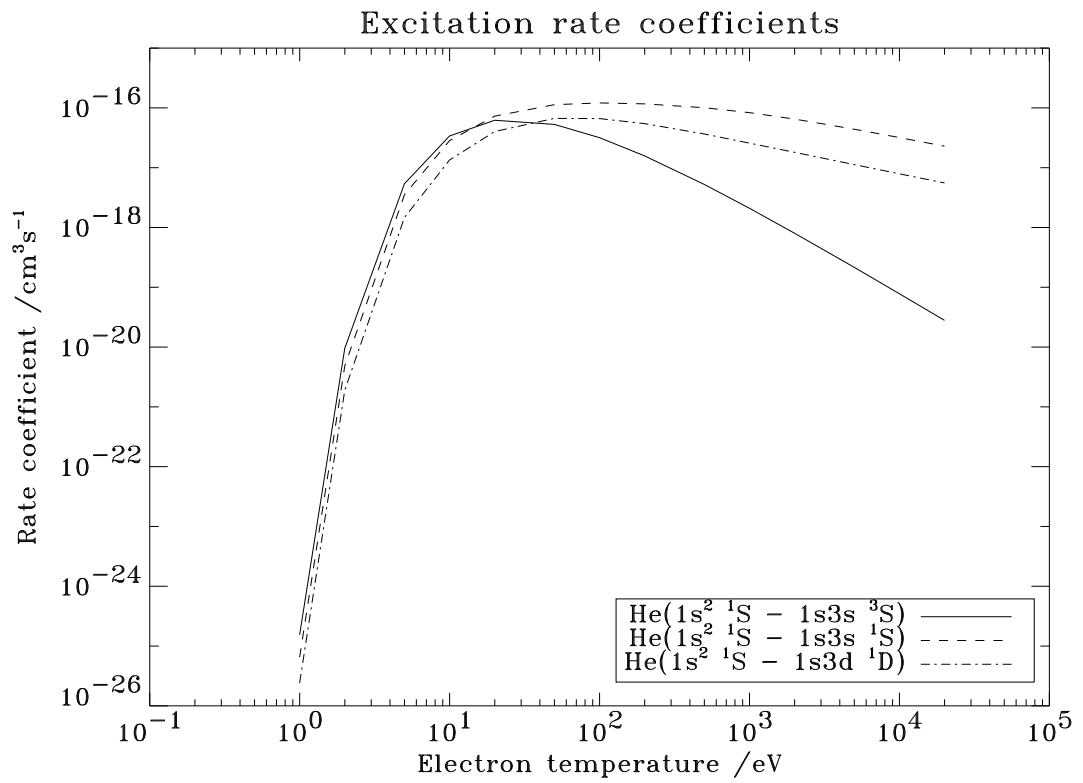


Figure 1.6: The electron-impact excitation rate coefficients populating the upper states in table 1.3.

sity and temperature sensitive emission ratios allows determination of a point in temperature–density space. Figure 1.7 shows contours of the diagnostic line ratios as a function of N_e and T_e and demonstrates their inherent diagnostic sensitivity.

The lines described above have been used previously with some success to study the JET divertor[35, 36, 37, 38] and the plasma edge of the COMPASS-D¹[39, 40, 41] and TEXTOR¹²[26] tokamaks. This work seeks to combine detailed fundamental data with dedicated spectroscopic measurements of HeI emission in a well-diagnosed magnetically confined fusion plasma. A comprehensive theoretical and computational framework to describe and investigate the spatial and temporal variation of the emission is outlined. This investigation includes the role of the 2^3S metastable in the emission process and an attempt to deduce the collimation of the gas injection nozzle, which has proven difficult to measure accurately. Amalgamating spectral emission measurements with the complete theoretical emission model allows the deduction of local electron density and temperature local radial profiles. These issues will be discussed in chapter 4.

Section 1.5.1 highlights the Thomson scattering diagnostic’s lack of spatial resolution and large measurement uncertainties at the low-field edge of MAST. One of the main objectives of this work is to determine if the HELIOS diagnostic can be used as an alternative to Thomson scattering at the edge of MAST, and if so, over what spatial region it is applicable.

1.5 Alternative diagnostic methods

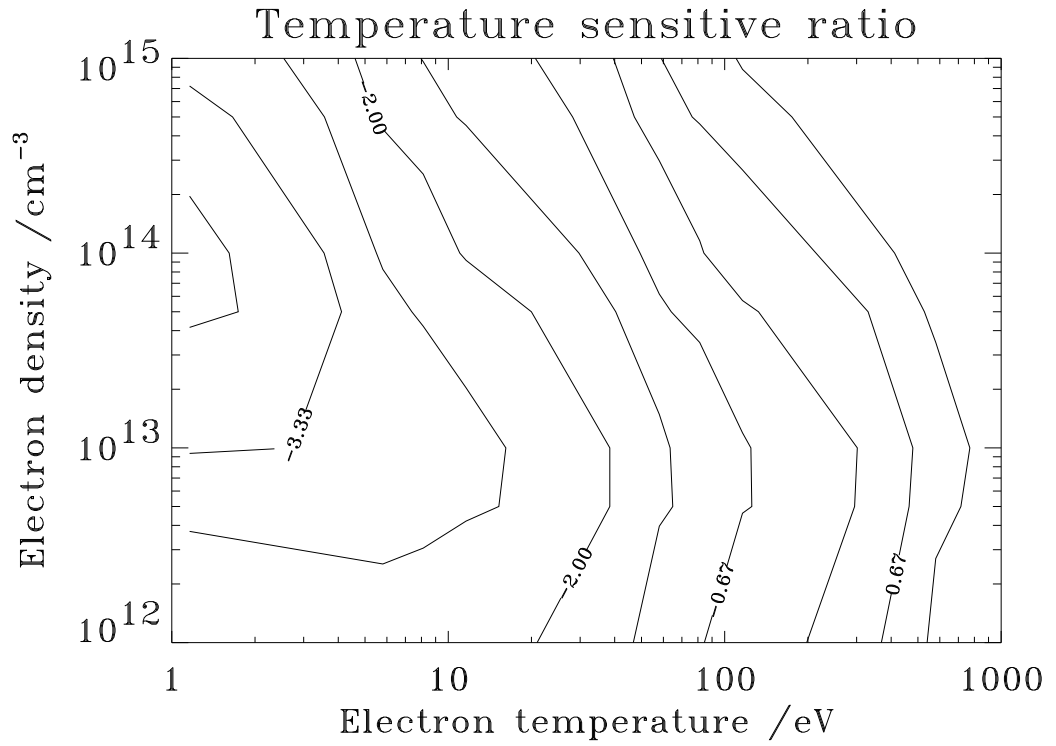
This work required HeI emission to be measured in a well-diagnosed plasma, and this section details alternative diagnostic methods used[42]. Problems with the diagnostic sensitivity of the methods are highlighted, with details of the optimal merging of diagnostic techniques discussed in chapter 4.

1.5.1 Thomson scattering diagnostic

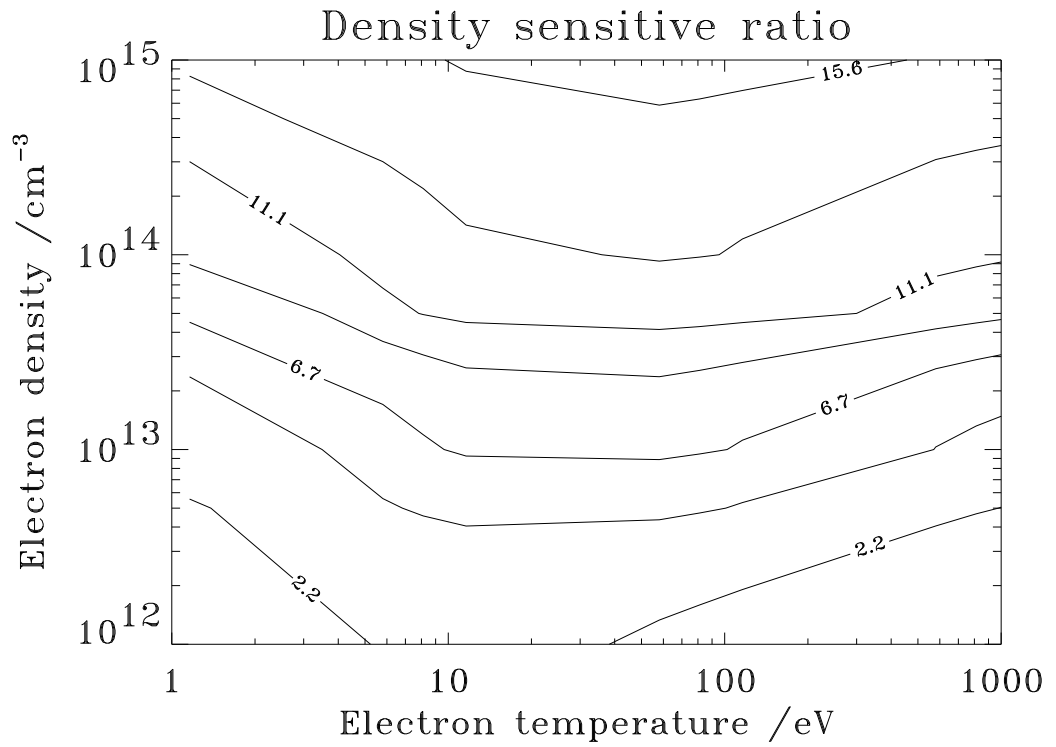
Thomson scattering (TS) is one of the most widely used diagnostic methods for measuring electron temperature, T_e , and density, N_e , in hot plasmas. The method works by measuring the spectrum of photons scattered by the free electrons in the plasma.

There are currently two TS systems operating on MAST[14]. Both systems measure the full plasma diameter at the mid-plane of the vessel. One of the systems captures high spatial resolution measurements at one time-point in the pulse using a 10 J ruby

¹²Tokamak EXperiment for Technology Orientated Research, Forschungszentrum Jülich, Germany.



(a) Temperature sensitive line ratio, 1:3



(b) Density sensitive line ratio, 3:2

Figure 1.7: Contours showing the diagnostic sensitivity of the line ratios 1:3 and 3:2, as given in table 1.3.

laser. This system provides electron temperature and density profiles at ~ 300 spatial positions in the plasma. The second system uses four Nd:YAG lasers pulsed at 50 Hz to provide profiles of 19 spatial positions at 200 Hz. The Debye length of a MAST plasma is $\sim 30 \mu\text{m}$ and the wavelength of the Thomson scattering source on MAST is $\sim 7000 \text{ \AA}$. Incoherent scattering takes place because the Debye length is much greater than the source wavelength[43].

A main experimental aim of this work was to determine whether the HELIOS diagnostic could be used to determine N_e and T_e at the low-field plasma edge. The TS diagnostic ability is poor in this region of the plasma for two reasons: firstly, the spatial resolution of the diagnostic is limited due to the flux resolution at the outboard edge; secondly, the low electron density at the edge leads to large uncertainties in the fitting carried out on the TS spectrum. Figure 1.8 shows the normalised flux, ψ_N , of a typical plasma and the normalised flux resolution, $\Delta\psi_N$, of the ruby TS system varying with major radius. These quantities are defined as:

$$\psi_N = \frac{\psi_0 - \psi}{\psi_0 - \psi_{\text{edge}}} \quad (1.5)$$

and

$$\Delta\psi_N = \Delta R \left| \frac{\partial\psi_N}{\partial R} \right| \quad (1.6)$$

where ψ_0 is the flux on the magnetic axis and ψ_{edge} is the flux at the edge of the plasma, defined as the last closed flux surface (LCFS).

One can see that the relatively large value of $\Delta\psi_N$ at the outboard edge leads to poor spatial resolution. This is because a larger change in flux is associated with a change in radial position on the high field side than with the same change of radial position on the low-field side giving better radial resolution on the high field side. Furthermore, the beam path is parallel to the flux surfaces on the inboard side which allows for more efficient diagnosis of the plasma conditions. The asymmetry of the normalised flux in figure 1.8 is due to the large Shafranov shift that is characteristic of spherical tokamaks[44]. The Shafranov shift means the flux surfaces on the high field side are much closer together in real space than they are on the low-field side.

Figure 1.9 shows TS spectra obtained from the MAST plasma. A clear spectrum is visible for a radial position of $R=1.39 \text{ m}$, but a poor signal is detected at $R=1.49 \text{ m}$. This means the functional fit to the TS spectrum which determines N_e and T_e is better at $R=1.39 \text{ m}$. It is evident from the radial temperature profile that TS does not deliver reasonable diagnostic output at the edge. The experimental studies in the thesis were mainly concerned with the large uncertainties in the diagnostic data due to poor

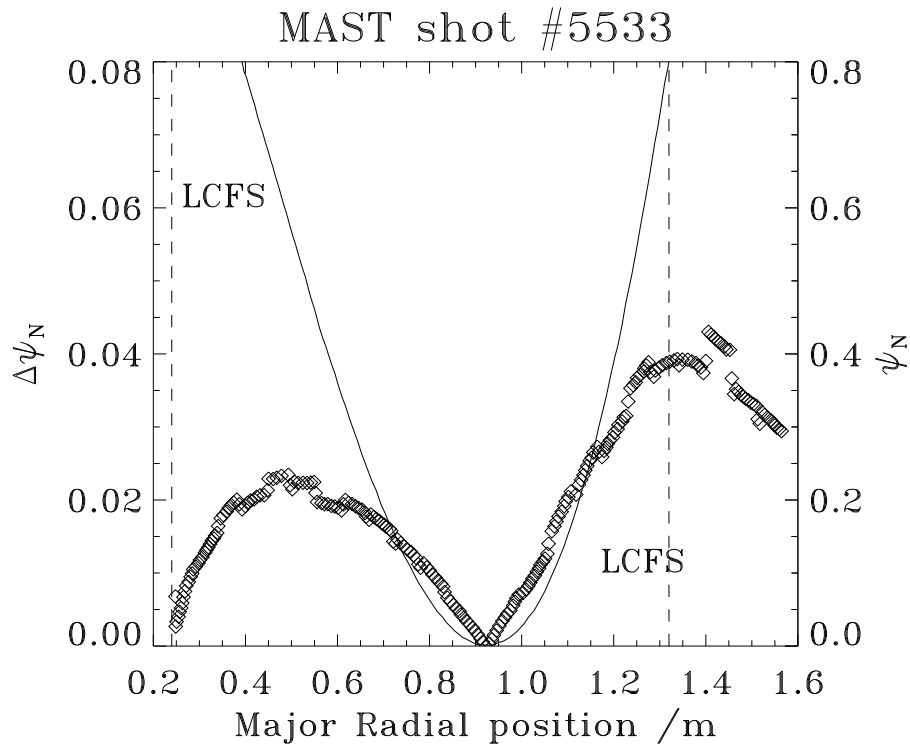


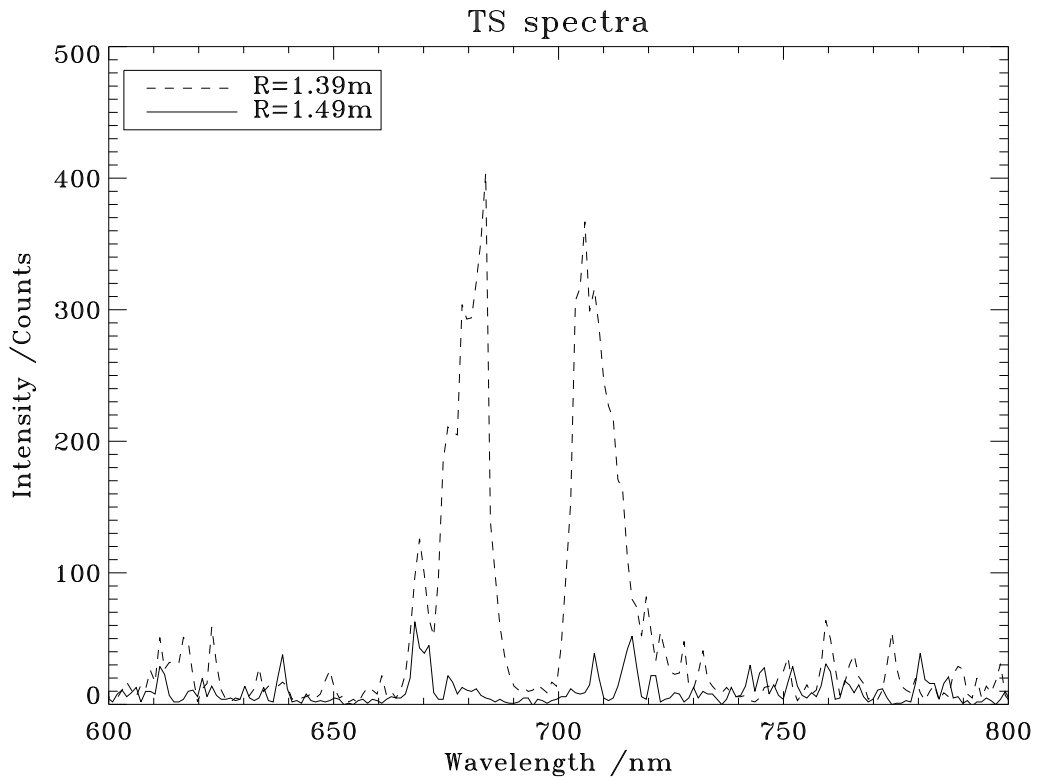
Figure 1.8: Normalised flux resolution of the ruby TS system on MAST. The solid line denotes the normalised flux, ψ_N , and the data points denote the normalised flux resolution, $\Delta\psi_N$. One can see that the normalised flux resolution is poor on the low-field side of the device, which is of interest in this work[14].

TS signal, how this could be overcome, and what role, if any, HELIOS could play in diagnosing the edge.

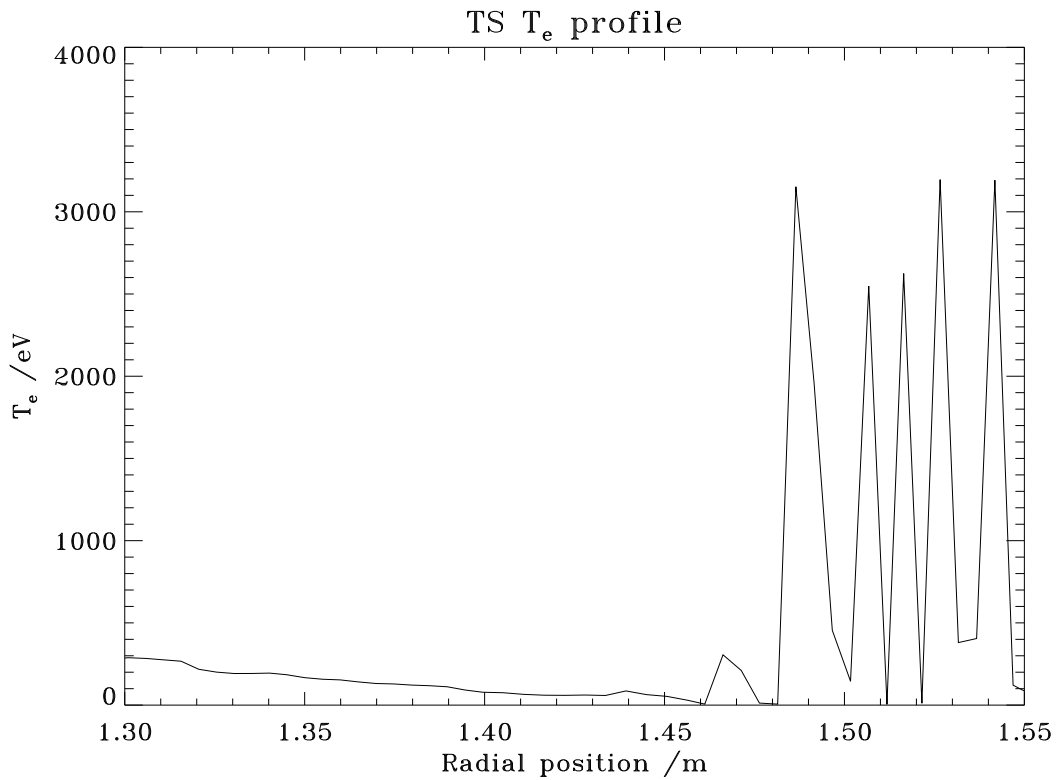
1.5.2 Langmuir probe diagnostic

An electric probe, often called a Langmuir probe, can be inserted into the plasma to determine electron temperature and density. The probe is biased with a potential difference, causing a current to flow when inserted into the plasma. The I-V characteristic can then be used to measure N_e and T_e in the SOL.

The temperature and density data extracted from the probe measurements are generally accompanied by a lot of high frequency noise. This leads to uncertainty in the measurements, but less than that associated with TS measurements at the plasma edge. Probe data can be used to supplement the radial profiles determined by TS, optimising the data over a radial range from inside the core plasma through the SOL. The use of probe measurements and the technique used to extract N_e and T_e data from the



(a) TS spectra



(b) TS radial T_e profile

Figure 1.9: The spectrum used to deduce N_e and T_e by TS and the resultant radial temperature profile for MAST shot #12209. The spectrum at $R=1.49$ m has no discernible lines from which to deduce the plasma parameters compared with the same measurement at $R=1.39$ m. This results in large uncertainties at the edge. This can be seen from the poor radial profile at the plasma edge.

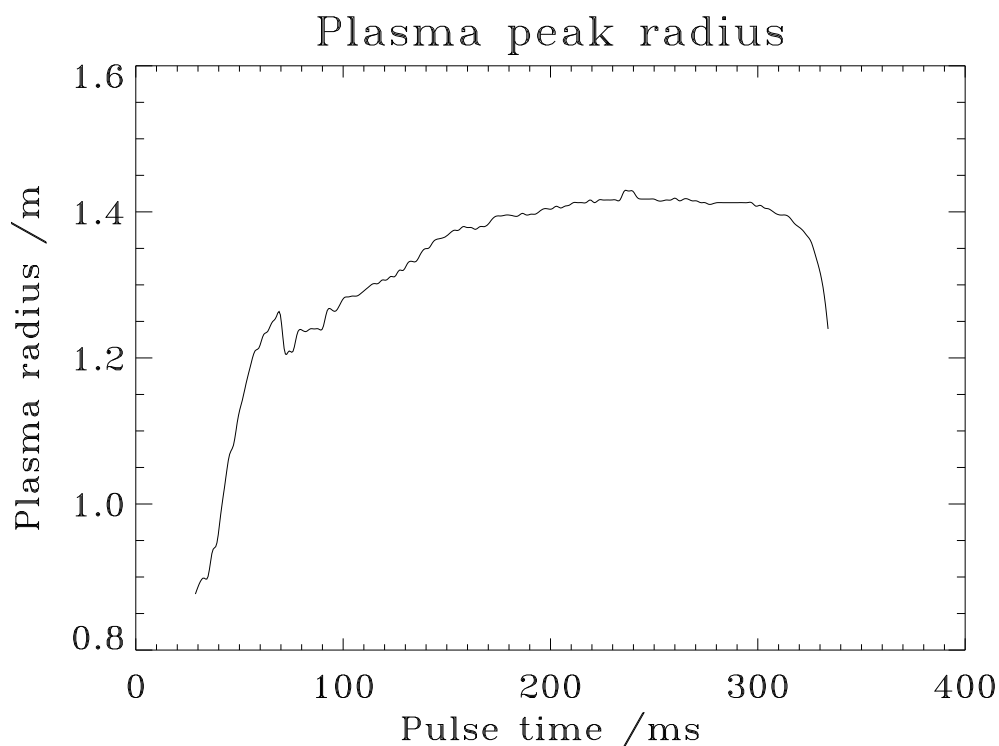


Figure 1.10: Variation of the plasma edge with time within MAST shot #12209, one of the shots discussed in detail in chapter 4. One can see the plasma growing after formation and settling to a peak radius of ~ 1.4 m.

background noise is discussed in chapter 3.

1.5.3 D_α emission diagnostic

The position of the separatrix is important since it defines the boundary between the confined plasma and the SOL. The D_α emission diagnostic can be used to trace the edge of the plasma during a pulse. Figure 1.10 shows the variation of the separatrix with time for MAST shot #12209, one of the shots that will be discussed in more detail in chapter 3.

From a simple consideration of the physics involved it is logical that the emission will be in the vicinity of the separatrix, where N_e and T_e increase from their relatively low values in the SOL to those characteristic of the core plasma. It is therefore necessary to measure accurately the position of the separatrix, and the D_α emission diagnostic provides a convenient monitor.

1.5.4 Neutral lithium diagnostic

Measurements with a thermal lithium beam have allowed density perturbations in the SOL to be studied on TEXTOR[45]. A detailed study using a pair of thermal beams has measured radial and poloidal fluctuations in the SOL density[46]. On ASDEX-U, lithium has been used to measure electron densities[47, 48, 49] based on the detection of the Li(2s – 2p) resonance line at 6708Å[50]. These, and other, lithium studies have contributed a great deal to the diagnosis of the SOL, and has subsequent implications for the application of a thermal helium beam. The development of an edge spectral diagnostic is of limited interest if there exists a similar, proven method of obtaining the same deliverables. An alternate approach to spectral diagnosis must have definite advantages before the study and development can be justified. A major advantage of using helium rather than lithium is its large ionisation potential, ~ 24.6 eV, compared to lithium’s ionisation potential of ~ 5.4 eV[51]. Since the edge plasma of interest comprises a region several centimetres on either side of the separatrix, lithium’s relatively low ionisation potential would mean the spatial extent of a spectroscopic N_e and T_e diagnostic based on lithium would be less than one based on helium. The penetration can be improved by increasing the beam energy, although this is generally at the expense of spatial resolution. Due to the large N_e and T_e gradients and magnitudes in H-mode plasmas, the region of applicability of any spectroscopic diagnostic will be small compared with the minor radius. Therefore, choosing an emission source with a relatively large ionisation potential is crucial to diagnostic application given the small injection energy. MAST is not equipped with a lithium beam, therefore a direct comparison of the diagnostic effectiveness of the two beam species is not possible. However, the significant body of research carried out with lithium beams over a large range of energies should be noted[52, 45, 53, 54, 55]. There is also the financial advantage of a diagnostic based on HeI emission being considerably cheaper than a LiI system.

1.6 Thesis outline

The thesis describes the development of a predictive model for the HeI emission from the low-field edge of the Mega Ampère Spherical Tokamak and the experimental work undertaken to confront the model. The complete spatial and temporal model can then be used with measured spectral emission data to deduce local N_e and T_e radial profiles. Chapter 2 discusses the calculation of the fundamental atomic data required for the predictive modelling. It includes details of the *R*-matrix method used to calculate the excitation collision strengths and the numerical methods developed to reduce the large quantity of data produced by an *R*-matrix calculation to a manageable amount that

can be used in the database framework of the Atomic Data and Analysis Structure, ADAS[56]. Chapter 2 also discusses the work undertaken to provide a new data class within ADAS: the uncertainty associated with the ADF04 specific ion data. Generalised collisional-radiative modelling is also discussed in chapter 2.

Chapter 3 gives details of all aspects of the experimental work carried out on HELIOS validation during the experimental campaigns M4 and M5. This chapter discusses in depth the issues that arose during the campaigns and the work that had to be carried out to commission, calibrate and utilise the HELIOS spectrometer.

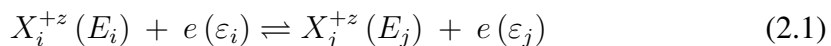
Chapter 4 discusses the work undertaken to develop a complete spatial and temporal model of the HeI emission at the low-field edge of MAST. The different stages of numerical simulation and development will be discussed. Computational outcomes will also be discussed, such as the determination of the collimation of the neutral helium injection nozzle, which proved to be problematic to measure directly. The improved deduction of local N_e and T_e radial profiles supported by the superior electron-impact excitation data, discussed in chapter 2, and a complete GCR treatment of the metastable populations within a theoretical spatial and temporal emission model, will be outlined.

The conclusions drawn from this work and recommendations for future work are presented and discussed in chapter 5.

Chapter 2

Fundamental data and modelling

The electron-impact excitation/de-excitation reaction is of the form



where $E_i < E_j$. The left-to-right process denotes an excitation, right-to-left denotes de-excitation. $\varepsilon_i + E_i = \varepsilon_j + E_j$; $E_{i,j}$ is the energy of the ion $X_{i,j}^{+z}$ relative to its ground state; ε_i is the energy of the incident electron; and ε_j is the energy of the scattered electron. This reaction can be described by the collision strength[57, 58, 59], Ω_{ij} , defined as:

$$\Omega_{ij}(\varepsilon) = \omega_i \left(\frac{\varepsilon_i}{I_H} \right) \frac{\sigma_{i \rightarrow j}(\varepsilon_i)}{\pi a_0^2} = \omega_j \left(\frac{\varepsilon_j}{I_H} \right) \frac{\sigma_{j \rightarrow i}(\varepsilon_j)}{\pi a_0^2} \quad (2.2)$$

with the property that it is symmetrical between initial and final states due to micro-reversibility. ω_i is the statistical weight of the state i ; ε_i/I_H is the relative impact energy; $\sigma_{i \rightarrow j}$ is the cross-section for the transition from state i to j ; and a_0 and I_H represent the Bohr radius and Rydberg energy respectively.

Fundamental helium–electron impact studies have been carried out over the last sixty years[60, 61] with new, more detailed, work building on the foundation of the previous calculations. The calculation of fundamental excitation data over the last thirty years has been aided by the use of the R -matrix method[62]. The R -matrix studies have gained precision over time as computational resources and techniques have improved[63, 64, 65]. These improvements have resulted in variations in the data sets due to different levels of approximation. The failure of theory to converge with experiment above the ionisation threshold in earlier studies is noted. This was resolved by including “pseudostates” to span the continuum; this will be returned to in the next section. As computing resources have increased, more detailed approximations have been made and these have been shown by experiment to converge on experimen-

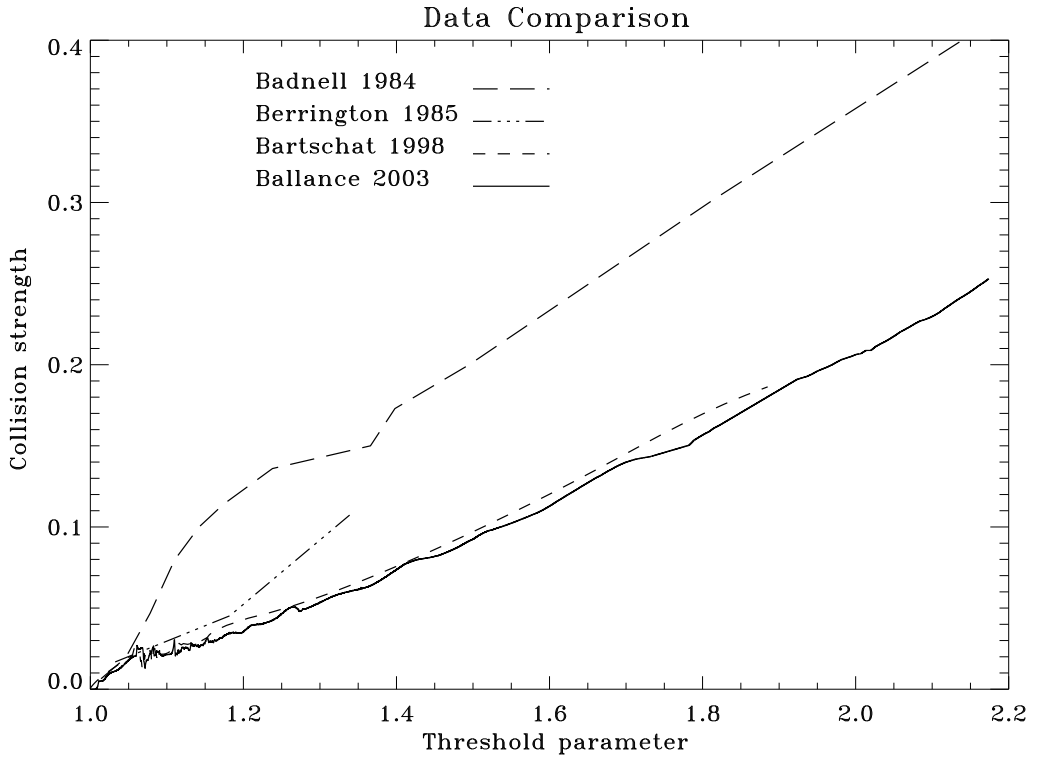


Figure 2.1: A comparison of the calculation of the excitation collision strength for $\text{He}(1\ ^1\text{S} - 2\ ^1\text{P})$ as a function of energy in terms of the threshold parameter. It can be seen that there are quite large differences from earlier to later calculations, and the latest work carried out in support of this study resolves resonances near threshold[69]. See text for more details.

tally acceptable values[66, 67, 68, 69] — verified by confrontation with sophisticated experiments[70, 71]. Figure 2.1 exemplifies the evolution of collision strength data derived from R -matrix calculations. The threshold parameter used in figure 2.1 is defined in terms of the projectile energy, ε_i , and the transition energy, ΔE_{ij} , as:

$$X = \frac{\varepsilon_i}{\Delta E_{ij}} \quad (2.3)$$

The calculation of Badnell (1984) contains no coupling to the higher bound states nor to the continuum. Berrington (1985) couples to the $n = 3$ bound states, but not to the continuum. One can see that the over-estimation of the collision strength near the excitation threshold has been mostly resolved by the inclusion of the higher states in the model. The calculation of Bartschat (1998) couples to the bound states up to $n = 4$, and also to the continuum. One can see that the deviation in the vicinity of the ionisation threshold, $X \simeq 1.2$ has been resolved in this calculation. The work of

Ballance (2003) builds on this base to produce resonance-resolved collision strengths from a more physically accurate collision model.

2.1 *R*-matrix and RMPS calculations

The close-coupling method[72], as developed for continuum Hartree–Fock solutions[58], has proven to be a practical means of studying electron–ion collision phenomena since the individual behaviours of both the colliding and ionic electrons are revealed. In its most general form, the close-coupling wavefunction for a quasi two–electron system can be expanded as the sum of product wavefunctions assuming angular coupling and antisymmetrisation[73]:

$$\Psi(\vec{r}_1, \vec{r}_2) = \sum_i \Phi_i(\vec{r}_1) f_i(\vec{r}_2) + \int d\vec{k} \Phi_{\vec{k}}(\vec{r}_1) f_{\vec{k}}(\vec{r}_2) \quad (2.4)$$

In this complete expansion, Φ_i and $\Phi_{\vec{k}}$ are the bound and continuum wavefunctions of the one-electron ion. f_i and $f_{\vec{k}}$ are the wavefunctions for the scattering electron, which are determined by solving the close-coupling equations which result from truncating and/or approximating equation 2.4. The *R*-matrix method is widely used for this purpose.

Only a finite close-coupling expansion can be used in a numerical treatment and the choice of which terms to retain defines the art of performing electron–ion collision calculations within basis expansion methods. The earliest close-coupling calculations for electron–hydrogen collisions could only include the lowest six states due to the computational power available at the time: 1s, 2s, 2p, 3s, 3p, 3d. It was realised that the atomic polarisability, which is given by:

$$\alpha = \sum_{\ell, n > 1} \frac{\langle \Phi_{1s} | \vec{r} | \Phi_{n\ell} \rangle \langle \Phi_{n\ell} | \vec{r} | \Phi_{1s} \rangle}{E_{n\ell} - E_{1s}} + \sum_{\ell} \int d\vec{k} \frac{\langle \Phi_{1s} | \vec{r} | \Phi_{\vec{k}\ell} \rangle \langle \Phi_{\vec{k}\ell} | \vec{r} | \Phi_{1s} \rangle}{E_{\vec{k}\ell} - E_{1s}} \quad (2.5)$$

received an 18.4% contribution from the second term in equation 2.5[74]. This indicates that the two-electron continuum must be included to describe accurately the polarisation of the hydrogen atom by an incoming electron: an important realisation in the development of the collision model.

Studies following the Sturmian basis set ideas[75, 76] introduced the so-called “pseudostates” into the close-coupling expansion. These are unphysical orbitals which, in general, overlap the bound and continuum hydrogenic orbitals $\Phi_{n\ell}$ and $\Phi_{\vec{k}\ell}$. A distinctly improved convergence over earlier results was obtained but non-trivial dis-

crepancies with experiment remained. Despite advances in computational power over the subsequent two decades, and the development of more sophisticated pseudostate methods[77], the disagreement between theory and experiment for electron–hydrogen collisions remained unresolved.

The development of “Converged Close-Coupling” (CCC)[78] resolved this discrepancy. The solution of the Lippman–Schwinger (momentum–space) equations with a large expansion of Laguerre pseudo-orbitals obtained excitation cross-sections that were in good agreement with experiment. This was a significant result since it indicated that the two-electron continuum expansion in equation 2.4 could be adequately represented by a finite pseudostate expansion. Furthermore, it was found that the electron-impact ionisation cross-sections could be extracted by analysing the excitation to the pseudostates[79].

The Belfast (Wigner–Eisenbud) R -matrix codes[62, 80] are relatively robust in that they can be used to study electron–ion systems of arbitrary complexity. “ R -matrix with Pseudostates” (RMPS) has been successfully used to treat two–electron processes in the photoionisation and electron-impact excitation and ionisation of numerous atomic systems[65, 81, 82]. Figure 2.2 gives an example of the collision strengths calculated using the R -matrix method for neutral helium excitation.

The energy grid on which the R -matrix calculation is carried out is extremely fine, and chosen to resolve fully the resonance structure. Section 2.2 explores how this large density of data points may be reduced safely for different applications of the data, and how the data can be included within a database structure such as the one that forms part of ADAS.

The R -matrix method takes into account numerous physical effects that contribute to cross-sections, and is applicable to all kinds of ions, from neutral to highly ionised species. Because of this, and in more complex species, the R -matrix method can be very computationally intensive[83].

The R -matrix theory starts by dividing the configuration space using a sphere of radius a centred on the target nucleus. In the inner region, $r < a$, where r is the relative coordinate of the free electron, electron exchange and correlation between the scattered electron and the target are important. Thus a close-coupling expansion like that in equation 2.6 is adopted for the system[84, 85]. In the outer region, $r > a$, electron exchange between the free electron and the target can be neglected if a is large enough to contain the charge distribution of the target and the scattered electron moves in the long-range asymptotic multipole potentials of the target ion. The inner and outer regions are linked by the R -matrix on the boundary, $r = a$. The total wavefunction Ψ in the inner region for any energy E can be written in terms of the energy independent

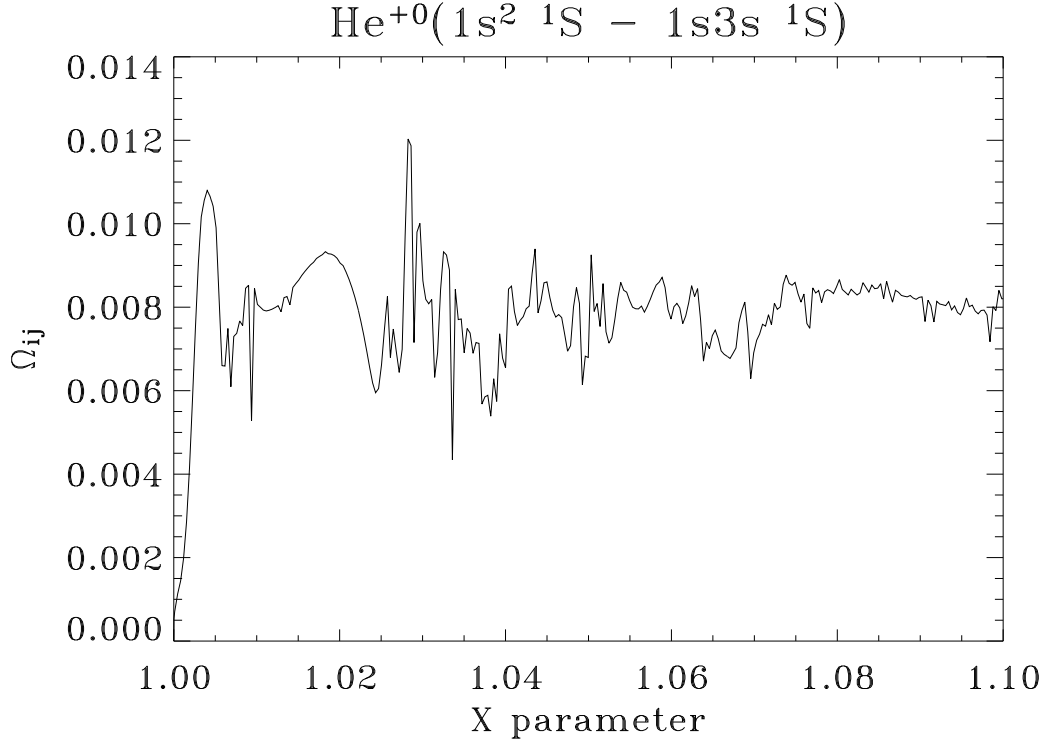


Figure 2.2: The resonance structure resolved using the R -matrix with pseudostates method[69]. These resonances can influence non-Maxwellian distributions[27] and low-temperature systems.

basis set $\{\psi_k\}$ as[86, 87]:

$$\Psi = \sum_k A_{Ek} \psi_k \quad (2.6)$$

which satisfies the time-independent Schrödinger equation

$$\hat{H}_{N+1} \Psi_i = E \Psi_i \quad (2.7)$$

where E is the total energy and the Hamiltonian is defined by

$$\hat{H}_{N+1} = \sum_{i>j} \frac{1}{r_{ij}} - \sum_i \left(\frac{1}{2} \nabla_i^2 + \frac{Z}{r_i} \right) \quad (2.8)$$

The energy dependence is carried by the A_{Ek} coefficients. The surface amplitudes, w_{ij} , are obtained by diagonalising the Hamiltonian. This leads to the definition of the R -matrix as:

$$R_{ij}(E) = \frac{1}{2a} \sum_k \frac{w_{ik}(a) w_{jk}(a)}{E_k - E} \quad (2.9)$$

The diagonalisation of the total Hamiltonian need only be carried out once, yet enables the R -matrix to be determined at all energies. This is the reason for the considerable computational efficiency of the R -matrix method.

The scattering matrix, and thus the cross-section for a transition, can then be calculated by solving the scattering problem in the outer region subject to the boundary condition imposed by the R -matrix.

In the exemplary collision strength given in figure 2.2, resonance structure is evident near threshold. Physically, resonances occur when the energy of the incoming electron is close to that required to get trapped into an autoionising state of the $N + 1$ electron system by redistributing energy with the N electron system. Since the electron remains trapped for a time before autoionisation takes place, a phase shift occurs in the scattered wavefunction that manifests itself as sharp peaks or troughs in the cross-section. These resonances appear as Rydberg series converging onto the various excitation thresholds of the target, as shown in figure 2.3 [88].

In complex ions with many levels close in energy, the series of resonances often overlap and interference effects occur between the bound and scattering wavefunctions. Therefore, the fine detail of these resonances cannot be reproduced by superimposing an isolated resonance feature on a background cross-section[89]. This interference in the resonance structure on the background cross-section is one of the main subtleties handled by the R -matrix method.

The effective contribution to the cross-section due to resonance structure is a further matter of note. It has been found, for example, that the $1s^2 1S_0 - 1s2s^3S_1$ transition in He-like Fe shows a factor of two difference in the collision strength when one includes resonance detail compared to a calculation in which it is neglected[90, 91]. The treatment of resonances at this modern level of sophistication is therefore of importance across the range of species from the helium focused on in this work, through to the heavy species of particular interest due to their proposed use as plasma facing components on ITER[92, 93, 94], their applications in discharge lithography[95] and their existence in solar plasmas[96].

2.2 Interval-averaging method

The most sophisticated calculation of neutral helium collision strengths executed to date, was carried out to support the studies of this thesis by Ballance (2003). This

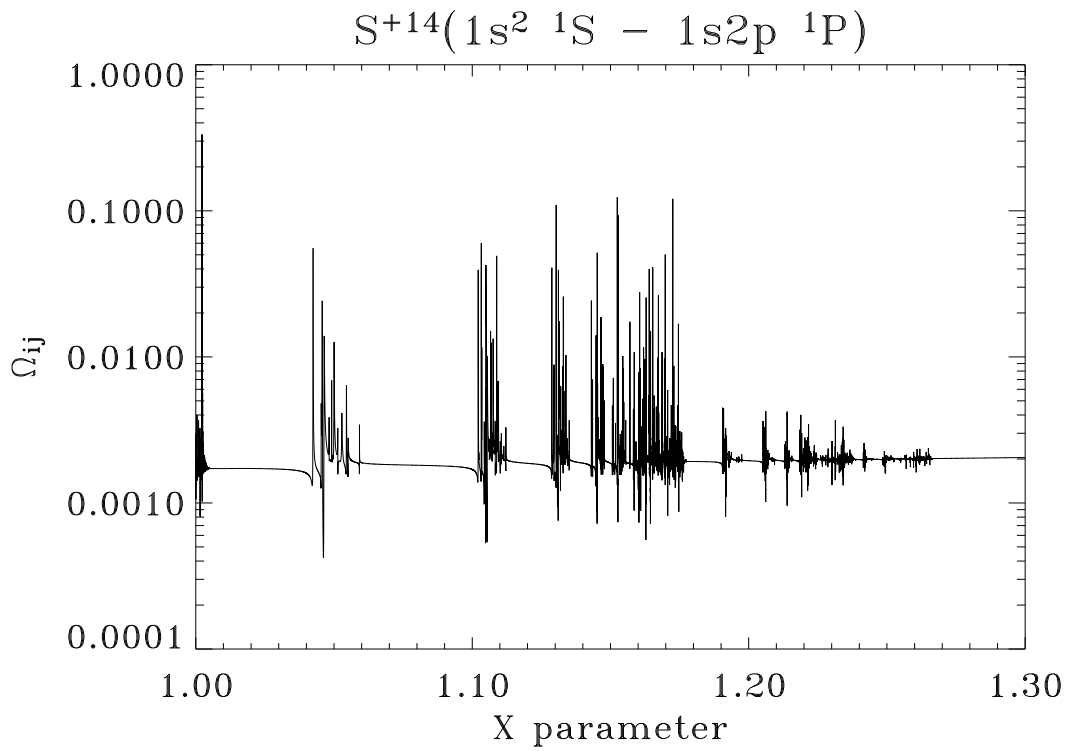


Figure 2.3: The collision strength of $S^{+14}(1s^2 \ ^1S - 1s2p \ ^1P)$. One can see the resonances bunched in a Rydberg series converging on the various excitation thresholds of the target He-like sulphur ion.

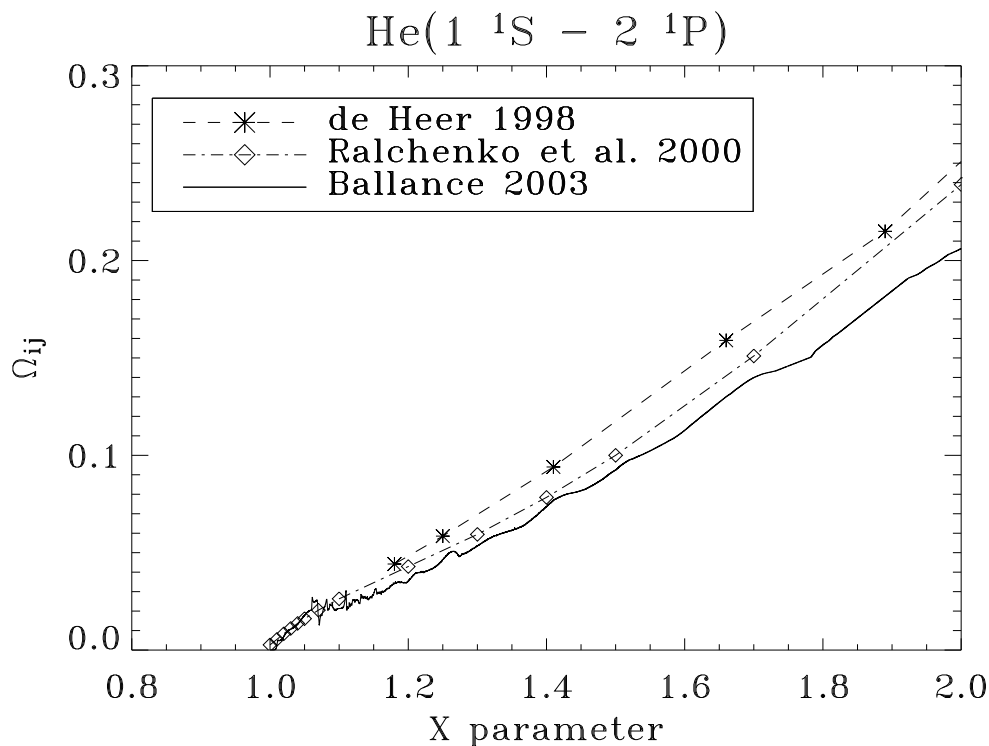


Figure 2.4: The energy resolution of the most recent R -matrix calculation for neutral helium compared to that of previous data sets. The dipole excitation $\text{He}(1^1\text{S} - 2^1\text{P})$ is used in this illustration.

involved detailed pseudostate expansions to span the continuum while minimising the influence on physical deliverables[69]. This calculation utilised a fine energy mesh at low projectile energies, chosen to resolve the resonance structure in the collision strengths. Figure 2.4 shows different calculations for the excitation $\text{He}(1^1\text{S} - 2^1\text{P})$. One can see from figure 2.4 that the calculation of Ballance (2003) pays great attention to the resonance region, which influences distribution averages used to describe low-temperature plasmas.

The large quantity of data produced using the R -matrix method is necessary to resolve resonance structure as shown in figure 2.4 — where ~ 9000 data points were included — and more obviously, figure 2.3 — with $\sim 30,000$ data points. This quantity of data is unsuitable for storage within a compact database structure for application such as ADAS, which must include very many reactions. Therefore, a process which reduces the total number of data points necessary to define a collision strength accurately for application is required[97]. The method of “interval-averaging” allows a large R -matrix data set to be reduced onto an energy grid of approximately 40 – 50

points, similar to the ADAS standard energy grid.

In order to reduce the large number of points to a workable level, a preferred grid was decided on, which would form a base for the processed data set. Between two points on the preferred grid, X_k and X_{k+1} , the average collision strength in the interval is given by:

$$\langle \Omega \rangle_{X_k, X_{k+1}} = \frac{1}{X_{k+1} - X_k} \int_{X_k}^{X_{k+1}} \Omega_{ij}(X) dX \quad (2.10)$$

where the quantities X_k refer to threshold parameters defined in equation 2.3.

One must now consider the abscissae of the interval-averaged data calculated in the manner above. It is important that the grid on which the data is output is weighted towards the peaks in the collision strength. If this is not taken into account, the procedure will displace the resonance features. In order to calculate the Ω -weighted energy, the first moment of the collision strength, μ , is calculated for all the intervals in the preferred grid.

$$\mu_{X_k, X_{k+1}} = \int_{X_k}^{X_{k+1}} X \Omega_{ij}(X) dX \quad (2.11)$$

Using μ , the Ω -weighted value of the energy associated with an interval can be calculated.

$$\langle X \rangle_{X_k, X_{k+1}} = \mu_{X_k, X_{k+1}} \left(\int_{X_k}^{X_{k+1}} \Omega_{ij}(X) dX \right)^{-1} \quad (2.12)$$

The interval-averaging process can be used to take the high-resolution R -matrix collision strength data and reduce it to a more manageable quantity. Figure 2.5 shows the resonance region $X \in [1, 1.2]$ for He($1^1S - 2^3S$) on a relatively sparse preferred grid.

One can see from figure 2.5 that the interval-averaged data set follows the main characteristics of the much larger R -matrix data without resolving all of the resonance detail. Figure 2.6 shows the same resonance region of the same transition but with a larger number of points in the preferred energy grid. One can see that the larger interval-averaged data set follows more of the resonance detail of the R -matrix data, as one would expect. However, this raises the question of objectivity in the interval-averaged data set. What is the number, and density, of points required to follow the resonance detail adequately, without tabulating, and ultimately archiving, a vast quan-

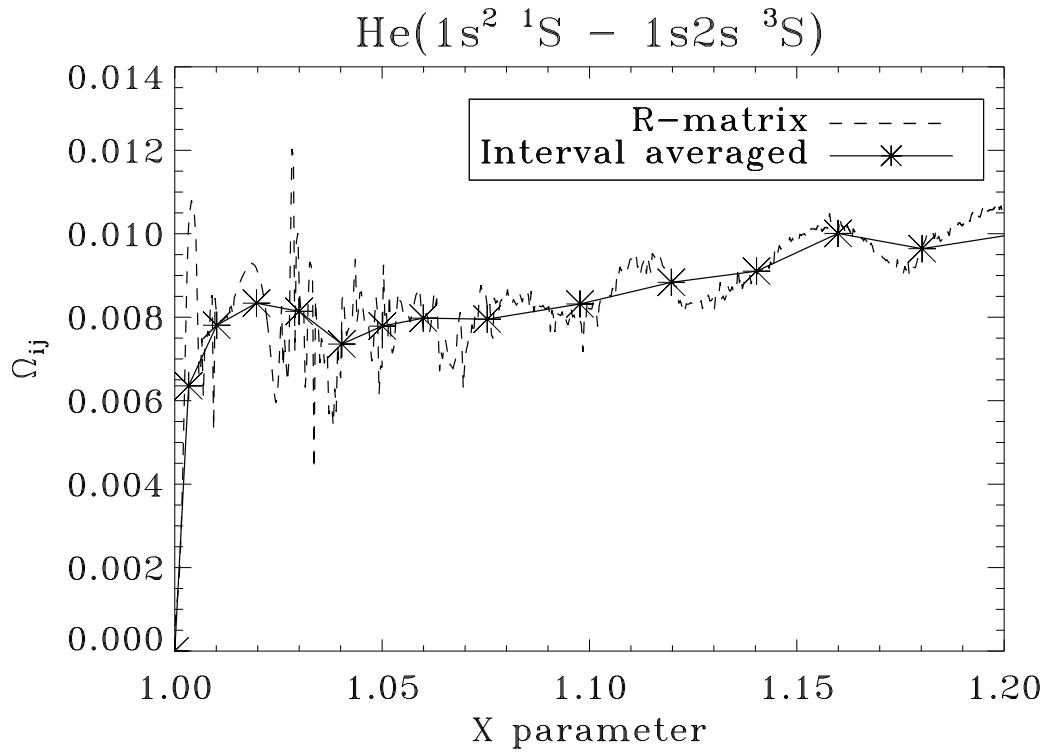


Figure 2.5: The collision strength for the transition He($1\ ^1S - 2\ ^3S$) showing how the interval-averaging technique follows the main characteristics of the resonance structure below threshold without the need for a large R -matrix data set. In this region $X \in [1, 1.2]$ the R -matrix data set has ~ 7000 data points and the interval-averaged data set has 14. It should be noted that oscillations at $X > 1.1$ are unphysical features caused by the pseudostates.

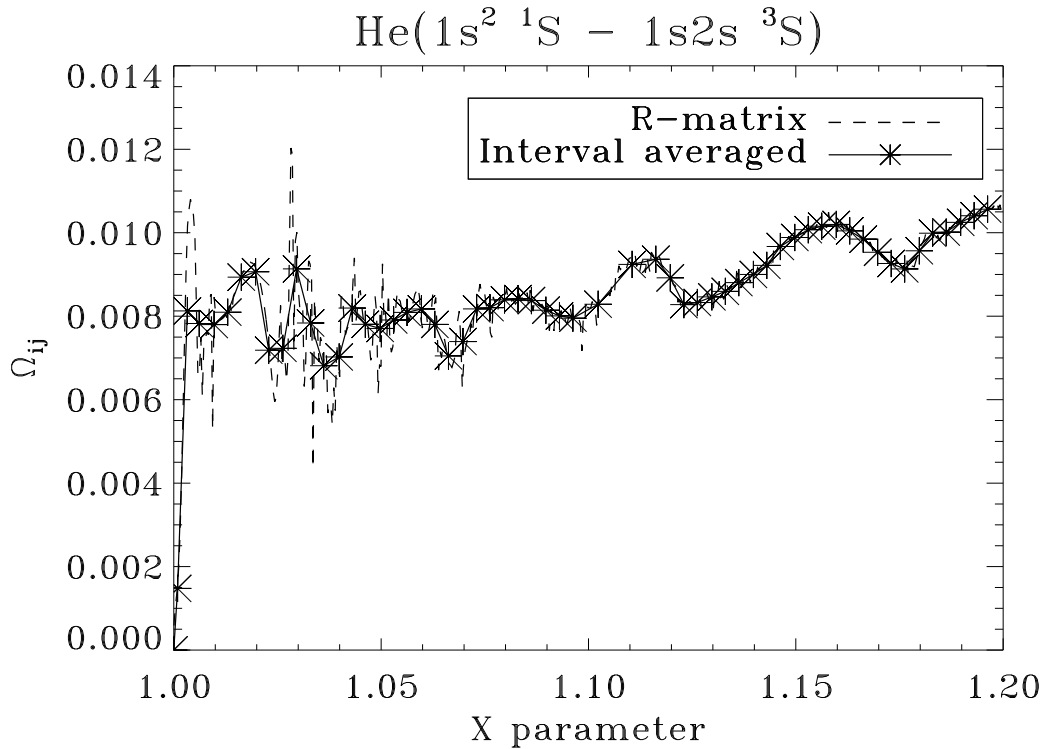


Figure 2.6: The same resonance region of the same transition in figure 2.5, but with a larger number of data points in the interval-averaged data set. One can see that the interval-averaged data set follows the variations in the R -matrix data more closely than that shown in figure 2.5, as one would expect. The objectivity of the data set is discussed in section 2.2.1. It should be noted that the oscillations at $X > 1.1$ are unphysical features caused by the pseudostates.

tity of data? This is explored in section 2.2.1.

2.2.1 Considering distribution averaging

It is appropriate at this point to introduce the different transition types briefly mentioned earlier. This consideration is essential in handling correctly the distribution averaging of collision strengths.

As the energy $E \rightarrow \infty$, the collision strength Ω tends to a simple limiting energy dependence determined by the dominant target–projectile interaction, and hence by the type of transition. The different transitions have been classified as[31]:

- Type 1 transitions are optically allowed and are induced by electric dipole interactions. The high energy behaviour of type 1 transitions is given by the Bethe approximation[98]:

$$\lim_{\varepsilon_i \rightarrow \infty} \Omega = A \ln \varepsilon_i \quad (2.13)$$

- Type 2 transitions are optically disallowed and are due to electric multipole interactions. The high energy behaviour of type 2 transitions is given by the Born approximation[99, 100]:

$$\lim_{\varepsilon_i \rightarrow \infty} \Omega = B \quad (2.14)$$

- Type 3 transitions are essentially those that are not described by types 1 or 2. In the LS coupling scheme this corresponds to a change of spin in the target system due to electron exchange. In more complex systems, transitions which would fall in to the type 3 category in LS coupling can have either dipole or Born limits, due to mixing of angular momenta, taking them into type 1 or 2. The high-energy behaviour of the type 3 transitions is given by the Ochkur approximation[101]:

$$\lim_{\varepsilon_i \rightarrow \infty} \Omega = D/\varepsilon_i^2 \quad (2.15)$$

where A , B and D are constants.

It is noted for completeness that in the case where the oscillator strength of what appears to be an electric dipole transition is very small, a slight modification of the type 1 treatment may be required; the alterations are discussed in [31]. The Burgess–Tully scaling of the collision strengths were used extensively during this work since it allows the infinite energy range to be mapped onto the finite range $[0, 1]$ ¹. The Burgess–Tully y -transformation gives the infinite-energy limit point for a transition on a finite range. This is especially valuable given, as $E \rightarrow \infty$, $\Omega \rightarrow \infty$ for an electric dipole transition. See [100]. The Burgess C parameter stretches the abscissae such that both threshold and asymptotic regions can be investigated. In the following applications of this work, the definitions of the Burgess transformations are such that C is chosen to place the ionisation threshold at $x = 0.5$.

Type 1

$$x = 1 - \frac{\ln C}{\ln(X - 1 + C)} \quad (2.16)$$

$$y(x) = \frac{\Omega}{X - 1 + e} \quad (2.17)$$

¹It is noted that a value of $x = 1$ corresponds to an infinite energy, suggesting the range should be $x \in [0, 1)$; however, the infinite energy limit point is well defined, so the range is denoted $[0, 1]$.

where $y(0) = \Omega(0)$ and $y(1) = 4S/3$ can be obtained using the Bethe approximation[98] and where S is the line strength.

Type 2

$$x = \frac{X - 1}{(X - 1 + C)} \quad (2.18)$$

$$y(x) = \Omega \quad (2.19)$$

where $y(0) = \Omega(0)$ and $y(1)$ can be obtained using the Born approximation[99].

Type 3

$$x = \frac{X - 1}{(X - 1 + C)} \quad (2.20)$$

$$y(x) = X^2\Omega \quad (2.21)$$

where $y(0) = \Omega(0)$ and $y(1)$ can be obtained using the Ochkur approximation[101].

The interval-averaging method can evidently return varying levels of congruence depending on the number of data points in the preferred energy grid, as exemplified in figures 2.5 and 2.6. In order to instill a more rigorous objectivity in deciding the number of data points in the reduced data set, we must consider how the collision strengths will be used.

In the majority of applications, one is interested in the collision strengths, Ω , when they have been averaged with a Maxwellian electron distribution function. This distribution-averaged collision strength is denoted, Υ . In order to ensure a well-defined distribution-averaged collision strength, one must consider the ‘‘energy scale lengths’’ of the interval-averaged collision strength and distribution function, which in general are low-order numerical representations.

$$\lambda_{\Omega}^{-1} = \left| \frac{1}{\Omega} \frac{d\Omega}{dX} \right| = \left| \frac{d \ln \Omega}{dX} \right| \quad (2.22)$$

and

$$\lambda_f^{-1} = \left| \frac{1}{f} \frac{df}{dX} \right| = \left| \frac{d \ln f}{dX} \right| \quad (2.23)$$

To guarantee a well-defined average is formed, so that the interval-averaged collision strength is sufficient to represent accurately the variation of the distribution function, the distribution function must vary on a longer scale length than the interval-averaged collision strength in the resonance region between the excitation and ionisation thresholds. It is important to note at this stage, the derivatives in equations 2.22

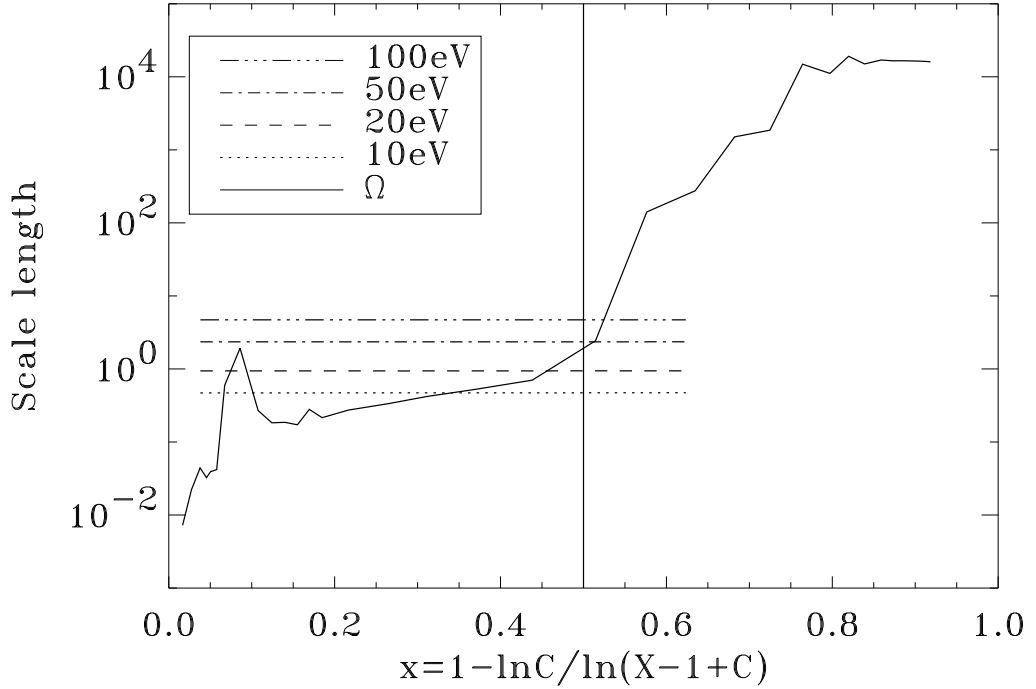


Figure 2.7: The energy scale lengths for a Maxwellian distribution at four temperatures from 10–100 eV and that of the interval-averaged collision strengths for the transition $\text{He}(1^1\text{S} - 3^3\text{P})$. The independent variable x follows the Burgess C-plot transformation, with C chosen to place the ionisation threshold at $x = 0.5$.

and 2.23 are calculated discretely on the interval-averaged collision strengths and tabulated distribution function. This results in the scale lengths being dependent on the number of data points representing a particular region. Figure 2.7 illustrates the energy scale lengths of a set of interval-averaged collision strengths and of Maxwellian distribution functions with four temperatures from 10–100 eV.

Figure 2.7 shows the scale lengths as a function of reduced energy using the Burgess x transformation given above. As previously mentioned, the test criterion for whether there will be a well-defined effective collision strength is: in the resonance region, where the collision strengths are not smoothly varying in their limiting energy dependence, $\lambda_\Omega < \lambda_f$. One can see from figure 2.7 that the criterion is satisfied for all four temperatures, except at $x \sim 0.1$.

It is therefore necessary during the interval-averaging process to calculate the scale lengths of the averaged data and compare with the scale lengths of the distribution function before forming Υ . In figure 2.7 the region around $x = 0.1$ has an interval-averaged

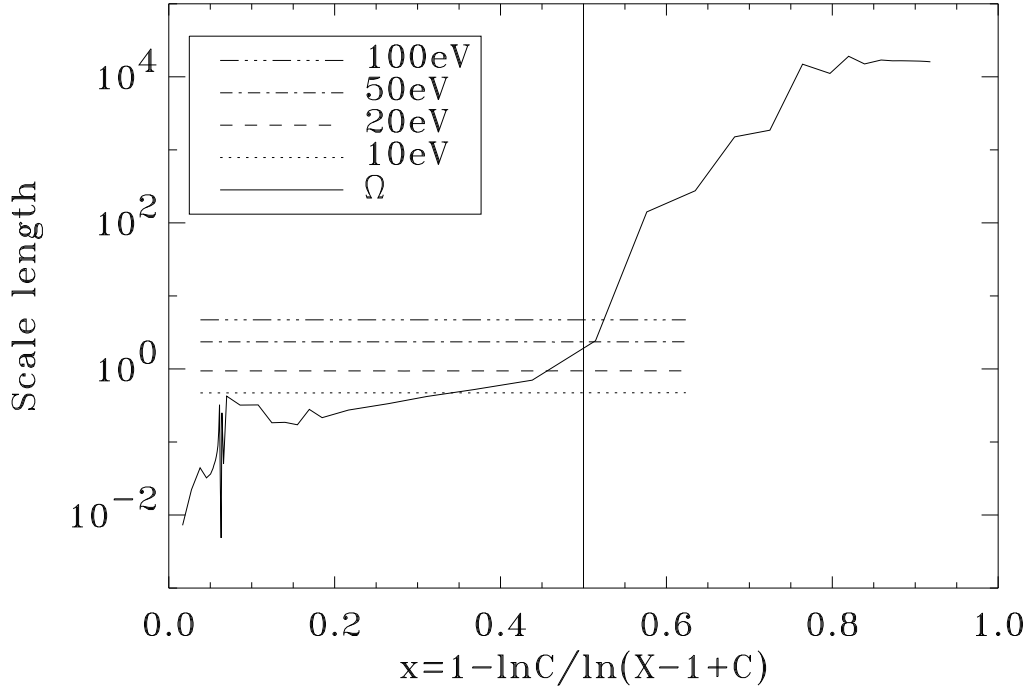


Figure 2.8: Illustrates the same data as that shown in figure 2.7 when more data points are included in the interval-averaging quadratures. This is sufficient in this case to produce well-defined effective collision strengths for temperatures greater than approximately 10 eV.

collision strength which varies on a scale length that is too long to form a well-defined average with the Maxwellian distributions at 10 eV and 20 eV. It would therefore be necessary to include more points in that vicinity during the interval-averaging process if one required effective collision strengths with Maxwellians in that temperature range. Figure 2.8 shows the outcome of adding more data in the unsatisfactory region of figure 2.7. One can see that the inclusion of extra points in this region is sufficient to reduce the scale length of the interval-averaged collision strengths to values below that of the distribution functions.

The interval-averaging process can therefore be effectively used to reduce the quantity of data archived from the tens-of-thousands of R -matrix data points to around thirty to fifty without the loss of the important physical contributions to the collision strengths from the resonance structure below the ionisation threshold. A graphical overview of the interval-averaging process is given in figure 2.9.

The preferred grid used to produce the final interval-averaged data file is defined

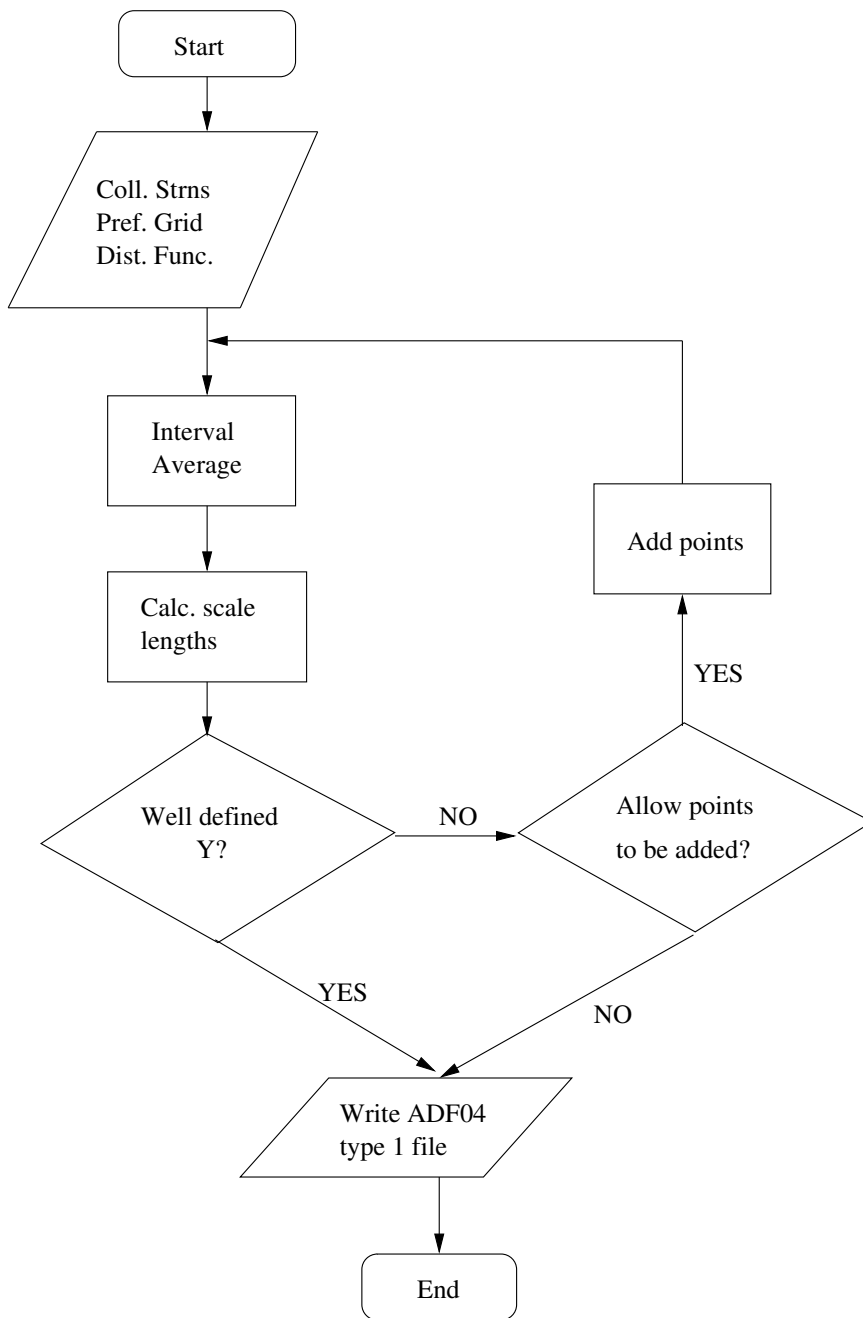


Figure 2.9: A graphical overview of the interval-averaging process. One can see how the basic number of preferred energy grid points is defined and this preferred grid can be augmented with additional data points if necessary to produce a well-defined Υ from Ω and the distribution function.

and an optional input relating to the distribution function used with the collision strengths to produce the distribution averaged collision strengths Υ are also determined. If the distribution function is not provided then a straight-forward interval-average is carried out without calculating scale lengths and Burgess transformations; the output data is on the preferred grid supplied. If a distribution function is supplied, the scale lengths of the interval-averaged collision strengths are calculated and a comparison made with the distribution function's scale lengths to determine whether a well-defined effective collision strength can be produced. If the scale lengths are such that there is a well-defined Υ , that is $\lambda_\Omega < \lambda_f$ in the resonance region, an ADF04 type 1 file is written. If $\lambda_\Omega > \lambda_f$ in the resonance region, the procedure can add extra points to the grid before calculating Υ . It should be noted that if one allows extra data points to be added to the interval-averaged data set, it will be this larger set of data that is written to the final ADF04 file. This is the best course of action given that the resonance structure below threshold could have varying degrees of influence on an effective collision strength. To illustrate this point one only has to consider the effect of taking a distribution centred on the resonance region and varying the width of the function. As the function narrows, the influence of the peaks and troughs in the resonant collision strength will manifest itself more and more to the point where a mono-energetic distribution would be fully susceptible to the variations of the resonances.

There are classes of non-Maxwellian electron distribution functions of particular interest in applied plasma physics, both in the laboratory and in astrophysical contexts. A thorough discussion of the treatment of non-Maxwellian distribution functions is given in [102]. Figure 2.10 shows a similar plot to those in figures 2.7 and 2.8, however, it shows a family of κ distributions, which are relevant to astrophysics. The plot in figure 2.10 shows how the scale lengths of the interval-averaged collision strengths compare with those of different κ distributions for a characteristic effective temperature, T_{eff} , of 50 eV. The high-energy tail associated with the κ distribution is evident. The effective temperature is defined by:

$$kT_{\text{eff}} = \frac{2\bar{E}}{3} \quad (2.24)$$

where

$$\bar{E} = \int_0^\infty E f(E) dE \quad (2.25)$$

This parameterises the κ functions in the same way the “real” temperature, T_e , parameterises a Maxwellian.

Figures 2.7 and 2.8 show the scale lengths of the Maxwellian distributions to be

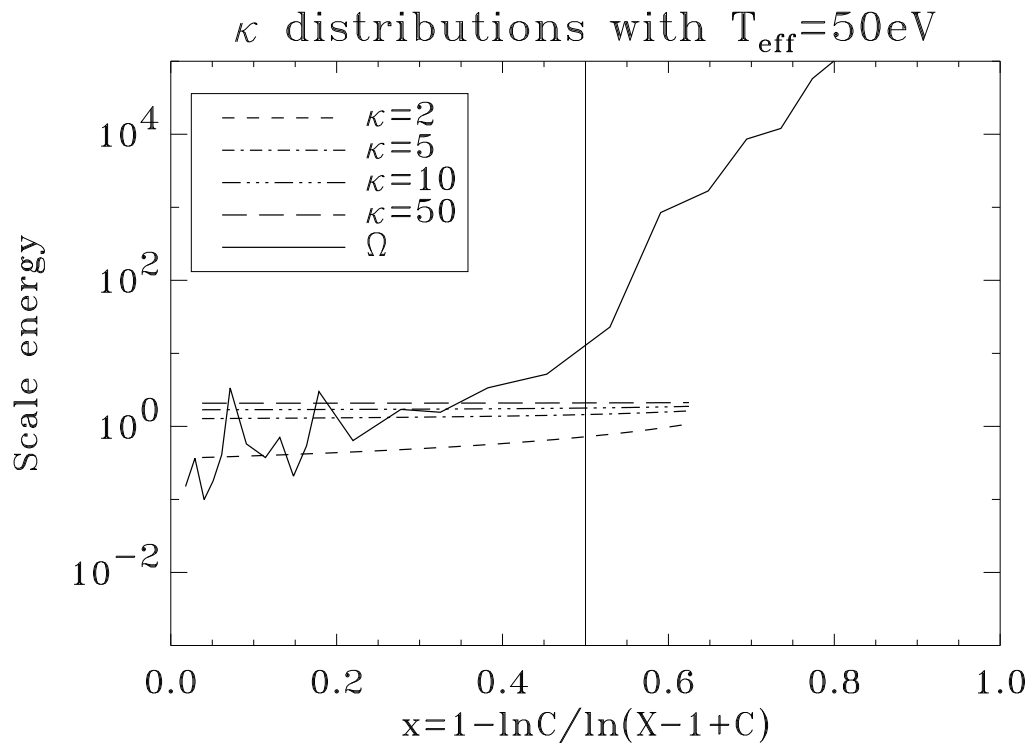


Figure 2.10: A similar comparison to those shown in figures 2.7 and 2.8 with the important difference that these curves show comparisons of scale lengths for a family of κ distributions, which are of particular relevance to astrophysical plasmas. The four distributions all have an effective temperature T_{eff} of 50 eV.

constant as a function of the reduced energy abscissa x . This is to be expected from the definition of the scale lengths given in equations 2.22 and 2.23. One can see from figure 2.10 that the non-Maxwellian κ distributions do not necessarily have a scale length which is constant with reduced energy; again, this is evident from the definition of the scale lengths. Therefore, the scale lengths themselves can be used to quantify a distribution function's deviation from the Maxwellian. From figure 2.10 one can see that the scale length of the $\kappa = 2$ case is clearly not constant, but as $\kappa \rightarrow \infty$ the κ distributions' deviation from Maxwellian tends to zero. This is not an unimportant point since the atomic physics for Maxwellian distributions of free electrons is well-defined and well understood by the plasma physics community. Therefore, it would be useful to know at what point a truly non-Maxwellian treatment of the atomic physics processes within a plasma is necessary, and where a Maxwellian approximation can be made to a reasonable degree of accuracy. The full non-Maxwellian treatment of the atomic processes is given in [27] and a discussion of the uncertainty in the atomic data is discussed in section 2.3.2 of this thesis. Figure 2.11 shows how the scale length of the κ distribution varies from low κ to the high κ Maxwellian limit for $T_{\text{eff}} = 50$ eV.

One can see from figure 2.11 that the intermediate cases form a continuum converging from low κ to the high κ limit. The constant value of the scale length corresponding to the Maxwellian with $T_e = T_{\text{eff}}$ is clearly a function of the effective temperature, that is, the width of the distribution. Therefore, if one were to choose a relatively low effective temperature, the result could be quite different from that in figure 2.11. Figure 2.12 shows the case for $T_{\text{eff}} = 5$ eV and one can see that the convergence on the high κ limit is very different from the $T_{\text{eff}} = 50$ eV case. For low T_{eff} , the scale lengths of the low κ distribution are shorter than the Maxwellian with corresponding T_e at low energies, but longer than the Maxwellian at high energies. This emphasises the point that care is needed when considering the need for a full non-Maxwellian treatment of the atomic physics relating to the processes taking place in a plasma, or if the simpler Maxwellian assumption can be made.

Section 2.2 has outlined and discussed the mathematical method of the interval-averaging technique and the implications and considerations of the technique's application to the production of distribution averaged collision strengths. Important points remain regarding archiving and analysing fundamental collision data in the context of the ADAS project. These considerations are:

- how interval-averaged R -matrix data compares with previous data sets;
- using this new data to define the 'ADAS preferred data sets';
- determining the degree of uncertainty in the fundamental data.

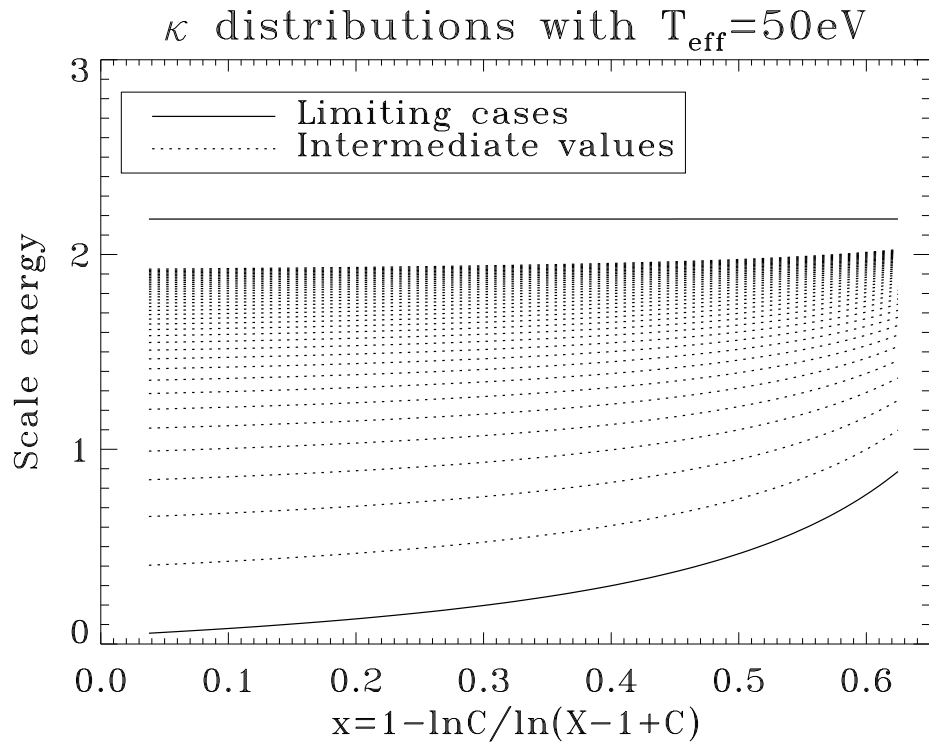


Figure 2.11: The two limiting values of low and high κ with intermediate values. It is clear that as $\kappa \rightarrow \infty$ the scale lengths tend to the constant value associated with a Maxwellian of $T_e = T_{\text{eff}}$. This is the case for $T_{\text{eff}} = 50\text{eV}$. $\kappa = 2.0$ is used to illustrate the low- κ limit.

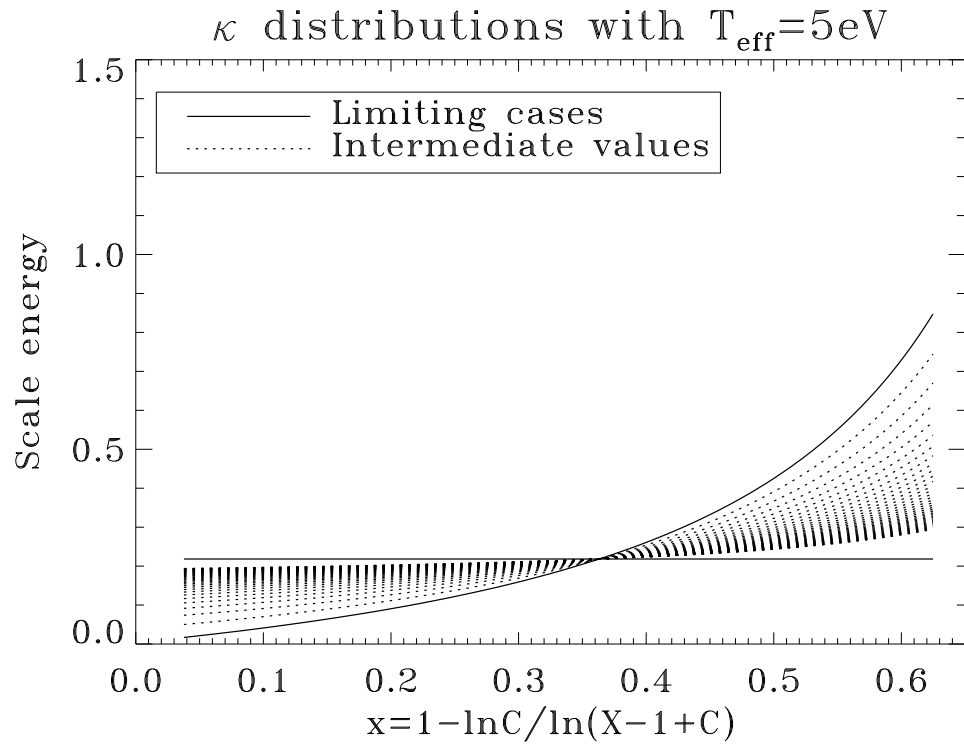


Figure 2.12: A different picture of the scale lengths' variation with κ at a relatively low effective temperature when compared with the higher effective temperature shown in figure 2.11. Again, $\kappa = 2.0$ is used to indicate the low- κ behaviour.

These points will be discussed in section 2.3.

2.3 Merged data analysis

There have been several instances since the ADAS project[56] began when the collisional excitation data for a particular ion has been reworked, leading to different generations of data. In the case of neutral helium, the original ADAS preferred data from 1993 was augmented with an improved data set in 1998[103] and again in 2000[104] before the most recent revision, carried out in support of this work, in 2003[69]. This process leads to the production of ADAS “preferred” data sets.

ADAS is made up of three sections that are available to the users of the ADAS system and a fourth that is made available to recognised developers. These sections are:

- online ADAS;
- offline ADAS;
- atomic physics database;

and

- spreadsheets for fundamental data analysis.

“Online ADAS” is a series of computer codes, with the main physics-related content written in FORTRAN and the display codes written in IDL. These series of codes can be used to interrogate ADAS data with a centrally maintained visual interface that is consistent and familiar throughout the different series. This aspect of ADAS is of particular importance when the primary purpose is using ADAS data within theoretical models; this interface allows one to inspect important atomic data used within atomic models, such as photon emissivity coefficients or ionisation rate coefficients[105].

“Offline ADAS” is used for larger-scale calculations which demand more computational power, time, and are unsuitable for interrogation in a real-time user interface environment[106, 107]. The computer codes that make up offline ADAS are largely similar to those found in online ADAS, but can contain features that allow particularly large problems to be tackled[56].

The atomic physics database contained within ADAS is one of the largest repositories of fundamental and derived atomic data in the plasma physics community[108]. It is widely used in the fields of nuclear fusion and astrophysical research by laboratories around the world, with the majority of the world’s leading fusion laboratories having access to the ADAS database[109, 110, 111].

The development work on the ADAS data sets take place within the data spreadsheets, which are made available to recognised developers, and it is these spreadsheets which were used to form the new ADAS preferred data set as a result of this work.

2.3.1 Database collision strengths

The approximations used in R -matrix collision calculations do not lend themselves to spanning the full energy range required by the ADAS data sets. For example, an R -matrix calculation is only valid to an energy half the value of the highest continuum energy used; therefore, the R -matrix with pseudostates calculation described above is inappropriate for spanning energies up to perhaps 10^5 times the excitation threshold, as is required by ADAS. The ADAS spreadsheets allow developers to visualise all of the data available for a particular transition in an ion, and merge data sets to give the best accuracy over the necessary energy range. Figure 2.13 shows the collision strength data for He($1^1S - 2^3S$) contained within the ADAS spreadsheet.

The ADAS preferred data shown in the lower plot of figure 2.13 has a very well-defined behaviour for the higher energies of $X > 2$ due to the asymptotic behaviour as the energy increases past the ionisation threshold². The spin change transition He($1^1S - 2^3S$) can be seen to tend to zero as the energy increases, as one would expect from section 2.2.1, and it is in the region $X < 2$ where the preferred data has changed over time. The upper plot of figure 2.13 shows the individual calculations on which the ADAS preferred data sets have been based. The latest neutral helium work of Ballance (2003) gives far larger emphasis to the resonance region than in previous calculations. Therefore the most recent calculation deserves consideration in this region. The fact that a calculation delivers higher resolution data in a particular energy region does not mean that the calculation is more accurate in this region, hence the need for a quantifiable measure of the uncertainty in a particular data set; this is discussed in section 2.3.2.

Given the discussion above regarding the consideration of the collision strengths' energy scale lengths compared with those of the particular distribution functions of interest, it is clear that the merging of collision strength data from different calculations to form an ADAS preferred collision strength is an incomplete treatment. The data requirement of a high T_e Maxwellian distribution can be vastly different from that of a near-mono-energetic numerically tabulated distribution, so one might wonder the rationale behind providing a data set that is of limited use to the wider ADAS commu-

²It should be noted that the x-axis of the plots in figure 2.13 is $X - 1$. This puts the excitation threshold at zero on this scale allowing the logarithmic scale to expand more fully the energy region near threshold.

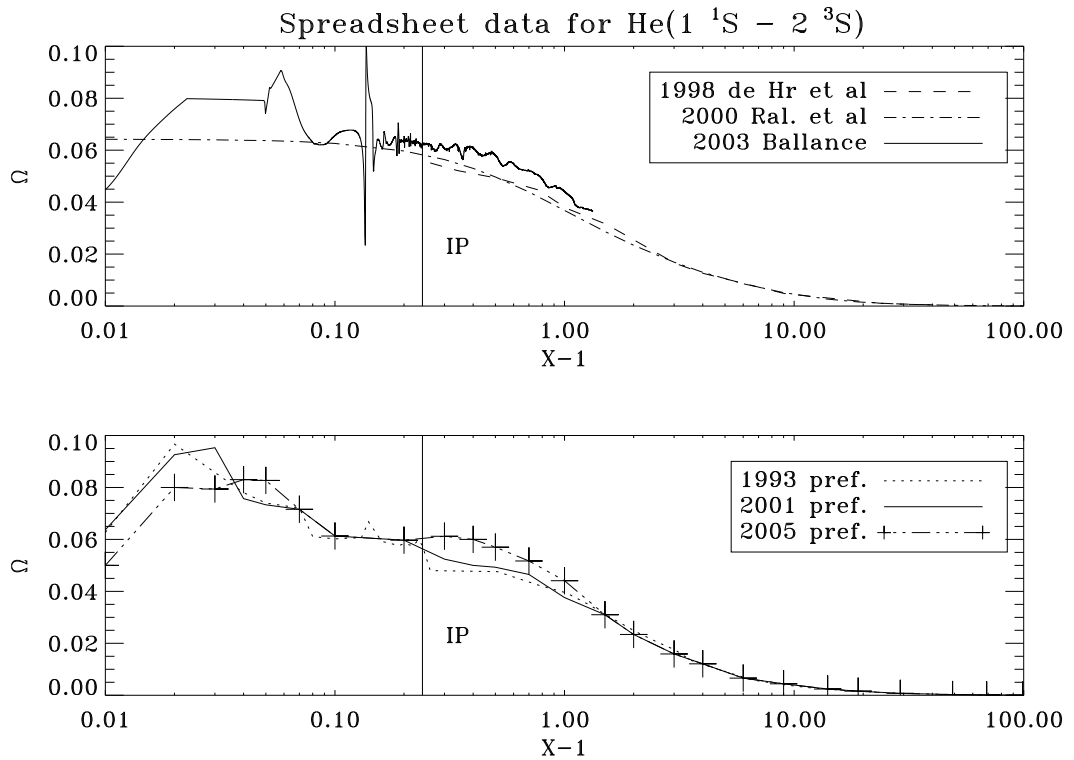


Figure 2.13: Data from the ADAS spreadsheets for the spin change transition $1^1S - 2^3S$ of neutral helium. One can see that the ADAS preferred data sets are in good agreement with one another in the high energy regime ($X - 1 > 1$), but there are variations in the data closer to the excitation threshold. The newest data set represents the resonances near threshold, but does not extend to very high energy; in this case just over twice the excitation threshold. The ionisation potential is marked 'IP' and has a value of $X - 1 \simeq 0.24$.

nity. The detailed treatment given to the data in this work means the preferred data will be appropriate for most applications, and documentation is provided at the foot of an ADF04 type 1 data set giving information on the source of the data, any processing that has been carried out and the developer who produced the data set.

2.3.2 Database uncertainty estimates

As discussed previously, different levels of approximation result in different levels of physical quality in the data that is calculated. For example, an R -matrix calculation can resolve the resonance detail near threshold whereas a distorted wave[112] calculation cannot. The distorted wave method neglects the coupling of the target and projectile electron, hence cannot directly include resonances which represent compound states in the $N + 1$ electron system. Resonances can be superimposed on distorted wave calculations using a perturbative method[89], however, they arise automatically on solving the close-coupling equations used in an R -matrix method. This does not mean R -matrix calculations can completely supplant distorted wave. Since the resonance contributions cannot be scaled along isoelectronic sequences, it is not possible to scale resonance-resolved collision strengths obtained from an R -matrix calculation, while those obtained by the distorted wave approximation can be scaled. Therefore, distorted wave is an important method in its own right and can provide convenient baseline data that is not possible with R -matrix. This raises the issue of quantifying the accuracy of a given calculation compared with other approximations and, in particular, compared with previous data sets. This is the second use of the ADAS spreadsheets.

There are several different aspects to be considered regarding the relative uncertainty in collision strength data. If two data sets have a systematic shift relative to each other then there should clearly be an uncertainty related to this shift. However, if a new data set contained resonance structure, there would be shifts from previous data sets, but the new data would more accurately represent the physical nature of the collision strengths. This indicates uncertainty related to the resonances' departure from the previous data set should have less weighting than a systematic shift.

The method used to estimate the uncertainty in a new data set depends on several steps. These are:

- determination of three “critical” points in the energy grid:
 - ionisation threshold;
 - twice the ionisation threshold;
 - five times the ionisation threshold;

- division of the energy grid using these critical points;
- determination of oscillatory behaviour of collision strength;
- calculation of the new data's deviation from previous data sets;
- compilation of information to estimate the uncertainty of the new data set.

The energy grid is divided into regions defined by the critical points; these regions refer to domains with disparate physical characteristics. The first energy region, bounded by the excitation threshold, X_e , at its lower limit and the ionisation threshold, X_i , at its upper limit, exhibits large resonances that do not exist in the other regions. In the region $[X_e, X_i]$ the resonant nature of the collision strengths means that the uncertainty cannot be evaluated using a simple calculation of the deviation. The second region $[X_i, 2X_i]$ has no resonances, but may contain oscillations at a lower frequency to those in the $[X_e, X_i]$ domain. These oscillations are non-physical artifacts of the pseudostates. The collision strengths in the region $[2X_i, 5X_i]$ behave principally as their asymptotic dependence dictates and therefore the largest component in the uncertainty calculation is due to systematic shifts in one calculation relative to another. Table 2.1 shows an excerpt from the ADAS spreadsheets for the excitation from 1^1S to 2^3S in neutral helium. The table has the three 'critical' points detailed above, and the value of the collision strength at those energies for the particular data set; in this case the 1993 ADAS preferred data set. In the case where one of these energies is not explicitly tabulated on the spreadsheet, a linear interpolation is carried out to the energy of interest.

The next part of table 2.1 shows the maximum, minimum and average values of the collision strength in the three energy domains defined by the critical points. The third part of table 2.1 gives the fractional change between the most recent data, denoted "[6]", and the 1993 ADAS preferred set, "[1]". The data is analysed in a similar way for the remaining data sets until one reaches the newest set. Table 2.2 shows another excerpt from the ADAS spreadsheets for the newest calculation. One can see that the layout of the data is similar to that in table 2.1, but rather than the third part of the table giving the fractional change in the data, it shows the maximum, minimum and average of the fractional changes given by the older data sets.

The information in the third part of table 2.2 can then be used to assemble the error estimation for the data set:

- firstly, the maximum contribution to the uncertainty was taken: this is the Max.[1-5] data in table 2.2;

[1]		
Critical points		
X	Ω	
1.241	5.79^{-2}	
2.482	3.16^{-2}	
6.203	9.04^{-3}	
Max.	Min.	Ave.
9.67^{-2}	5.75^{-2}	6.48^{-2}
5.79^{-2}	3.16^{-2}	4.50^{-2}
3.16^{-2}	9.04^{-3}	1.99^{-2}
$ [1] - [6] /[6]$		
3.30^{-2}	3.76^{-2}	1.14^{-1}
5.39^{-2}	2.73^{-3}	2.64^{-2}
2.73^{-3}	2.73^{-2}	2.64^{-2}

5.79^{-2} denotes 5.79×10^{-2}

Table 2.1: Data contained in part of the uncertainty analysis spreadsheet for neutral helium. This data is taken from the 1993 ADAS preferred data set. See text for details.

[6]		
Critical points		
X	Ω	
1.241	6.03^{-2}	
2.482	3.15^{-2}	
6.203	8.80^{-3}	
Max.	Min.	Ave.
1.00^{-1}	5.97^{-2}	7.31^{-2}
6.12^{-2}	3.15^{-2}	5.23^{-2}
3.15^{-2}	8.80^{-3}	2.04^{-2}
Max.[1-5]	Min.[1-5]	Ave.[1-5]
3.57^{-1}	3.33^{-1}	9.71^{-2}
9.90^{-2}	1.73^{-1}	1.13^{-1}
7.90^{-2}	2.24^{-1}	1.22^{-2}

6.03^{-2} denotes 6.03×10^{-2}

Table 2.2: Data contained in part of the uncertainty analysis spreadsheet for neutral helium. This is data from the newest calculation by Ballance. See text for details.

Domain	A%	B%	Ave. A&B	Meth. low	Meth. high	Final err. %
$[X_e, X_i]$	35.7	9.7	22.7	3.0	10.0	10.0
$[X_i, 2X_i]$	17.3	11.3	14.3	3.0	10.0	10.0
$[2X_i, 5X_i]$	22.4	1.2	11.8	3.0	10.0	10.0

Table 2.3: Data in the final uncertainty estimation of $\text{He}(1^1\text{S} - 2^3\text{S})$. See text for details.

Domain	A%	B%	Ave. A&B	Meth. low	Meth. high	Final err. %
$[X_e, X_i]$	81.6	10.5	46.1	3.0	10.0	10.0
$[X_i, 2X_i]$	9.2	4.4	6.8	3.0	10.0	6.8
$[2X_i, 5X_i]$	10.9	3.1	7.0	3.0	10.0	7.0

Table 2.4: Data in the final uncertainty estimation of $\text{He}(1^1\text{S} - 2^1\text{S})$. See text for details.

- secondly, the average data was taken from Ave.[1-5] in table 2.2;
- finally, these two error contributions were averaged.

This final average uncertainty is compared with values considered to be the maximum and minimum errors possible for the method of calculation and transition type[113]. If the calculated uncertainty lies below the lower limit for the calculation method or above the method's upper limit, the error is set at the corresponding limiting value. If the uncertainty lies within the bounds set for the method and transition, this value is set as the uncertainty for that particular energy region. Table 2.3 shows the detail of this, with *error A* and *error B* data coming from the first and third columns respectively of table 2.2.

One can see from table 2.3 that the lower and upper bounds on the uncertainty for the transition $\text{He}(1^1\text{S} - 2^3\text{S})$ are 3% and 10% respectively[113]. For the three energy regions defined by the critical points, the uncertainty is set to the upper limit of 10%; this is characteristic of the type 3 transition, with types 1 and 2 generally giving a lower level of uncertainty. Table 2.4 shows similar data to that contained in table 2.3, but for the non-dipole allowed type 2 transition $\text{He}(1^1\text{S} - 2^1\text{S})$. One can see that the resonance region has an uncertainty set to the limiting value of 10%, but the other two energy regions have lower uncertainties within the bounds of the method. The limiting values on the uncertainty scale with the principal quantum number of the initial state in the excitation reaction, increasing with every increase in n . That is, transitions out of $n = 2$ or $n = 3$ have larger uncertainties than those out of the ground state due to increasing uncertainties in the method used in the calculation.

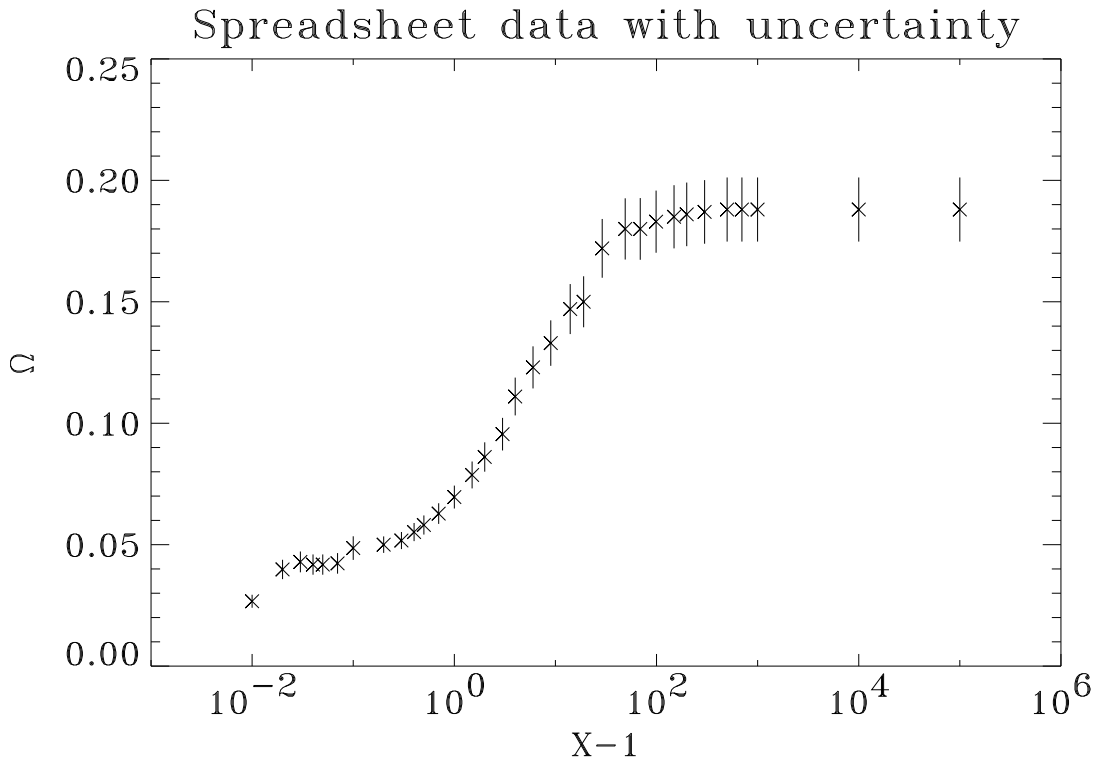


Figure 2.14: Collision strengths from the 2005 ADAS preferred data with the uncertainties included as calculated on the ADAS spreadsheets and contained in the newly defined `.err` file.

With the uncertainties calculated in the different energy domains defined by the critical points, one can attach an uncertainty to every data point contained in the ADF04 type 1 file. A new data format was created with the same format as the ADF04 type 1 file, but where there are collision strengths in the standard file, there are uncertainties in the new file. Every data set created in this way consists of two files; for example, `helike_idp04he0_t1.dat` and `helike_idp04he0_t1.err`. Therefore, for every data point in `helike_idp04he0_t1.dat`, there is a corresponding point in `helike_idp04he0_t1.err` that defines the Gaussian half-width uncertainty in that data point. Figure 2.14 shows the 2005 ADAS preferred data for the transition $\text{He}(1^1\text{S} - 2^1\text{S})$ with the uncertainty included from the corresponding `.err` file.

2.3.3 Data error propagation

The implications of the methods and details outlined in section 2.3 are far-reaching in the field of atomic modelling. The detailed collision strength data can be produced on an entirely customisable energy grid from high-resolution R -matrix data. This is com-

plemented by an equally detailed breakdown of the uncertainty in the underlying data. A theoretical uncertainty from the collision strengths, Ω , to the distribution-averaged collision strengths, Υ , and through the derived atomic reaction rate coefficients to data such as photon emissivities can be propagated using this underlying data. This allows uncertainty bars to be attached to theoretically anticipated spectra and determine directly whether models agree with experimental measurements within the accuracy of the approximations used in the fundamental calculations.

Work is on-going to allow uncertainty in fundamental electron-impact data to be carried through to an observable. A photon emissivity coefficient can be calculated from the collisional-radiative matrix, so if the fundamental data contained in the matrix — that is excitation/de-excitation rate coefficients, ionisation and recombination rate coefficients etc. — had an associated uncertainty, sampling the data from within the Gaussian uncertainties contained in the fundamental data can provide derived data with corresponding uncertainties.

The development and provision of the routines described constitute an extension to this work. With the fundamental data available and the methods described in section 2.3, they will provide an valuable tool to both theorists and spectroscopists. Section 4.4 of this thesis discusses a Monte Carlo statistical sampling routine developed to determine uncertainties in metastable populations. This routine allows one to include uncertainty in the underlying atomic data in its population evaluation. The paired collision strength and uncertainty data described above provide the starting point for an uncertainty propagation analysis.

2.4 Generalised collisional-radiative modelling

This chapter has discussed the calculation and production of fundamental data required to determine the excitation and de-excitation reaction rate coefficients for an atom or ion. The populations of different metastables of different ionisation stages directly control the spectral emission observed from a species and shall be determined for the neutral helium modelling in chapter 4.

“Generalised collisional-radiative”, or GCR, modelling deals with the modelling of excited populations of ions and the ionisation and recombination to adjacent ionisation stages in the presence of long-lived, dynamically evolving metastables[29]. In chapter 1 it was noted that the collisional-radiative lifetime of an ordinary excited state, τ_o , was less than the lifetimes of the ground and metastables states, τ_g, τ_m . For this reason the populations of the excited states are in quasi-static equilibrium with the populations of the ground and metastables states of an ion. That is to say, the population

structure of an atom or ion is defined by the local conditions in the plasma and the resultant populations of the ground and metastable states. The population statistical balance equations are:

$$C_{ij} N_j = N_e N_+ \alpha_i - \frac{dN_i}{dt} \quad (2.26)$$

This system can be partitioned into the ground and metastable part, which have a time dependence on their populations, and the excited states, which are in quasi-static equilibrium with the instantaneous population of the metastables. This creates a system of equations for generalised collisional-radiative theory which can be conveniently expressed in matrix notation. Here Greek characters indicate dynamic states, Roman characters indicate quasi-static excited states and barred symbols such as \bar{C}_{ij} indicates all quasi-static excited states.

$$\begin{bmatrix} C_{\rho\sigma} & \vdots & \bar{C}_{\rho j} \\ \cdots & \cdots & \cdots \\ \bar{C}_{i\sigma} & \vdots & \bar{C}_{ij} \end{bmatrix} \begin{bmatrix} N_\sigma \\ \cdots \\ N_j \end{bmatrix} = N_e N_+ \begin{bmatrix} \alpha_\rho \\ \cdots \\ \bar{\alpha}_i \end{bmatrix} - \begin{bmatrix} \frac{dN_\rho}{dt} \\ \cdots \\ 0 \end{bmatrix} \quad (2.27)$$

From equation 2.27 it is evident that

$$\bar{C}_{i\sigma} N_\sigma + \bar{C}_{ij} N_j = N_e N_+ \bar{\alpha}_i \quad (2.28)$$

which, upon re-arrangement, becomes

$$N_j = \bar{C}_{ji}^{-1} (N_e N_+ \bar{\alpha}_i - \bar{C}_{i\sigma} N_\sigma) \quad (2.29)$$

This shows the populations of the excited states of the ion can be determined from the ground and metastable populations, N_σ . Therefore, the entire population structure of an ion can be defined as

$$(C_{\rho\sigma} - \bar{C}_{\rho j} \bar{C}_{ji}^{-1} C_{i\sigma}) N_\sigma = N_e N_+ (\alpha_\rho - \bar{C}_{\rho j} \bar{C}_{ji}^{-1} \bar{\alpha}_i) - \frac{dN_\rho}{dt} \quad (2.30)$$

by substitution of equation 2.29 into equation 2.27.

The GCR model can be used to calculate theoretically anticipated emission from a plasma. The model and calculations relevant to this work are outlined in chapter 4. It is therefore fruitful to derive a connection between the emission from a species in the plasma and the populations calculated using the expressions in equation 2.30. From equation 2.29 one can see that the populations of the excited states are composed of

two components: an excitation component

$$X = \bar{C}_{ji}^{-1} \bar{C}_{i\sigma} N_\sigma \quad (2.31)$$

and a recombination component

$$R = N_e N_+ \bar{C}_{ji}^{-1} \bar{\alpha}_i \quad (2.32)$$

Multiplying the expression for the excited populations in equation 2.29 by the spontaneous emission, or Einstein A, coefficient gives:

$$\begin{aligned} A_{j \rightarrow k} N_j &= A_{j \rightarrow k} N_e N_+ \bar{C}_{ji}^{-1} \bar{\alpha}_i - A_{j \rightarrow k} \bar{C}_{ji}^{-1} \bar{C}_{i\sigma} N_\sigma \\ &= \left[\frac{-A_{j \rightarrow k} \bar{C}_{ji}^{-1} \bar{C}_{i\sigma}}{N_e} \right] N_e N_\sigma + [A_{j \rightarrow k} \bar{C}_{ji}^{-1} \bar{\alpha}_i] N_e N_+ \end{aligned} \quad (2.33)$$

The terms in brackets have the dimensionality of reaction rate coefficients: the bracketed term on the left is referred to as the ‘‘excitation photon emissivity coefficient’’ driven by the σ^{th} metastable, and the term on the right as the ‘‘recombination photon emissivity coefficient’’, denoted:

$$\mathcal{PEC}_{j \rightarrow k, \sigma}^{(excit.)} = -\frac{A_{j \rightarrow k} \bar{C}_{ji}^{-1} \bar{C}_{i\sigma}}{N_e} \quad (2.34)$$

$$\mathcal{PEC}_{j \rightarrow k}^{(recom.)} = A_{j \rightarrow k} \bar{C}_{ji}^{-1} \bar{\alpha}_i \quad (2.35)$$

ADAS[56] is used to calculate the photon emissivity coefficients for a particular spectral line for given electron temperature and density in the plasma. Using the GCR picture outlined in this section, it is possible to model the evolving populations of the dynamic metastable states and, further, calculate the populations of the quasi-static excited states which are in instantaneous equilibrium with the metastable states.

At this stage we will consider the timescales of the atomic processes that can change the population structure of an atom or ion to determine their relevance to this work. As mentioned briefly in chapter 1, the main atomic processes that drive the population structure, and hence emission, in a tokamak are excitation, de-excitation, ionisation and recombination. We will now consider the time scales associated with these processes starting with those which couple adjacent ionisation stages.

Consider the time scale of a typical ionisation from the ground state of helium. Using the central ADAS collisional-dielectronic ionisation rate coefficient shown in figure 2.15 and collisional-dielectronic recombination coefficient to the ground state,

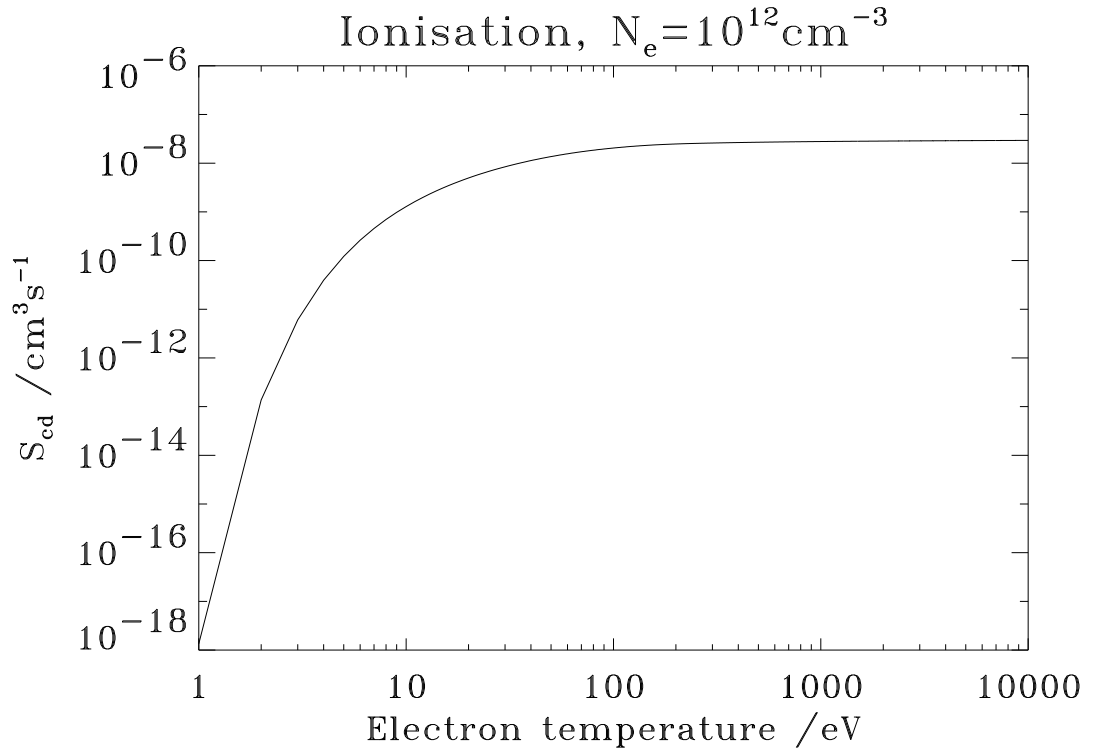


Figure 2.15: Central ADAS collisional-dielectronic ionisation rate coefficient out of the ground state of neutral helium.

shown in figure 2.16, it is possible to deduce approximate values for the time scales of the ionisation and recombination processes.

The reaction rate coefficients for helium shown in figures 2.15 and 2.16 show the variation with temperature of the ionisation and recombination at an electron density of $N_e = 1 \times 10^{12} \text{cm}^{-3}$. If one takes typical MAST plasma edge conditions, with an electron temperature of 10 eV, a typical ionisation rate coefficient of $1 \times 10^{-9} \text{cm}^3 \text{s}^{-1}$ and a typical recombination rate coefficient of $1 \times 10^{-13} \text{cm}^3 \text{s}^{-1}$, a typical time scale can be calculated for each of these two processes:

$$\tau_{scd} \simeq (S_{CD} \times N_e)^{-1} \simeq 10^{-3} \text{ s} \quad (2.36)$$

$$\tau_{acd} \simeq (\alpha_{CD} \times N_e)^{-1} \simeq 10 \text{ s}$$

It can be seen that the time scale of the recombination process is several orders of magnitude longer than that of ionisation. The He^+ population created by direct ionisation of the neutral gas puff is swept away from the region of observation by the magnetic fields. There is subsequently negligible background He^+ population in the

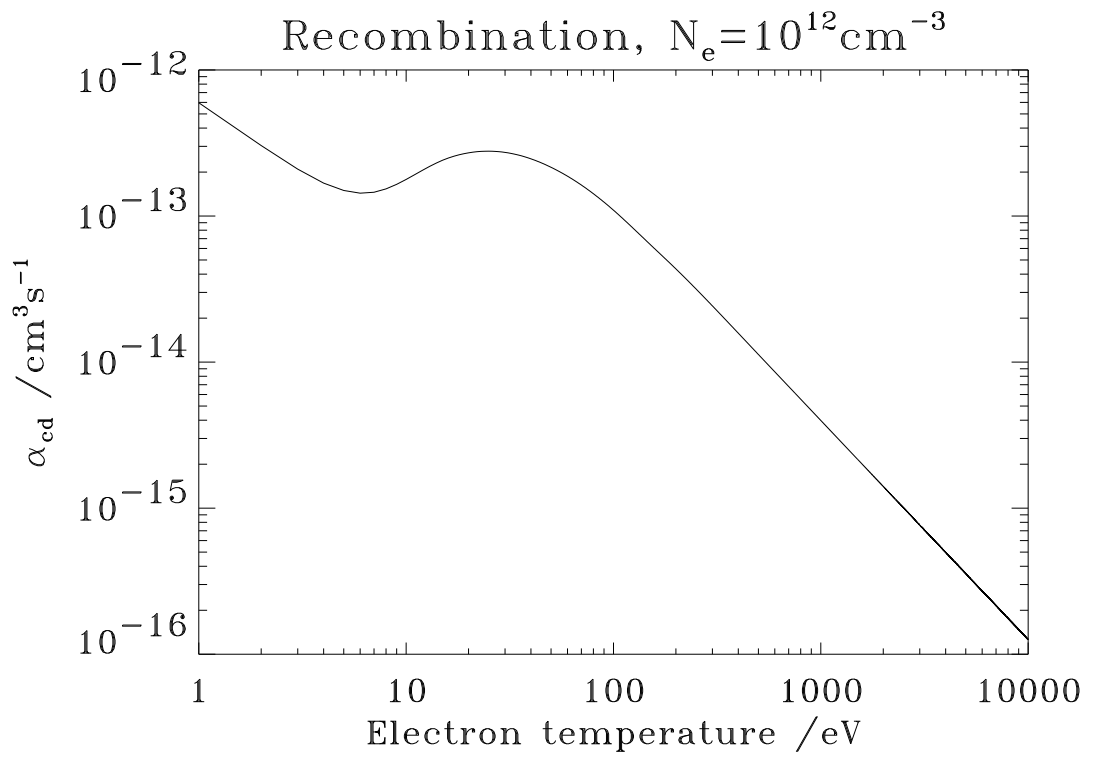


Figure 2.16: Central ADAS collisional-dielectronic recombination rate coefficient populating the ground state of neutral helium.

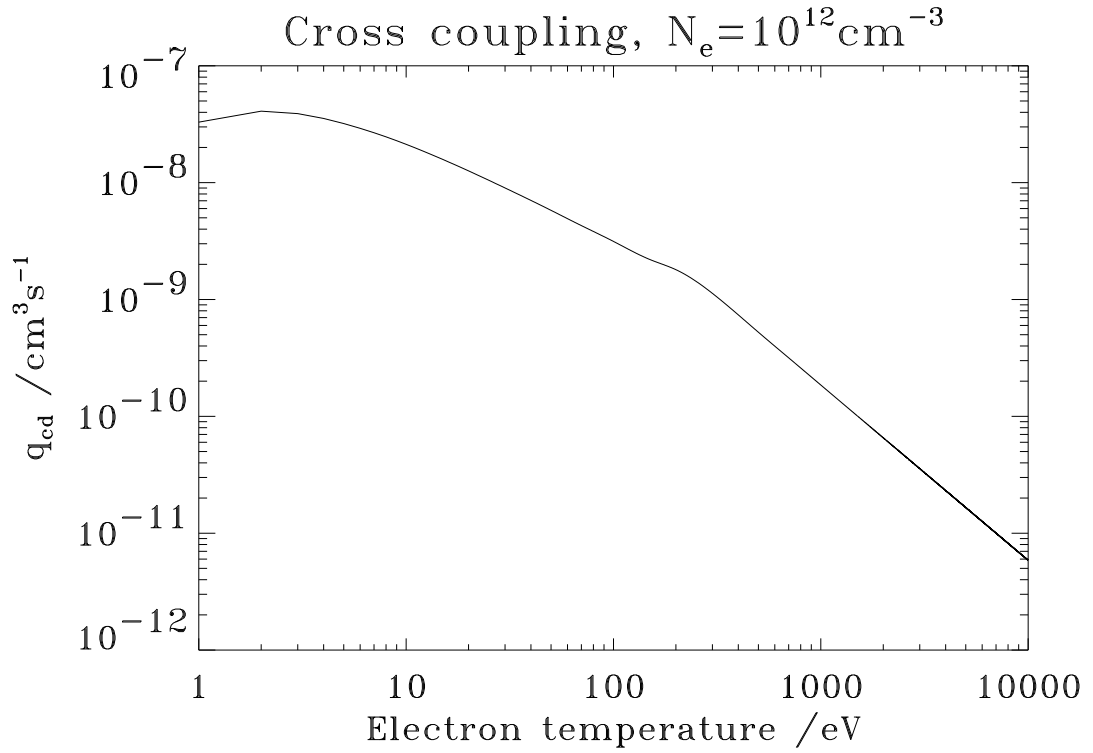


Figure 2.17: Central ADAS metastable cross-coupling coefficient for neutral helium which populates the ground state from the $1s2s\ ^3S$ state at $N_e = 10^{12}\text{cm}^{-3}$.

vicinity of the gas puff.

Now consider the processes which couple states within an ionisation stage. From the discussion above, it is clear that the population structure of an ionisation stage is dictated by the metastables' populations. Therefore, the reaction rates that are of interest are those which couple the $1\ ^1S$ and $2\ ^3S$ states of neutral helium. Again, using the central ADAS reaction rate coefficients which cross-couple the metastables of neutral helium, it is possible to deduce approximate values for the time scales for the process. Figure 2.17 shows the cross-coupling rate coefficient which de-populates $1\ ^1S$ to populate $2\ ^3S$ state and figure 2.18 shows the reaction rate coefficient which populates $1\ ^1S$ from $2\ ^3S$.

Figures 2.17 and 2.18 show the variation with temperature of the metastable cross-coupling reactions in neutral helium at an electron density of $N_e = 1 \times 10^{12}\text{cm}^{-3}$. If one takes a typical electron temperature of 10 eV, then a typical rate coefficient is $1 \times 10^{-9}\text{cm}^3\text{s}^{-1}$. Thus the time scale can be calculated:

$$\tau_{cc} \simeq (q_{cc} \times N_e)^{-1} \simeq 10^{-5} \text{ s} \quad (2.37)$$

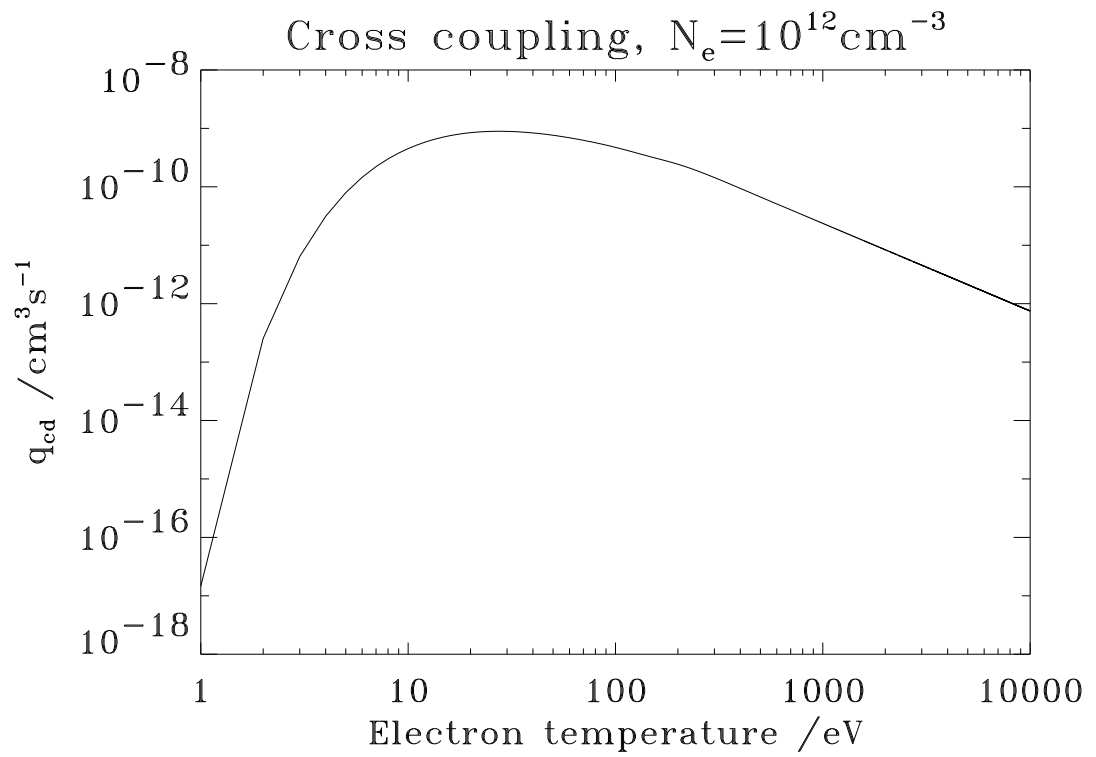


Figure 2.18: Central ADAS metastable cross-coupling coefficient for neutral helium which populates the $1s2s \ ^3S$ state from ground at $N_e = 10^{12} \text{cm}^{-3}$.

where τ_{cc} is the time scale for cross-coupling of the metastables. The time scales given in equations 2.36 and 2.37 show that the cross-coupling and ionisation processes take place on a far shorter time scale than the recombination reactions. This justifies neglecting the recombination process when modelling the HeI emission at the plasma edge. Section 4.4 will discuss how the atomic processes detailed above are combined to form the collisional-radiative matrix, and subsequently used in modelling the population evolution of the neutral helium at the MAST plasma edge.

2.5 Conclusions

This chapter has outlined the work undertaken in fundamental data calculation, processing and application. The main points of note are:

- in general application, collision strength and distribution function scale lengths must be considered (section 2.2.1);
- determining Υ for non-Maxwellian distribution functions or low-temperature plasmas may require Ω tabulations that are not ADAS standard;
- the method of interval-averaging allows the large R -matrix data sets to be reduced to a tabulation appropriate to the distribution function and physical regime;
- objective analysis is required to produce the ADAS preferred collision strength data (section 2.3.1);
- uncertainty estimates on the fundamental electron impact data will allow error propagation through to derived atomic reaction rates (sections 2.3.2 and 2.3.3);
- the fundamental data discussed in this chapter can be directly applied to GCR modelling.

Although no plasma physics analysis or experimental work was presented in this chapter, it forms the base for a discussion of the experimental work carried out in chapter 3 and for the specific GCR modelling of the physics underlying the HELIOS diagnostic in chapter 4.

This chapter outlines a framework for taking high resolution R -matrix data sets and providing ADF04 type 1 files that can be archived within the ADAS database structure. It also discusses the method of providing the collision strength data in a tabulation tailored to a specific distribution function, which is of particular interest in both

astrophysical and technical plasmas, where electron distribution functions cannot be adequately described by a Maxwellian. The implications for carrying out distribution averages at low temperatures are discussed along with a method of treating these plasma conditions safely.

A framework is set out which estimates the uncertainty in the fundamental ADF04 data, which forms a new data set within ADAS, allowing uncertainties to be propagated through an entire GCR model to give uncertainties on the final observable. This chapter provides useful deliverables for spectroscopists and theorists in terms of plasma models and the atomic data used to underpin them. The detailed electron-impact data discussed in this chapter will support the spectral emission modelling and related analyses outlined in chapter 4.

Chapter 3

Helium gas puff experiments on MAST

The helium gas puff experiments carried out for this work took place over two experimental sessions in August 2004 and February 2005. The main aims were to obtain measurements which, when combined with appropriate atomic modelling, could be used to:

- verify consistency and estimate uncertainty in comparison of measured emission and theoretical emissivity modelling using new high precision cross-section data;
- establish sensitivity and emission de-localisation due to He(1s2s ³S) metastable formation outside the plasma edge and emission “wrapping around” the plasma edge;
- deduce the angular spread of the gas puff by combining spectral emission measurements and predictive spatial emission modelling;
- establish a globally optimised diagnostic procedure for local N_e and T_e radial profiles.

The exploitation of HeI spectral line ratios at visible wavelengths from a thermal puff into the low-field edge plasma for N_e and T_e diagnosis is both desired and attempted in many fusion laboratories but remains unreliable. The technique requires accurate theoretical modelling of the line emissivities and its applicability is limited by beam divergence, the dynamic character of both the helium ground and metastable populations, and the uncertain nature of the latter population when the gas encounters the plasma. The HELIOS system posed most of these questions, but also provided the

Line	Wavelength / Å	Transition
1	6678	He (1s2p ¹ P – 1s3d ¹ D)
2	7067	He (1s2p ³ P – 1s3s ³ S)
3	7283	He (1s2p ¹ P – 1s3s ¹ S)

Table 3.1: Table of diagnostically relevant HeI emission lines observed by the HELIOS spectrometer.

opportunity to investigate them by taking advantage of MAST’s diagnostic flexibility and high resolution Thomson scattering system.

A validated diagnostic procedure would be of general benefit to the fusion community, allowing the use of the system in dynamic plasma situations and also underpinning thermal helium modelling and spectral observations in divertor and edge plasmas. This chapter will describe all aspects of the experimental work carried out for analysis with the population and emission modelling described in chapter 4. It will discuss the experimental hardware and its calibration, as well as the plasma configuration required for the pulses. The session planning will be discussed along with the rationale behind choosing a particular plasma configuration. The pulses will be summarised and the scientific outcomes discussed. The HeI emission lines measured by the HELIOS spectrometer are given in table 3.1.

3.1 Neutral helium gas injection

The neutral helium is introduced to the low-field edge of MAST through a subsonic nozzle attached to a reciprocating probe, in a configuration similar to that used at UKAEA Culham on the COMPASS-D tokamak[114], and at Forschungszentrum Jülich on TEXTOR[115, 116].

The reciprocating probe (RP) allows the source of the diagnostic helium to be moved to best suit the plasma conditions. The specific setup used during the experiments and the plasma conditions chosen will be discussed in section 3.3.

The helium gas is delivered to the injection nozzle via a 2.5 m long tube with a 3 mm bore. The conductance of a long tube in the laminar flow regime¹ is proportional to the mean pressure in the tube \bar{P} such that[117]

$$C_{\text{lam.}} = \frac{\pi d^4}{128\eta L} \bar{P} \quad (3.1)$$

and the throughput, Q , is defined as

¹Laminar flow will be assumed at this point and confirmed by calculation of the Reynolds number.

$$Q = \bar{P} C_{\text{lam.}} \quad (3.2)$$

where d is the tube bore, L is the tube's length and η is the gas viscosity. The gas viscosity of helium at a temperature of 300 K is $\eta_{\text{He}} = 1.924 \times 10^{-5}$ Pa.s and the molar density is $\rho_{\text{M,He}} = 4.003$ gram.mol⁻¹ [118]. The gas density is given by

$$\rho = \frac{\bar{P}m}{kT} \quad (3.3)$$

where m is the mass of a helium atom, k is the Boltzmann constant and T the temperature. The efflux of gas from the nozzle is given by

$$\dot{N} = C_{\text{lam.}} \frac{\rho}{\rho_{\text{M,He}}} N_A \quad (3.4)$$

where N_A is Avogadro's number. For a reasonable HeI signal to be detected, an efflux of $\dot{N} \geq 10^{19}$ atoms per second is required[119]. The mean pressure in the pipe is therefore calculated as

$$\begin{aligned} \bar{P} &\geq \left[\frac{\dot{N} \cdot 128\eta L k T \rho_{\text{M,He}}}{\pi d^4 m N_A} \right]^{1/2} \\ \bar{P} &\geq 10^3 \text{ Pa} = 10 \text{ mb} \end{aligned} \quad (3.5)$$

with a pressure twice this value, 20 mb, required to sustain the flow.

This means the throughput corresponding to an efflux of 10^{19} atoms per second is

$$\begin{aligned} Q &= \bar{P} C_{\text{lam.}} \\ Q &= 4.14 \times 10^{-2} \text{ Pa.m}^3.\text{s}^{-1} = 0.414 \text{ mb.l.s}^{-1} \end{aligned} \quad (3.6)$$

The mean free path of the helium atoms in the gas injection nozzle can be calculated as[120]

$$\lambda = \frac{2\eta}{\rho v} = \frac{2\eta}{\bar{P}} \left(\frac{\pi k T}{8m} \right)^{1/2} = 19.04 \text{ } \mu\text{m} \quad (3.7)$$

Finally, the Knudsen number[121], Kn , for the flow through the pipe can be calculated from the mean free path as

$$\text{Kn} = \frac{\lambda}{d} \simeq 6 \times 10^{-3} \quad (3.8)$$

which means means the flow through the pipe is viscous rather than molecular. As mentioned above, these calculations have assumed that the flow is laminar. To determine whether the viscous flow is laminar or turbulent we must calculate the Reynolds

Criterion	Viscous		Transition	Molecular
	Turbulent	Laminar		
Kn	Kn < 0.01		1 > Kn > 0.01	Kn > 1.0
Re	Re > 2200	Re < 1200	—	—

Table 3.2: Criteria for determining the gas flow regime in a pipe of circular cross-section.

number, Re , which gives

$$Re = \frac{\rho dv}{\eta} = \frac{\bar{P}d}{\eta} \left(\frac{8m}{\pi kT} \right)^{1/2} \simeq 315 \quad (3.9)$$

and shows that the flow is, indeed, laminar. Table 3.2 shows the criteria for checking the gas flow regime in a pipe of circular cross-section, such as the one used in the gas injection system.

The helium injection nozzle was designed to serve two distinct purposes: to deliver the gas to diagnose a short pulse, ~ 200 ms; and be used to diagnose longer pulses ~ 1 s. In the case of the short pulse, the throughput must increase rapidly from zero and decay slowly over the 200 ms period. This is achieved using a piezoelectric valve at the entrance to the feed tube, which can deliver a throughput of $Q_{in} = 50$ mb.l.s $^{-1}$ when the valve is opened for a period of approximately 3 ms. The throughput is related to the average pressure and volume by

$$Q = \frac{d}{dt} (\bar{P}V) \quad (3.10)$$

which becomes

$$Q = V \frac{d\bar{P}}{dt} \quad (3.11)$$

since the volume of the apparatus is fixed at 17.7 cm 3 . The differential equation used to give the time dependence of \bar{P} , and hence Q , is

$$\frac{d\bar{P}}{dt} = \frac{1}{V} (Q_{in} - 2\bar{P}C) \quad (3.12)$$

where the expression for the tube's conductance in the transition region is used[118]; see table 3.2:

$$C_{tr.} = C_{lam.} + J C_{mol.} \quad (3.13)$$

where $C_{tr.}$ is the conductance in the transition region, $C_{lam.}$ the laminar conductance, $C_{mol.}$ the conductance in the molecular regime, given by

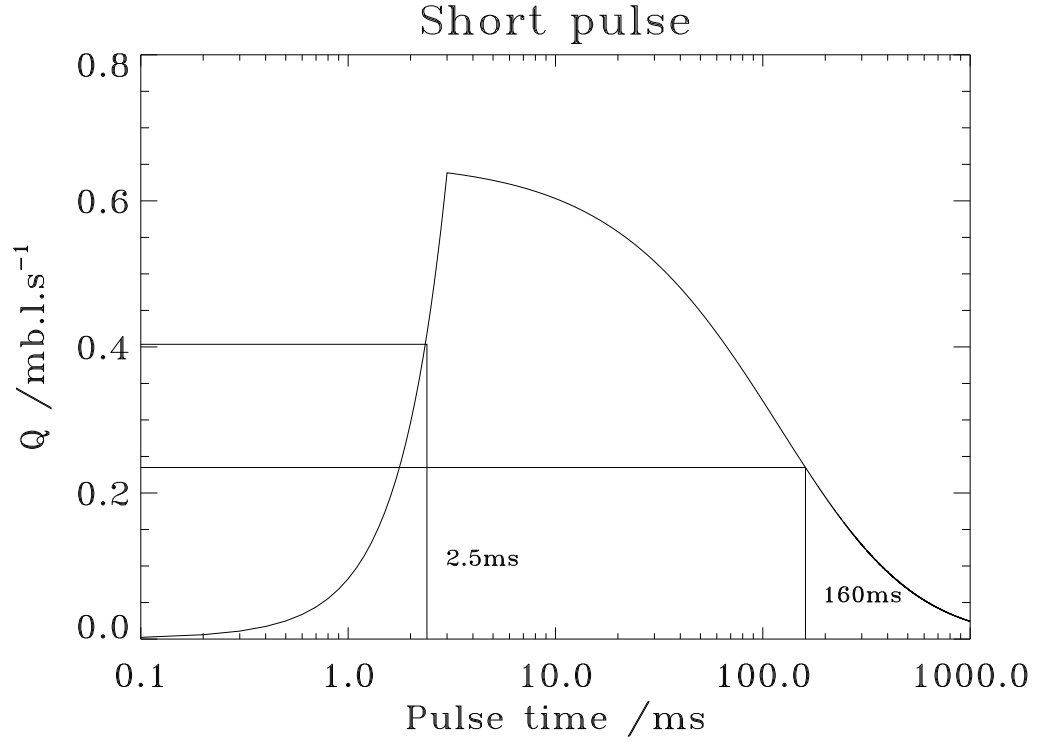


Figure 3.1: Evolution of the throughput Q as a function of time after the piezoelectric valve is opened. The $1 - 1/e$ and $1/e$ ramp-up and ramp-down times are marked.

$$C_{\text{mol.}} = \frac{16}{3} \left(\frac{kT}{2\pi m} \right)^{1/2} \left(\frac{\pi d^2}{4} \right)^2 \frac{1}{\pi d L} \quad (3.14)$$

and J is given by

$$J = \frac{1 + (d/\eta) (m/kT)^{1/2} \bar{P}}{1 + 2.47 (d/2\eta) (m/kT)^{1/2} \bar{P}} \quad (3.15)$$

$$\Rightarrow J = \frac{1 + 2.507 (d/2\lambda)}{1 + 3.095 (d/2\lambda)}$$

Equation 3.12 was solved numerically using a fourth order Runge–Kutta routine with

$$Q_{\text{in}} = \begin{cases} 50 \text{ mb.l.s}^{-1}, & 0 \leq t \leq 3 \text{ ms} \\ 0 \text{ mb.l.s}^{-1}, & t > 3 \text{ ms} \end{cases} \quad (3.16)$$

and an initial value of $\bar{P} = 0$ mb since the nozzle is at the MAST vacuum pressure. Figure 3.1 shows how the throughput varies for the short MAST pulse.

The $1 - 1/e$ rise time of 2.5 ms and the $1/e$ decay time of ~ 160 ms means this type of gas puff is well suited to a short pulse where the user is only interested in a temporal range of around 200 ms.

The average throughput, \bar{Q} , in the range $t \in [0, 200]$ ms is given by

$$\bar{Q} = \frac{1}{\Delta t} \int_0^{\Delta t} Q dt = \frac{1}{0.2} \int_0^{0.2} Q dt \simeq 0.4 \text{ mb.l.s}^{-1} \quad (3.17)$$

which is around the throughput calculated above, corresponding to a flux of 10^{19} atoms per second leaving the nozzle.

The piezoelectric valve on its own is not suitable for delivering a more sustained puff of gas because the volume of the nozzle is such that the $1/e$ decay time would be shorter than one would require. It is necessary to include a reservoir volume between the piezo valve and the nozzle feed tube. For a throughput of 0.4 mb.l.s^{-1} to leave the nozzle, an input pressure of 20 mb is required, as calculated above in equation 3.5. A reservoir volume of 56 cm^3 added to the gas puff apparatus delivers a decay time of around 560 ms. A 16 ms pulse of 50 mb.l.s^{-1} from the piezo was used to fill the reservoir to the required pressure of 20 mb. A pneumatic valve was then used to allow the gas in the reservoir to transit the nozzle to the vacuum chamber. The differential equation governing the evolution of the pressure, and hence throughput, is

$$\frac{d\bar{P}}{dt} = \frac{-2\bar{P}C}{V} \quad (3.18)$$

and the numerical solution to this equation with an initial pressure of $2\bar{P} = 20$ mb is shown in figure 3.2.

As before, the average throughput, \bar{Q} , in the range $t \in [0, 1]$ s is given by

$$\bar{Q} = \frac{1}{\Delta t} \int_0^{\Delta t} Q dt = \int_0^1 Q dt \simeq 0.4 \text{ mb.l.s}^{-1} \quad (3.19)$$

which, again, gives the necessary flux into MAST over the period of interest.

Figure 3.3 shows the throughput for MAST shot #12209. For this particular pulse, the HELIOS diagnostic was set to record data in the temporal range $t \in [50, 370]$ ms and the average throughput during this range was $Q \simeq 0.4 \text{ mb.l.s}^{-1}$, as required. The time taken for the $1 - 1/e$ ramp in throughput means that the gas flow has reached the required level when the diagnostic starts taking data at 50 ms and the $1/e$ ramp down time shows that the gas flows at the required level well after the the region of interest. Figure 3.4 shows the shot ending after approximately 330ms, compared to the much longer $1/e$ ramp down time of ~ 820 ms. The inboard injection nozzle, which

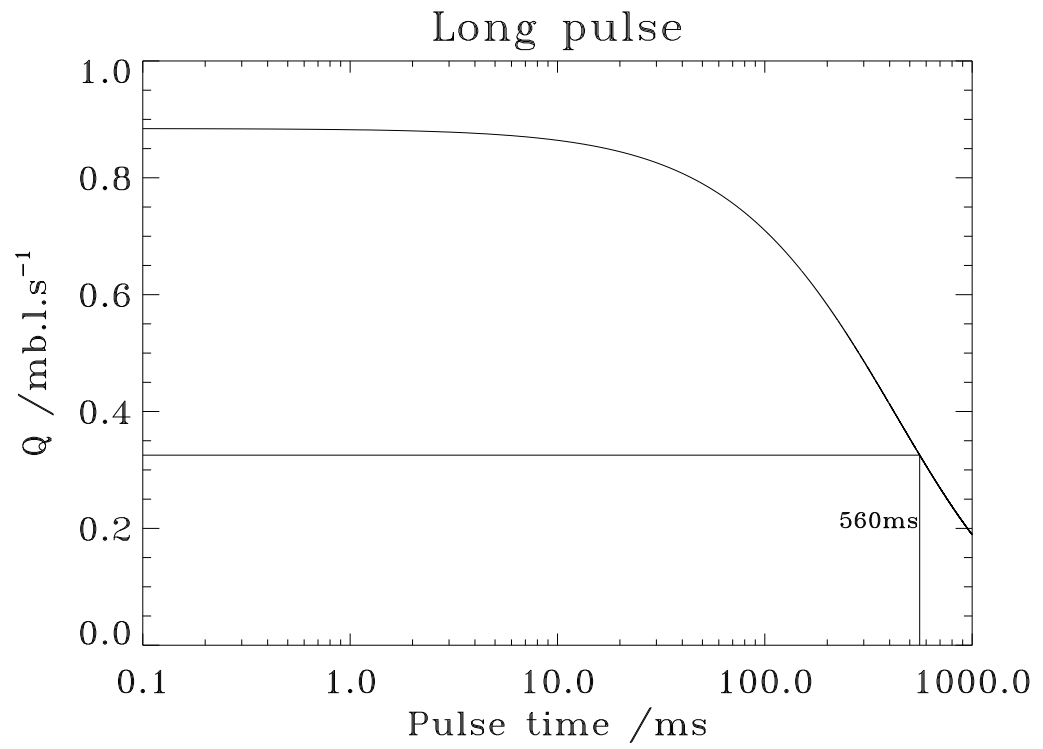


Figure 3.2: Evolution of the throughput Q as a function of time after the pneumatic valve between the reservoir and the nozzle feed tube is opened. The $1/e$ decay time is marked.

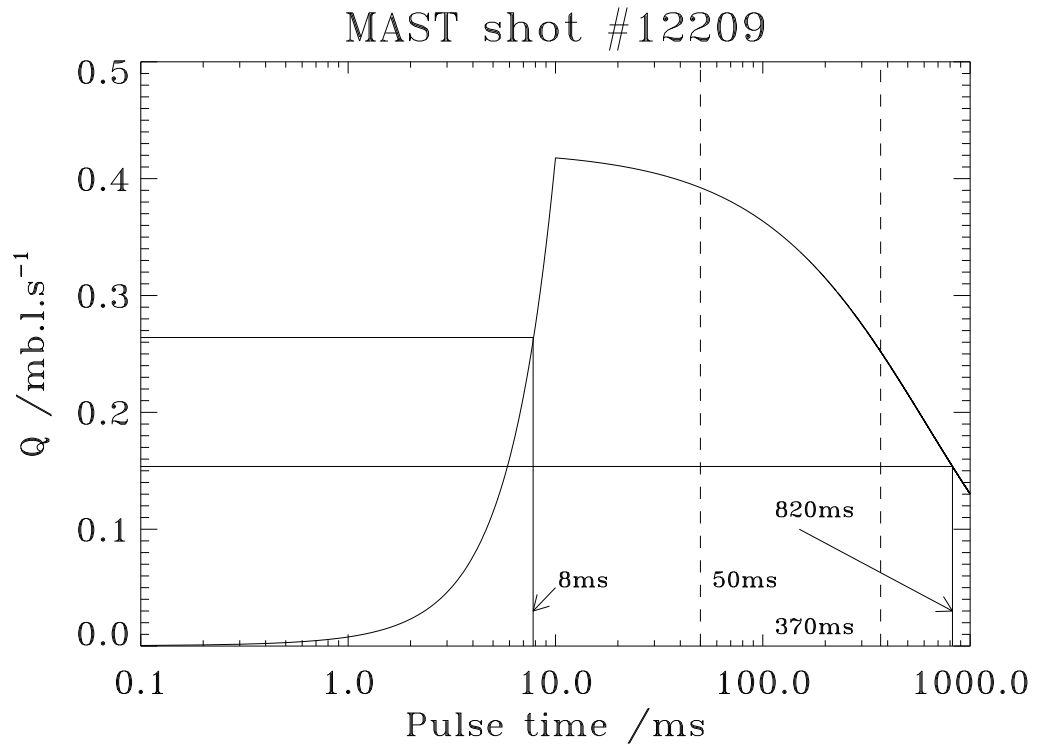


Figure 3.3: The calculated helium throughput for MAST shot #12209. HELIOS was set to record data in the temporal region $t \in [50, 370]$ ms, indicated by the vertical dashed lines, and the average gas flow in this range is ~ 0.33 mb.l.s $^{-1}$, in the vicinity of the required value of $Q \simeq 0.4$ mb.l.s $^{-1}$. The $1 - 1/e$ and $1/e$ ramp up and decay times are 8 ms and 820 ms respectively.

is nested on the central column of MAST, can be used to inject trace helium or, as was the case during this campaign, to inject deuterium. It is worth noting that the inboard injector has a fast-ion gauge attached, which can accurately measure the throughput of the nozzle[122]. This would be a useful addition to the outboard system, however, the outboard nozzle's mounting on the RP makes this more difficult. Therefore, fast-ion gauge measurements were not available during the campaign.

The gas injection system is controlled using a waveform which drives the valve connected to the nozzle's feed tube. Varying the time this valve is open determines the quantity of gas released and the profile of the gas flow. Figures 3.5 and 3.6 show the pulses sent to the programmable logic controller (PLC) and piezoelectric valve. These figures are present here for completeness and were concerned with avoiding saturation of the HELIOS detector during the experiments. This issue was directly addressed during the second phase of experiments, since saturation was observed during the first session. The performance of the piezoelectric valve was problematic towards the be-

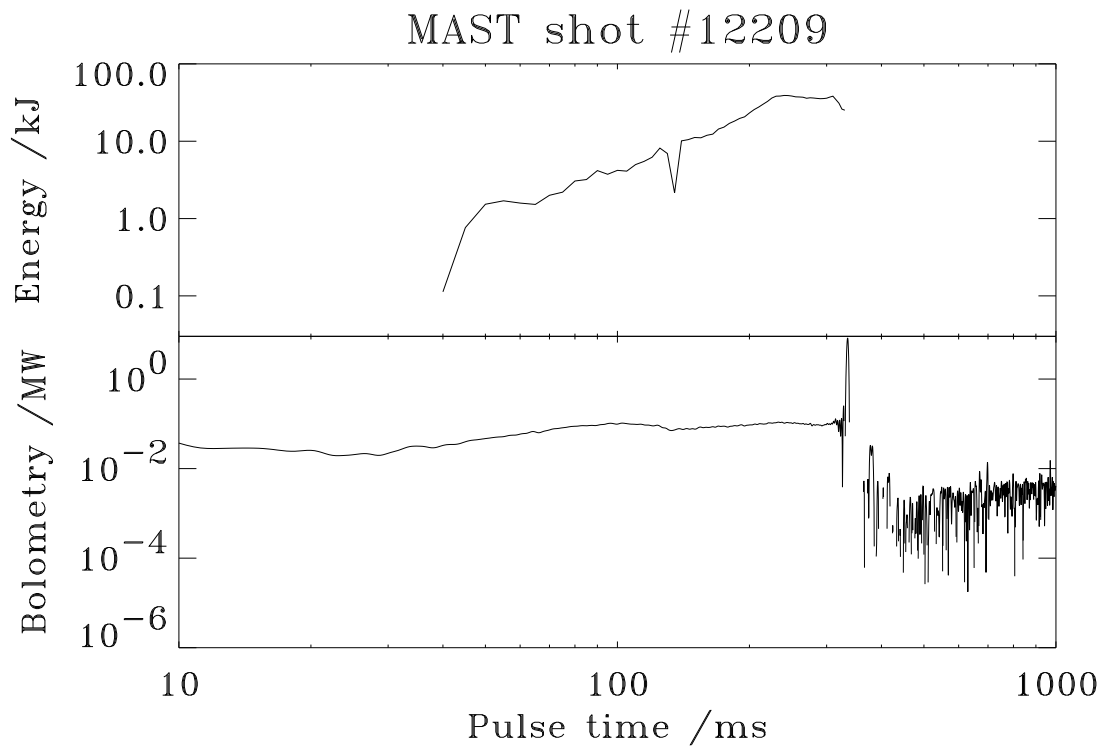


Figure 3.4: The termination of the MAST plasma for shot #12209. The upper plot shows the confined plasma energy which decreases after approximately 300 ms; this correlates with a large bolometry signal, shown in the lower plot, indicating the plasma has terminated.

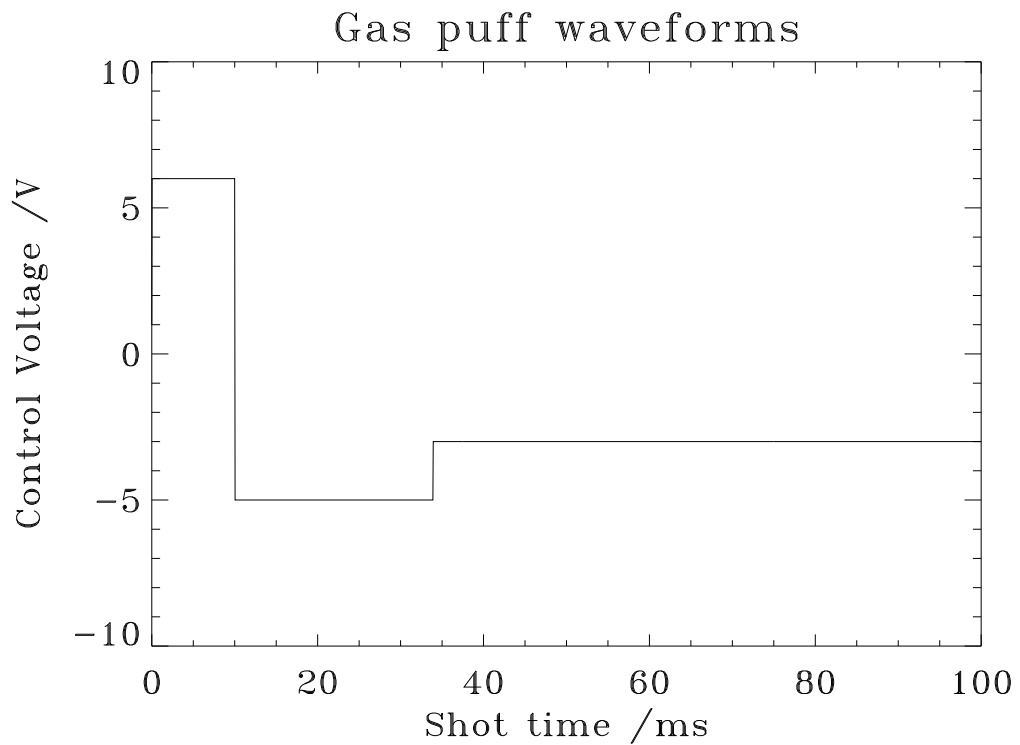


Figure 3.5: The low-voltage waveform sent to the PLC from the session leader’s panel in the control room. This signal is amplified and sent to the piezoelectric valve at the opening to the gas injection system, shown in figure 3.6.

gining of the second experimental session. The applied waveforms failed to result in the proper opening and closing of the valve. This was rectified by applying larger voltages than would regularly be the case to force the valve fully open and fully closed as required.

This section has outlined the studies and work carried out on the gas injection system prior to the execution of the HELIOS validation experiments. Sections 3.2, and 3.3 continue the discussion of the preparatory work carried out on the hardware in readiness of the experimental sessions.

3.2 HELIOS spectrometer & collection optics

The HELIOS diagnostic, as configured for the validation experiments, consists of the following fundamental components:

- 18 lines of sight through the plasma;

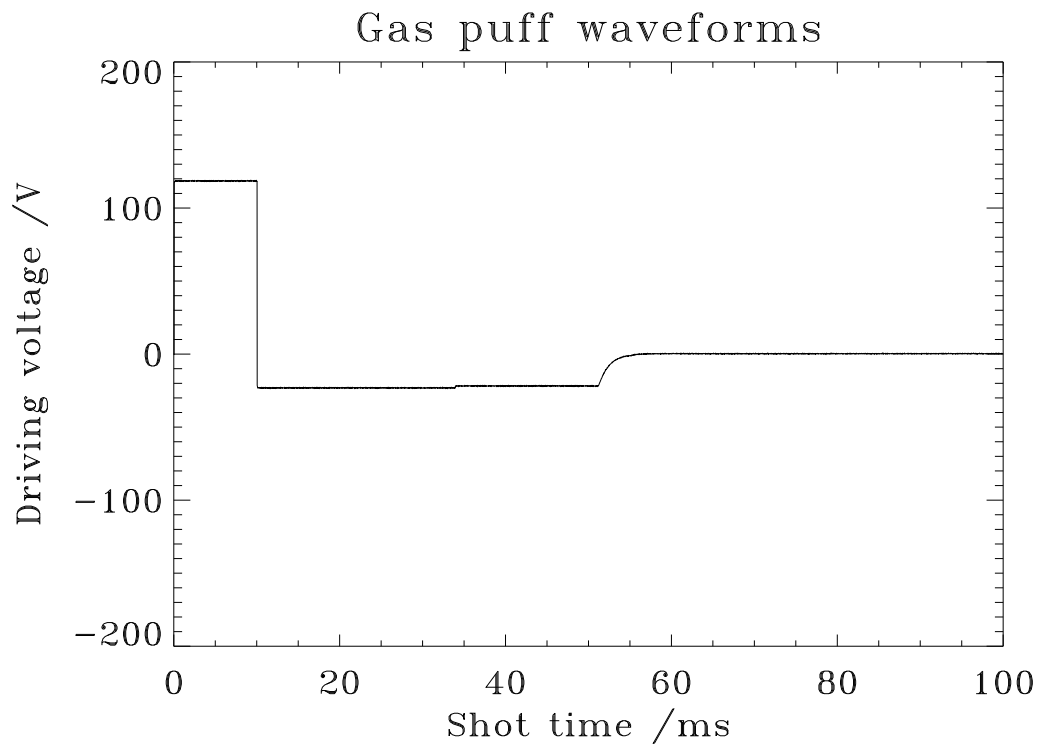


Figure 3.6: The amplified signal used to open and close the piezoelectric valve on the injection system.

Quantity	Value
focal length, f	85 mm
object dist., v	2 m
image width, U	4.9 mm

Table 3.3: Values for the known quantities of the viewing chords.

- an 85 mm objective lens giving a radial coverage of ~ 110 mm;
- 60 cm Czerny–Turner spectrometer with 200 μm slit;
- conjugate pair of lenses to match fibre and spectrometer apertures;
- 300 mm cylindrical lens to correct intrinsic astigmatism;
- a 300 l.mm^{-1} diffraction grating;
- quick-response LCD shutter;
- CCD detector Peltier-cooled to 200 K.

It was necessary for these different components to be set up and calibrated prior to the experiments. The first stage in readying the system was to determine the radial coverage of the tokamak given by the 85 mm objective lens. The quantities known for this calculation are given in table 3.3.

The value of the image width given in table 3.3 is determined by the physical size of the illuminated CCD chip, and the object distance is determined by the focal plane of the lens. The linear magnification of the system, M , can be shown to be:

$$M = \left(\frac{v}{f} - 1 \right)^{-1} \simeq 4.4 \times 10^{-2} \quad (3.20)$$

The magnification can then be used to calculate the object width, which corresponds to the radial range viewed in the tokamak:

$$V = \frac{U}{M} \simeq 110 \text{ mm} \quad (3.21)$$

Therefore, the 85 mm objective lens allows ~ 110 mm of radial coverage within the tokamak.

The 110 mm coverage over 18 viewing chords gives the system a radial resolution of ~ 6 mm. Since the region of particular interest to this work is in the vicinity of the separatrix, the chords were set such that the spectrometer viewed equal distances inboard and outboard of the separatrix for a typical plasma in the campaign. Figure 3.7

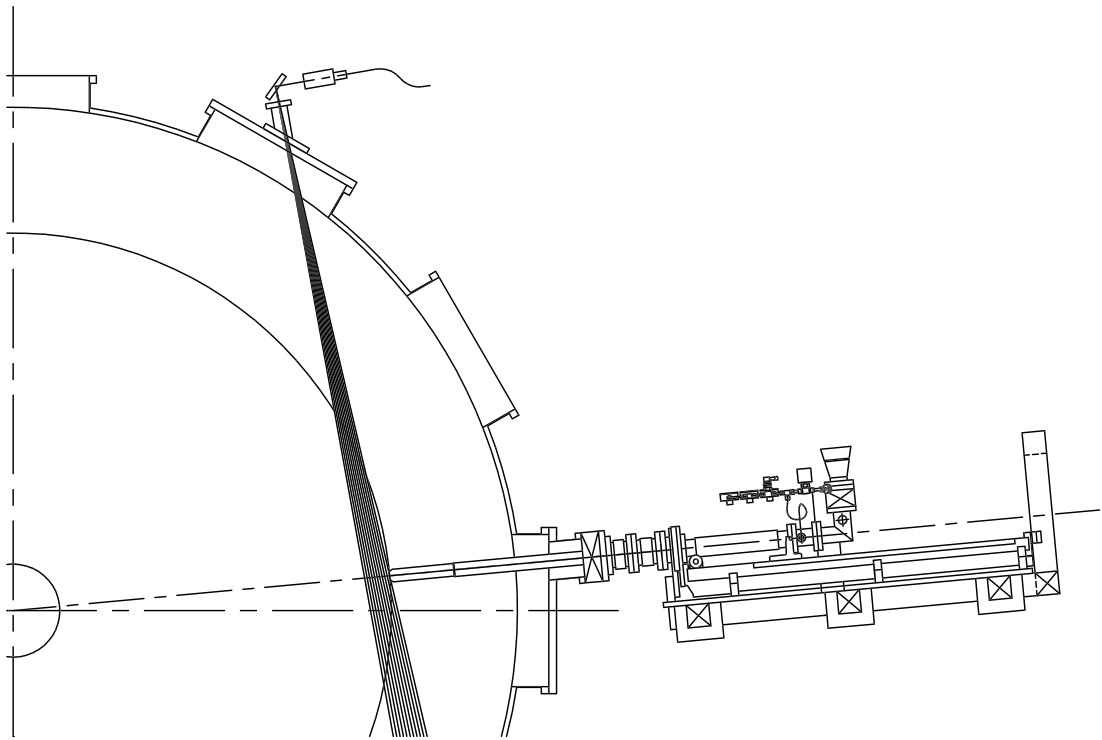


Figure 3.7: Schematic of the HELIOS viewing chords within MAST and their orientation relative to the neutral helium injection nozzle.

shows a schematic of the HELIOS hardware on the device; the steering mirror, viewing chords, and RP-mounted gas injection nozzle are noted.

A bright white-light source was attached to the optical fibre bundle in place of the spectrometer, and shone into the machine. A steering mirror mounted in front of the objective lens allowed the viewing chords to be oriented within the tokamak using two orthogonal Vernier micrometer screws. The RP was adjusted such that the tip of the injection nozzle was at a radial position of 1.4 m. The steering mirror was aligned so the outermost chord was visible as a point of white light on the tip of the nozzle. The micrometer readings are given in table 3.4. This is the configuration shown in figure 3.7. The RP was then re-positioned such that the nozzle was at a radial position of 1.5 m. The horizontal micrometer was then adjusted until the outermost chord was, again, visible on the tip of the nozzle; these micrometer readings are also given in table 3.4. The two sets of micrometer readings allow the conversion of changes in the steering mirror's orientation to radial displacements within the device. It is clear that the fibres were mounted horizontally at the objective lens since no alteration of the vertical position was required.

Micrometer	Initial value	Final value	Difference
Horizontal	1.00 mm	2.17 mm	1.17 mm
Vertical	0.19 mm	0.19 mm	0.00 mm

Table 3.4: The orthogonal micrometer readings for the orientation of the steering mirror. These can be used to convert changes in the mirror’s position to changes in radial position within the machine. The values in the table are average values obtained from three sets of readings.

The outermost viewing chord had to be positioned ~ 6 cm outboard of the required position of the separatrix. One can calculate the relation between changes in the steering mirror’s position, ΔX , and radial position, ΔR :

$$\frac{\Delta X}{\Delta R} = \frac{1.17 \text{ mm}}{100 \text{ mm}} \quad (3.22)$$

from the micrometer settings and positioning of the RP. Therefore, if the separatrix were positioned at $R_{\text{sep}} = 1.35$ m and the nozzle position was $R_{\text{noz}} = 1.5$ m, the change to the horizontal micrometer, δX , needed to change the radial position of the chords, $\delta R = -9$ cm, would be²

$$\delta X = \frac{\Delta X}{\Delta R} \delta R = -1.05 \text{ mm} \quad (3.23)$$

Since the micrometer was set at 1 mm at a radial position of 1.5 m, the required horizontal setting was $X_{\text{set}} = -0.05$ mm.

With the viewing chords aligned within the device and the spectrometer’s entry slit set at the normal width of 200 μm , it was possible to align the optics feeding the spectrometer. The slit width of 200 μm was found to be the optimum value to allow the least intense line at 7283 \AA to be visible without saturating the most intense line at 6678 \AA . The spectrometer was set such that the 6678 \AA was centred on the output display. The helium glow discharge used to clean the device between shots was then used to aid alignment. The optical fibre bundle was attached to a translation stage which allowed the fibres to be manipulated in the two planes perpendicular to the optic axis of the system. The translation stage was used to maximise the 6678 \AA line on the spectrometer’s output display, thus optimising the illumination of the spectrometer’s entry slit and diffraction grating.

The bandwidth of the system could then be measured. The 6678 \AA line was positioned at the lower limit of the spectrometer’s output display. The reading on the spectrometer was 1076.0 \AA . The spectrometer was then reset such that the line was

² $\delta R = -9$ cm because the distance from the separatrix to the nozzle is 15 cm and half the radial extent of the chords is 6 cm.

Reading	Measurement 1 /Å	Measurement 2 /Å	Measurement 3 /Å
Lower limit	1076.0	1075.6	1075.6
Upper limit	1359.4	1358.8	1359.2

Table 3.5: The spectrometer readings used to determine the working bandwidth of the HELIOS spectrometer.

at the upper limit of the spectrometer’s output display, this value was 1359.4 Å. This process was repeated three times to determine an average upper and lower limit on the spectrometer’s reading. The values are given in table 3.5.

It should be noted that the settings on the spectrometer given in table 3.5 correspond to real wavelengths if the dispersion is due to a 1200 l.mm^{-1} diffraction grating. The grating used in this work had 300 l.mm^{-1} and therefore the readings correspond to the real wavelengths multiplied by the dispersion ratio of four. The effective bandwidth, \mathcal{B} , of the system is then $\mathcal{B} = 1132.3 \text{ Å}$. This bandwidth spans a range of wavelengths adequate to measure the three HeI lines required for this study.

During the calibration and configuration described thus far, no problems with the CCD and LCD shutter were immediately obvious; however, this was investigated before carrying out measurements using the spectrometer. Problems are known to have occurred in the past with older LCD shutters. The ideal liquid crystal film for use as the shutter would be opaque in its default state and allow unimpeded transmission when a voltage is applied. Previous shutters have suffered from spotted regions due to light not being absorbed across the entire surface area in its relaxed state. The main advantage in using the LCD shutter, rather than a mechanical alternative, is its rapid response time, which reduces smearing on the CCD during the finite time required to bin the data. The lack of moving parts also means the LCD shutter has a longer lifetime due to less wear-and-tear on the equipment. The uniformity of the shutter’s opacity was determined while calibrating the spectrometer. Without altering the steering mirror the objective lens with the fibres attached was connected to an integrating sphere which provides a known white-light spectrum. The shot sequence was then run manually and the data acquisition software captured an image of the white-light source, as shown in figure 3.8.

A damaged fibre is clearly visible towards the top of the image in figure 3.8. It is also clear that the transmission of the shutter is not uniform since the right-hand-side of the image does not register as much flux as the left-hand-side. The lack of uniformity is not a major concern since it can be taken into account during the absolute calibration of the instrument. It is also evident from figure 3.8 that the viewing lines are not horizontal on the CCD. Since the fibres were mounted horizontally on the

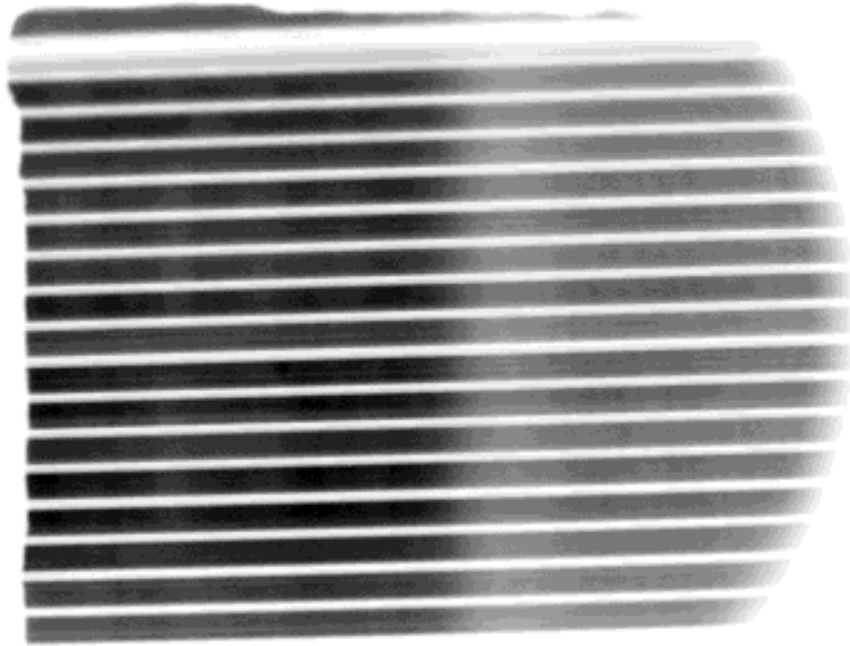


Figure 3.8: The white-light image acquired by the CCD while illuminated by the integrating sphere. The colour map on this image has been reversed, so the black sections show the light carried down each of the optical fibres. One can identify the damaged fibre at the top of the image which does not pass as much light as the other fibres.

integrating sphere and at the entrance to the spectrometer, this means the CCD has rotated slightly in its mounting. The deviation was not considered serious enough to disassemble the CCD and its cooling equipment, so care is taken to deal with the skewness when measuring the photon flux corresponding to each of the emission lines of interest. The CCD was cooled using a solid-state Peltier device coupled to a heat sink to remove thermal distortions to the detected photon flux.

While the system was illuminated using the integrating sphere, the chord positions on the chip were recorded. Figure 3.9 shows a slice through the image in figure 3.8. One can identify the the pixel numbers on the CCD that correspond to the edges of the chords and to the central chord positions, which are important quantities in determining the intensity of the lines of interest. The damaged fibre identified in figure 3.8 is also clearly visible in figure 3.9. The second chord from the right of the figure has a much smaller transmission than the others, and the transmission of the last chord is also somewhat reduced; this suggests damage to the fibre bundle after it had been clad. This could not be rectified without removing and re-fabricating the fibres; therefore, this had to be accepted as a source of systematic uncertainty in the measurements. Although having damaged fibres is not ideal, having them at the edge of the observed region is preferable to having them in a more central location.

With the apparatus in this configuration, illuminating the CCD with the integrating sphere, the spectrometer could be absolutely calibrated. The procedure is not detailed here but can be found in [123]. After completing the absolute calibration of the instrument, the diffraction grating was rotated such that the D_α line, which lies at a wavelength of $\sim 6550 \text{ \AA}$, was slightly below the lower wavelength limit. This removed the need for an intensity filter at the output from the spectrometer. Table 1.3 shows that the D_α line is much more intense than the helium lines of interest, so its removal from the wavelength range of interest was desirable.

Figure 3.10 shows an example of the helium spectrum obtained after the apparatus was configured and calibrated. It can be seen from figure 3.10 that the lines of interest, indicated on the plot, are distinct from the background and lie within the calculated bandwidth of the HELIOS spectrometer.

3.3 Plasma configuration

A plasma configuration was chosen that gave a long period of L-mode followed by a sustained H-mode since the validation experiments were related to both these confinement regimes. Figure 3.11 shows the D_α emission and the line-integrated electron density for the target shot #12158. It can be seen that there is a long L-mode phase to

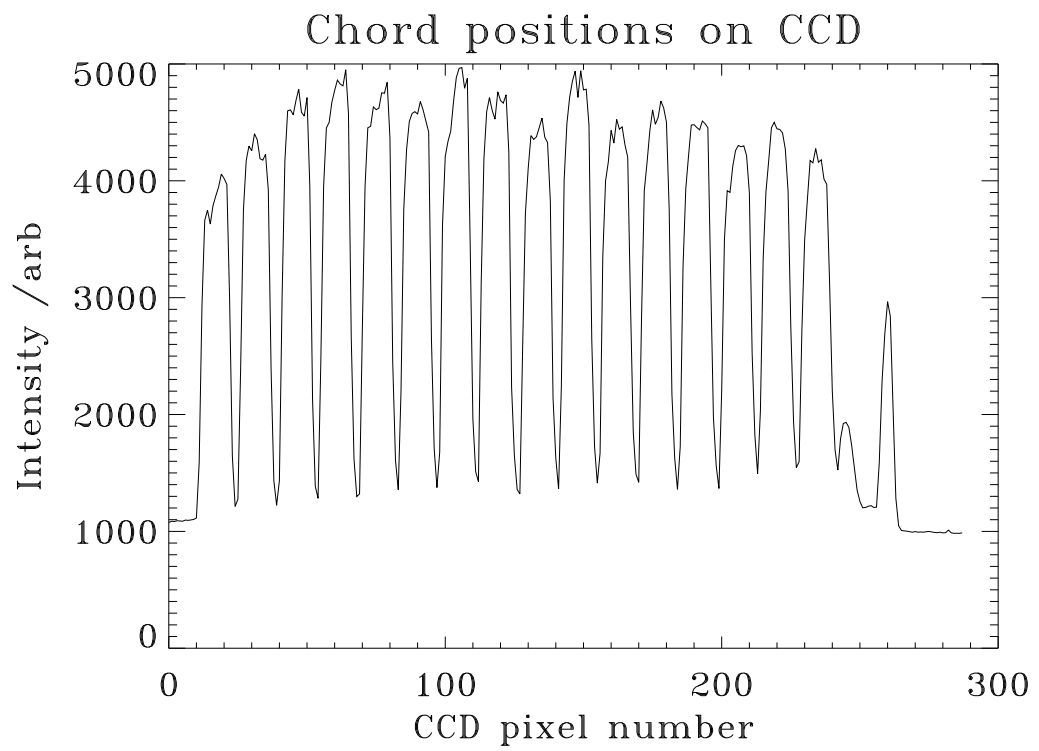


Figure 3.9: The position of the chords to the CCD. The edges of the chords are required when calculating the intensity of the lines of interest.

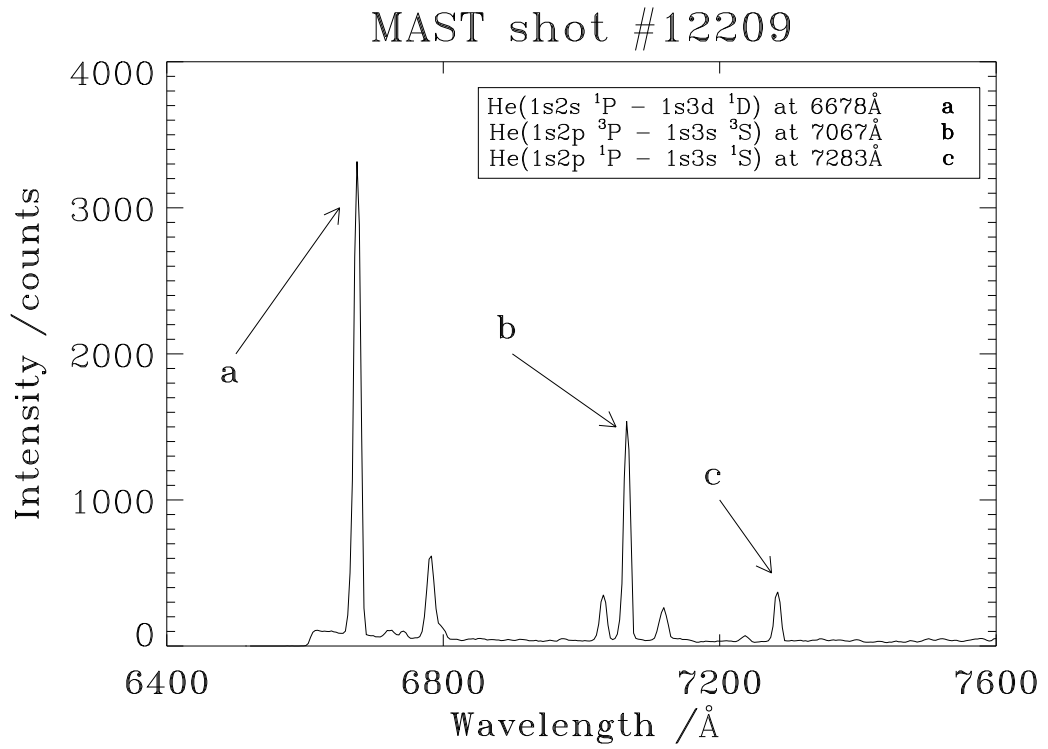


Figure 3.10: The helium spectrum taken after the configuration and calibration of the apparatus had been completed. One can see that the HeI lines of interest are distinguishable from the background and lie within the calculated bandwidth of the instrument.

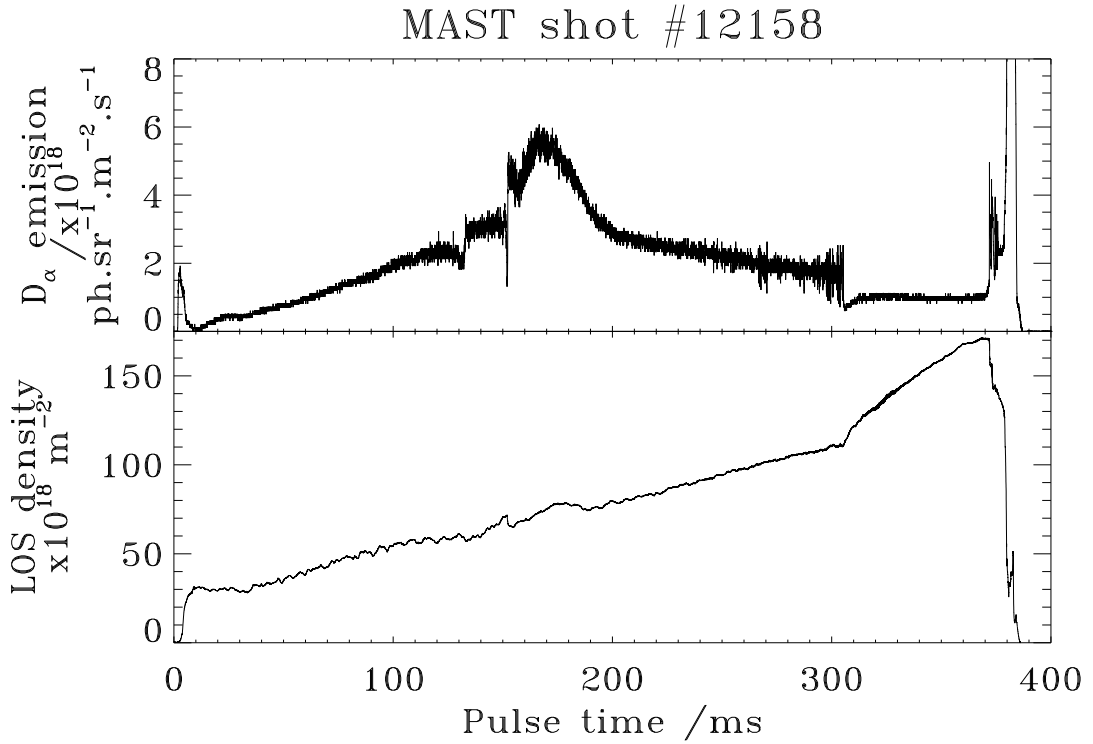


Figure 3.11: The upper plot shows the D_α emission and the lower plot the line-integrated electron density for MAST shot #12158. It can be seen that this shot has a long L-mode period to ~ 300 ms followed by an H-mode phase which lasts until ~ 370 ms characterised by the dip in D_α emission and sharper rise in density.

~ 300 ms followed by an H-mode phase persisting for ~ 70 ms.

Using this shot as a template, both L-mode and H-mode plasmas could be studied simply by altering the diagnostics' timing waveforms. The efficiency of this choice of shot saved time by removing the need to change and test plasma configuration between shots when moving between L- and H-mode measurements.

Taking the target shot into account, it was decided that the separatrix should be positioned at $R_{\text{sep}} = (145 \pm 1)$ cm, as it was for shot #12158. Figure 3.12 shows the plasma radius for the target shot #12158 and one of the first campaign shots, #12204; it can be seen that the plasma radius of the desired target shot was well reproduced. Both plasmas had a line integrated density of $\sim 10^{20} \text{ m}^{-2}$. The solid lines in figure 3.12 shows the magnetic reconstruction of the plasma edge produced by EFIT (equilibrium fitting). EFIT translates measurements from the magnetic diagnostics into useful information, such as plasma geometry, stored energy, and current profiles, by solving the Grad-Shafranov tokamak equilibrium equation[5, 44]:

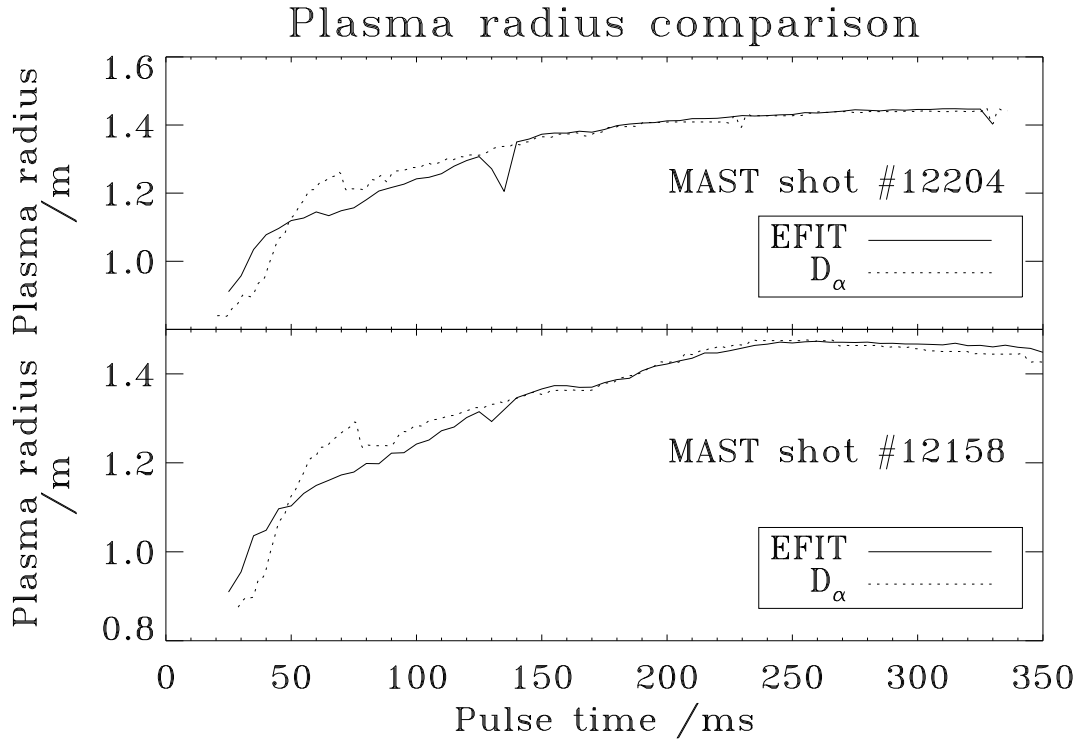


Figure 3.12: The upper plot shows the plasma radius for an early relevant campaign shot, #12204, and the lower shows the same plot for the target shot, #12158. The plasma radius as given by EFIT and D_α is shown.

$$R \frac{dp}{d\psi} + \frac{\mu_0}{R} f \frac{df}{d\psi} = j_\phi \quad (3.24)$$

where R is the major radius, p the pressure, ψ the poloidal flux, j_ϕ the toroidal current density, and f a flux function defined as:

$$f(\psi) = \frac{RB_\phi}{\mu_0} \quad (3.25)$$

The details of the EFIT method can be found in [124]. The EFIT reconstruction of the flux surfaces of the target shot #12158 are shown in figure 3.13 as an example of EFIT's general use as a post-pulse plasma analysis tool.

A list of deliverables required from the experimental time while measurements were being made with the HELIOS spectrometer were determined. These were:

- set $R_{\text{sep}} = (145 \pm 1)$ cm;
- adjust helium gas level for good measurement from $R_{\text{noz}} = 150$ cm;

MAST shot #12158, $t=130\text{ms}$

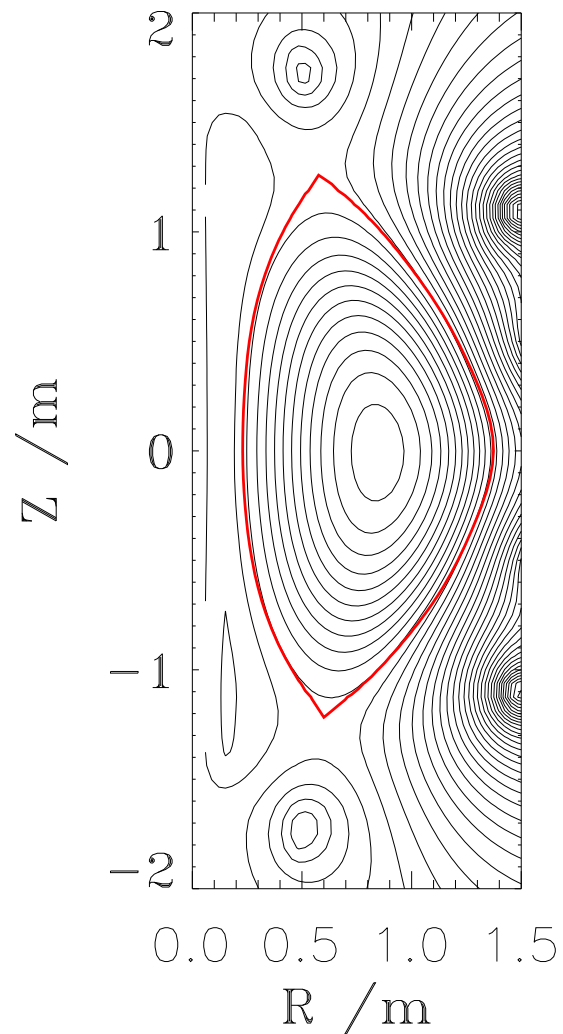


Figure 3.13: EFIT reconstruction of the MAST flux surfaces during the target shot #12158. The separatrix is indicated in red. The large Shafranov shift associated with spherical tokamaks is clearly evident; the flux surfaces are more widely spaced on the inboard side compared to the outboard.

- TS measurements in L-mode phase;
- change timing on TS, measurements in H-mode phase;
- change nozzle position to $R_{\text{noz}} = 155$ cm, TS measurements in H-mode phase;
- change timing on TS, measurements in L-mode phase;
- measure SOL profiles with RP in L-mode phase;
- measure SOL profiles with RP in H-mode phase.

These measurements would allow comprehensive data for comparison with theoretical modelling, and the inclusion of RP measurements of the SOL would provide detailed N_e and T_e which could be merged with TS measurements of the core plasma [125, 126]. This would give an accurate picture of the plasma conditions in the vicinity of the neutral helium nozzle and along the helium's attenuation path in the device. With accurate data for the path taken by the helium in the plasma, one can compare the spectral emission observed, an example of which is shown in figure 3.14, with that anticipated by the theoretical emission model. This comparison is carried out in chapter 4.

Since the ruby TS system takes only one set of spatial measurements per pulse, it can not be used in the temporal modelling to compare with the HELIOS measurements; however, the time resolved Nd:YAG system allows a temporal comparison. The issue of temporal modelling will be returned to in section 4.7.

3.4 Summary of the MAST pulses

To plan a detailed, structured scientific period for the second experimental phase one had to determine how close the injection nozzle could come to the plasma edge before interaction took place. Investigating the interaction between the plasma and the nozzle was the main outcome of the initial session. Strong interaction was observed during MAST shot #10502, as shown in figure 3.15.

From figures 3.15(a) and 3.15(b) one can see that the plasma reduces in size dramatically at ~ 250 ms and is preceded and accompanied by a large increase in emitted power. One can also see that the D_α emission, shown in figure 3.15(c), spikes at this point; this indicates a large energy/particle loss to the edge and is verified by the decrease in plasma density shown in figure 3.15(d). A comparison of the D_α and soft

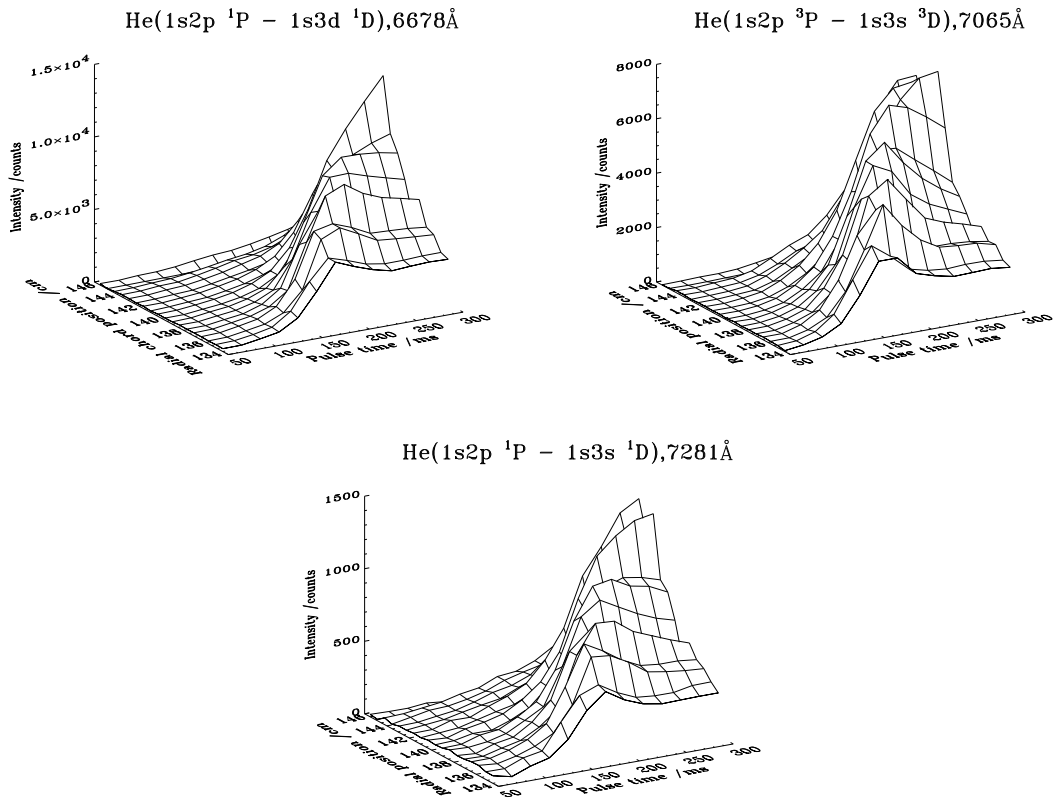


Figure 3.14: The spatial and temporal evolution of the emission lines of interest as measured by the HELIOS spectrometer.

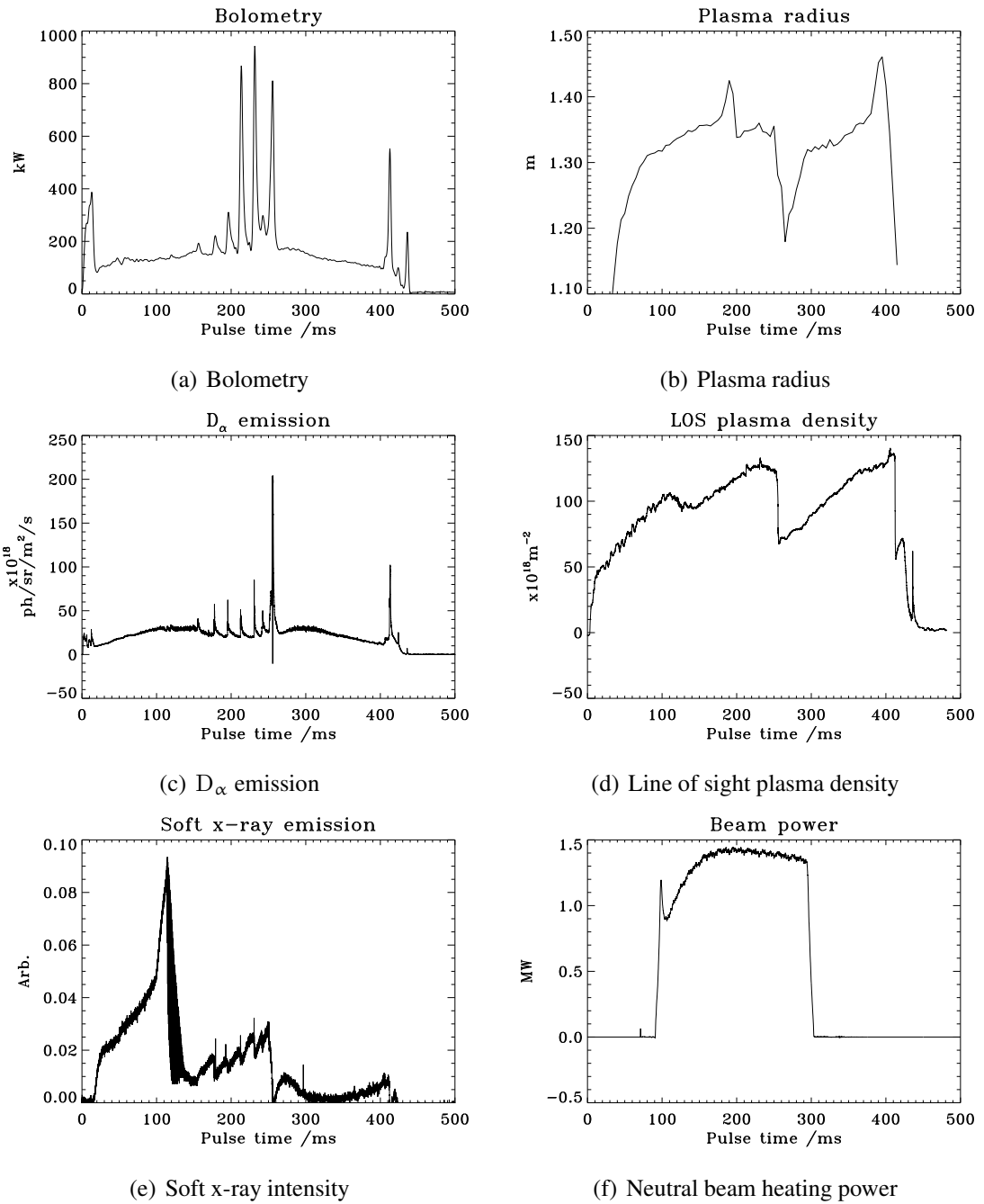


Figure 3.15: The interaction between the plasma and the neutral helium injection nozzle during MAST shot #10502 during the first experimental period. See text for details.

x-ray emission shows that there is a strong negative correlation between these two signals. A steady decrease in the D_α emission features shown in figure 3.15(c) is accompanied by a steady increase in the soft x-ray emission features shown in figure 3.15(e). Figure 3.15(f) shows the neutral beam heating power throughout the pulse; in the region of particular interest the heating power is relatively constant, which is ideal for these studies. It is clear from figure 3.15 that a sawtooth caused the plasma to impact on the HELIOS RP causing a large density loss, corresponding energy loss, and a possible risk to the helium injection hardware mounted on the RP. This was a useful outcome as it allowed the minimum distance between nozzle and separatrix to be judged for the types of plasmas used in the validation experiments. Due to this result, the radial position of the plasma separatrix was decreased by 3 cm, moving it away from the nozzle. In a sawtooth, a slow rise in plasma temperature is followed by a rapid crash, triggered by a plasma instability[127]. In the crash phase, hot plasma from the centre is thrown out into the colder outer plasma regions. This process can be used to remove helium ash and other impurities from the plasma, however it can be a danger to apparatus at the edge. The sawteeth, therefore, have to be tailored to the specific requirements of a particular experiment[128, 129, 130].

With the position of the plasma separatrix altered by 3 cm due to the useful outcome of MAST shot #10502, the last shot of the first period provided a good base from which to move on with the structured scientific phase of the validation experiments. Figure 3.16 shows similar plots to those in figure 3.15, but there are some important differences.

One can see that figure 3.16(a) does not contain the multiple peaks in power output evident in figure 3.15(a); nor does the D_α emission shown in figure 3.16(c) exhibit the spike found in figure 3.15(c), meaning there has not been a large loss of particles to the edge. Sustained sawtooth structure is evident in figure 3.16(c), with the inverted features observed in figure 3.16(e). The line plasma density of $1.5 \times 10^{20} \text{ m}^{-2}$ shown in figure 3.16(d) is close to the density sought for this work, and the stable beam power in figure 3.16(f) is very suitable, driving sawteeth when it reaches ~ 1.3 MW. If one looks closely at the D_α emission, soft x-ray emission and the plasma density in the vicinity of the sawteeth, one can see that the plasma goes into a very brief H-mode after the sawtooth, but it cannot be sustained due to the plasma's proximity to the central column. A close-up view of a sawtooth and brief H-mode from MAST shot #10504 is shown in figure 3.17. Figure 3.16(b) shows a decrease in plasma radius at ~ 215 ms, but there is no density loss shown in figure 3.16(d); this contrasts the observations of MAST shot #10502, where the change in plasma radius is accompanied by a clear density drop. The plasma equilibrium reconstruction by EFIT produced a value for the

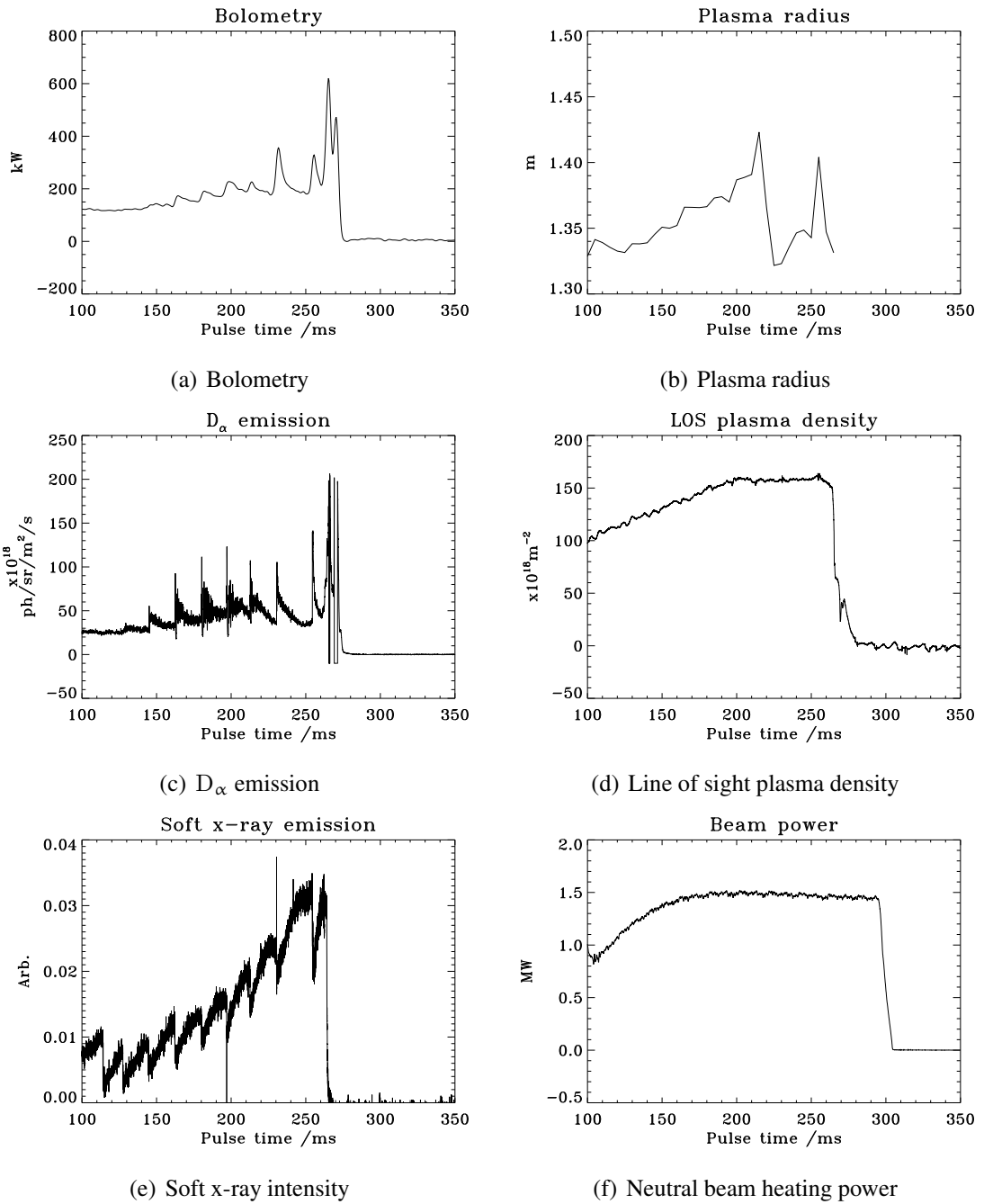


Figure 3.16: Measurements taken during MAST shot #10504 after optimisation of plasma parameters. See text for details.

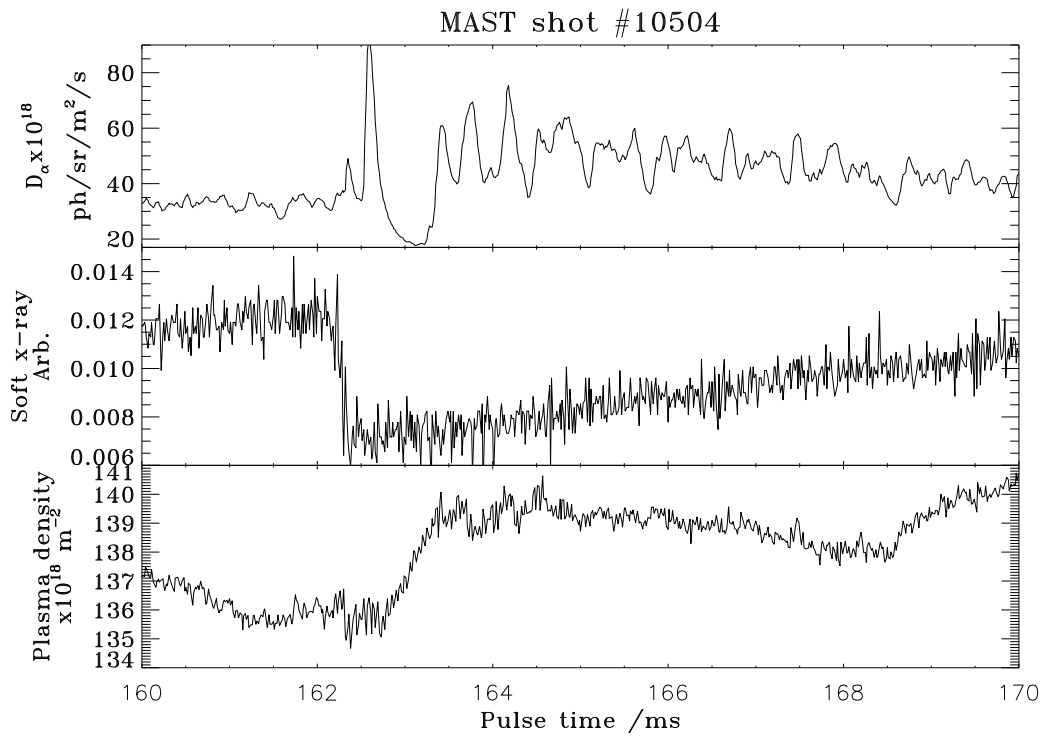
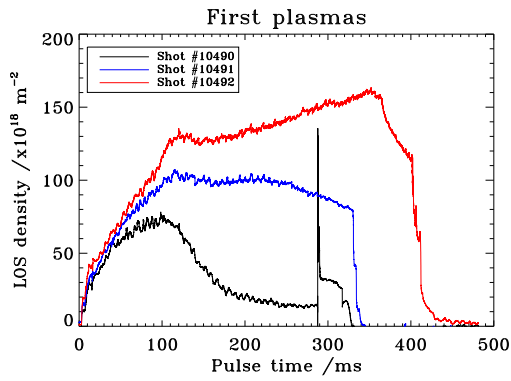


Figure 3.17: A close-up view of a sawtooth observed during MAST shot #10504. One can see the decrease in D_α emission correlated with an increase in plasma density. The H-mode is not sustained due to the plasma's proximity to the central column.

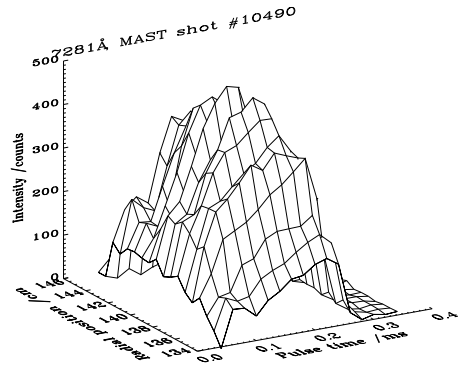
position of the inboard plasma edge which suggested the plasma moved towards the central column, explaining the change in plasma radius without a corresponding drop in density. This movement of the plasma is consistent with the testing of plasma radial control undertaken during this period.

This preliminary experimental period was encouraging and there were several outcomes which allowed a confident thrust at the structured scientific program for the second experimental phase. The important issues raised above were coupled with other observations made during the session. Data was taken by the HELIOS diagnostic throughout the commissioning period. From the first plasma produced, in MAST shot #10490, improvements were made to the setup, and these improvements were accompanied by clear HELIOS measurements. Figure 3.18(a) shows the LOS densities for the first three plasmas produced in the session. It can be seen that the line integrated density increases to a value of approximately $1.5 \times 10^{20} \text{ m}^{-2}$, appropriate for this work.

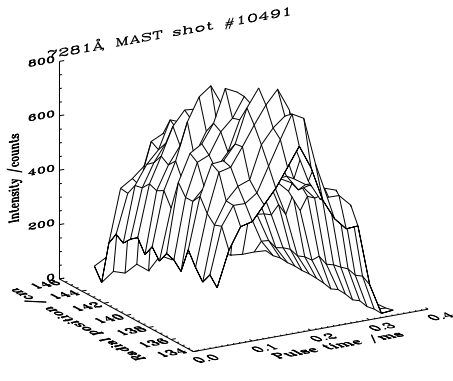
The emission detected by HELIOS shown in figure 3.18(b) is around 60% of that shown in figures 3.18(c) and 3.18(d). This is as expected since, from figure 3.18(a),



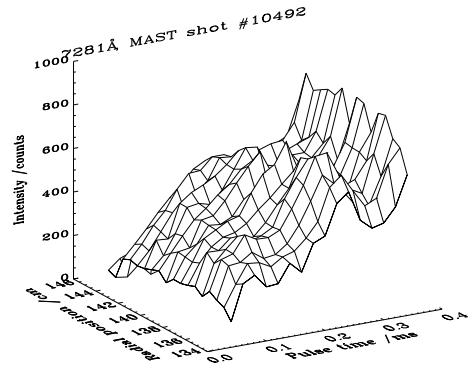
(a) First plasma densities



(b) 7281 Å emission for MAST shot #10490



(c) 7281 Å emission for MAST shot #10491



(d) 7281 Å emission for MAST shot #10492

Figure 3.18: The LOS electron density for the first three plasmas produced during the first experimental session and the intensities of the weakest emission line as measured by the HELIOS diagnostic. The configuration is improved to produce the density and duration required.

one can see that the plasma density in shot #10490 reaches its steady value in a time similar to the later shots, but the plasma is under-dense by a factor of 40 – 50% due to the inboard fuelling injector not delivering enough deuterium to the plasma.

The second experimental session provided many results within the structured program discussed in section 3.3. For MAST shot #12202, the HELIOS diagnostic was set to begin taking results 50 ms after the pulse start time, and take 16 frames at 20 ms intervals. The plasma in shot #12202 impacted on the helium injection nozzle and caused the plasma to disrupt at ~ 260 ms. HELIOS continued taking data through this period and acquired data from a hot plasma before the plasma–nozzle interaction and from a plasma with large edge emission during the interaction. Figure 3.19 shows the radial D_α profile for shot #12202. The radial position of the outboard plasma edge is visible as the peaked curve in the figure. One can see at the outboard edge of the plasma there is a large increase in D_α emission after 200 – 300 ms; this is emission due to the plasma–nozzle interaction. The large D_α emission at small radial position is the inboard plasma edge, which is relatively constant throughout the pulse.

Figure 3.20 shows a HELIOS spectrum taken 150 ms into the pulse and another at 230 ms. One can see the HeI lines clearly on the upper plot, but the lower plot shows a large continuum which obscures the emission lines of interest. The small impurity peaks visible on the upper plot are greatly intensified in the lower plot during interaction between in the plasma and the injection nozzle.

MAST shot #12241 provided a good L-mode pulse to fit in the structured plan. The neutral beam injectors provided ~ 1.5 MW during the shot and the ruby TS system was fired at 260 ms. HELIOS took good readings throughout the shot and H-mode was achieved after ~ 330 ms, as per the plan and target shot specifications. This shot provided one of the most suitable, stable L-mode plasmas for further study and analysis. The first sawtooth impacted on the nozzle causing the plasma to disrupt; however this occurred after the main period of interest in this shot. For maximum efficiency two similar plasmas were required, both with long L-mode periods followed by extended H-mode. Figure 3.21 shows a comparison of MAST shot #12241 and #12242; one can see that the plasma conditions were well replicated.

The ruby TS was set to fire at 350 ms for MAST shot #12242, in the region of decreased D_α emission indicating H-mode, as shown in figure 3.21(a), and HELIOS was set to take data from 100 ms. Shot #12242 goes into H-mode slightly later than #12241, but it is before the TS fires.

With good L- and H-mode shots obtained for analysis, the next point in the plan was to capture Langmuir RP data in the SOL to give comprehensive N_e and T_e data over the region of interest in the plasma. The results of the Langmuir probe mea-

D_α camera

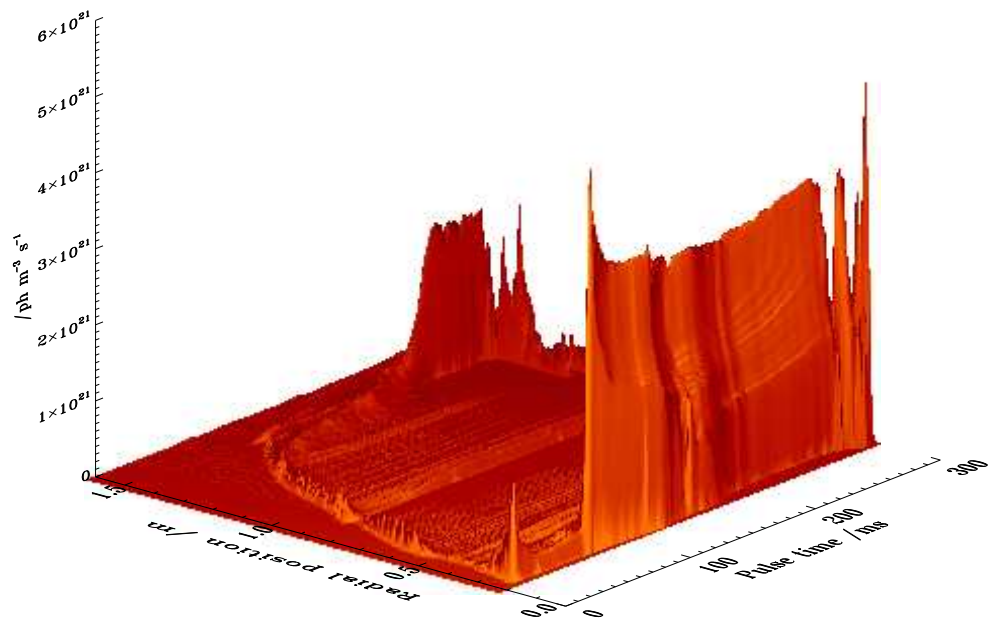


Figure 3.19: The radial D_α profile during MAST shot #12202. One can clearly see the increase in emission at the outboard edge after 200 – 300 ms due to the plasma–nozzle interaction. The position of the outboard plasma edge is visible as a function of time as the peaked curve on the plot. The plasma–nozzle interaction subsequently results in a plasma disruption.

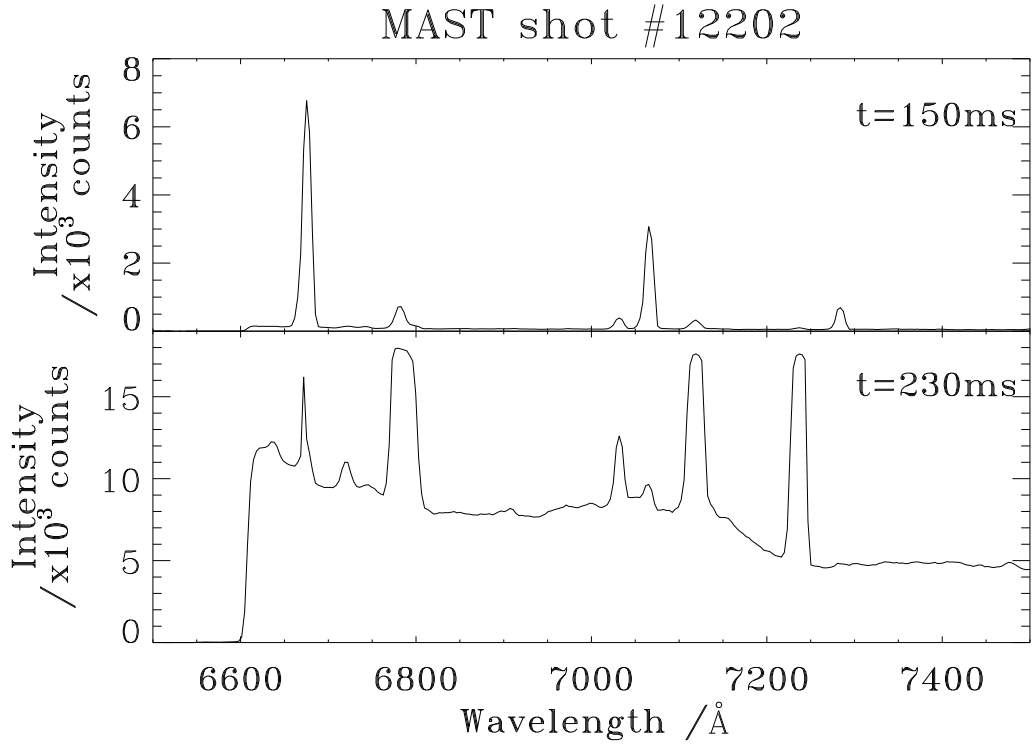
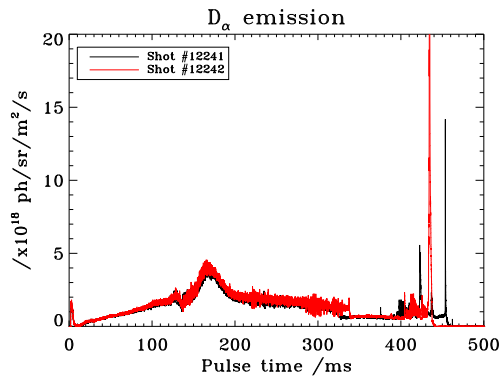
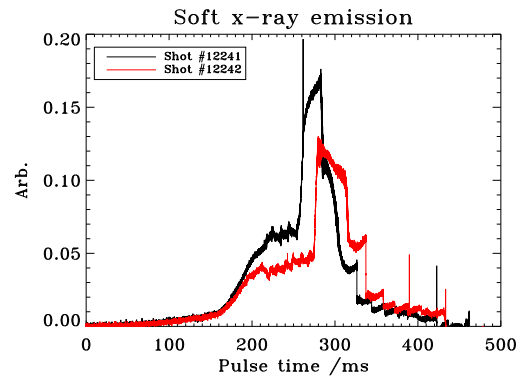


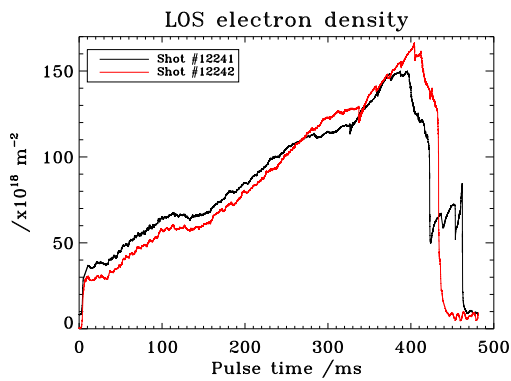
Figure 3.20: Spectra captured by the HELIOS spectrometer during MAST shot #12202. The upper plot shows the spectrum captured 150 ms into the pulse and the lower plot shows the spectrum at 230 ms. The HeI emission lines are clearly visible in the upper plot, but are obscured in the lower plot by the intense continuum radiation emitted during the interaction between the plasma and the helium injection nozzle. The impurity lines, due to CII at 6784 Å, 7116 Å, 7236 Å and CIII at 7037 Å, barely visible in the upper plot, are intensified in the lower plot[51].



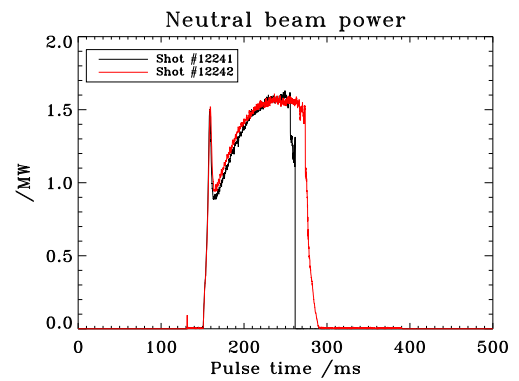
(a) D_α emission



(b) Soft x-ray emission



(c) LOS electron density



(d) Neutral beam power

Figure 3.21: Comparison of the plasmas of MAST shot #12241 and #12242. One can see that the plasma conditions are replicated well from one shot to the next.

measurements were limited due to strong interactions between the probe and the plasma causing disruptions, but nonetheless provide a useful N_e and T_e baseline in the SOL for augmentation with the TS measurements. Useful Langmuir probe data was taken during L-mode, but was not possible during H-mode due to disruptions caused by severe plasma–probe interaction.

So far this section has presented and discussed the measured results obtained during the experimental sessions. With this in place, it is timely to discuss the analysis of the HELIOS spectrometer’s measurements which can allow diagnostic deductions of plasma conditions to be made. L- and H-mode plasmas will be used to compare the HELIOS results with the other diagnostics; useful plasmas, and their conditions, are:

- L-mode: MAST shot #12241
 - NBI \sim 1.5 MW;
 - ruby TS fired at 260 ms;
 - good HELIOS measurements for full period;
 - entered H-mode \sim 70 ms after period of interest.

- H-mode: MAST shot #12242
 - NBI \sim 1.5 MW;
 - ruby TS fired at 350 ms;
 - HELIOS started taking data at 100 ms, good measurements throughout;
 - entered H-mode \sim 10 ms prior to period of interest.

- RP data during L-mode: MAST shot #12245
 - NBI \sim 1.5 MW;
 - ruby TS fired at 260 ms;
 - HELIOS started taking data at 100 ms, good measurements throughout;
 - good RP movement through the plasma, data for $R \in [1.46, 1.51]$ m.

Taking a HELIOS spectrum, the lines of diagnostic importance, as re-stated in table 3.1, are identified on the CCD. The pixel numbers corresponding to the edges and peaks of the lines are used to identify the lines. From figure 3.8 one can see that the chords are skewed slightly on the chip, therefore the edges and peaks of the lines are determined for each chord at each time-slice.

The number of counts detected by the spectrometer between the upper and lower limits of the lines is determined and a background count is subtracted. These counts are then divided by the calibration factor for the particular viewing chord to give the number of photons corresponding to the counts registered. These adjusted counts are used to calculate the line ratios at the particular time-slice for the viewing chords.

The predictive modelling of the HeI emission discussed in chapter 4 details the plasma model necessary to understand fully the emission processes taking place; however, at this stage, a simple look-up of the line intensity ratios can give a crude indication of the diagnostic sensitivity of the line ratios. It should be noted that there are certain assumptions that must be made to apply a simple look-up of the ratios rather than considering a full plasma model. One must assume that the emission detected by the spectrometer is not affected by the viewing geometry and that the ground to metastable relative populations are in local equilibrium. These are two large assumptions considering the collimation of the nozzle is not known. With no knowledge of the collimation, the spatial distribution of the helium within the viewing chords is not known. Also, the large temperature and density gradients at the edge of the confined plasma can lead to regions of non-equilibrium in the helium metastable populations where they are of most interest to this study. These issues will be discussed in more detail in chapter 4.

The line ratios of interest were discussed in chapter 2: the ratio of the two singlet transitions in table 3.1 being an electron density diagnostic, and the singlet–triplet ratio being an electron temperature diagnostic.

The simple look-up of the line ratios is accomplished by taking a contour of the line ratios as functions of electron temperature and density, splining the line ratios to find their position in parameter space, deducing the value of temperature and density that would result in the ratio pair. This is the method used with some success on TEXTOR[36], COMPASS-D[40] and Alcator C-Mod³[131], but has generally not provided such good results on MAST[132] or NSTX⁴. A new prototype supersonic gas injection system on NSTX is expected to improve measurements significantly, due to improved collimation and penetration[133].

Figure 3.22 shows the TS data for the L-mode MAST shot #12241 and the HELIOS values obtained using the simple look-up method..

Taking the N_e measurements in figure 3.22 as an example, the deviation of the HELIOS calculated values from TS at the extremes of the range can be explained. The discrepancy at $R \gtrsim 146$ cm could be due to the low density of the plasma resulting

³Massachusetts Institute of Technology, USA.

⁴National Spherical Tokamak eXperiment, Princeton Plasma Physics Laboratory, USA.

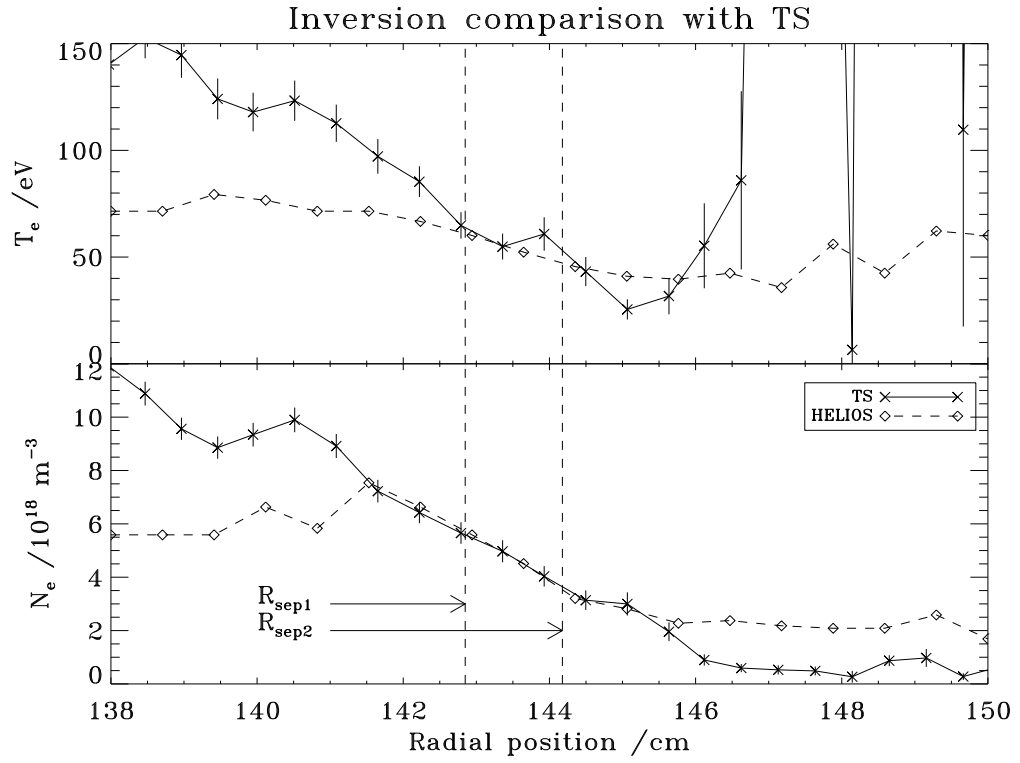


Figure 3.22: The electron temperature and density for the L-mode period of MAST shot #12241. The HELIOS results are obtained using a simple look-up of the emission line ratios calculated from the measured HeI spectrum. Two values of the separatrix are marked on the plots: R_{sep1} is the value given by the D_α diagnostic, and R_{sep2} is given by EFIT. The disparity is due to plasma interaction with the nozzle but is within the acceptable limit of $\pm \sim 1$ cm. The large separation between the separatrix plasma boundary and the magnetic pickup coils can result in relatively large errors of as much as a few centimetres in the separatrix position from the EFIT magnetics reconstructions[134].

One can see that there is very good agreement in N_e in the vicinity of the separatrix, with less agreement observed in T_e measurements. The large uncertainty bars on the T_e values of TS should be noted.

in little HeI emission in this region, or be caused by wrap-around emission observed by the spectrometer. The divergence of HELIOS from TS at $R \lesssim 141$ cm is because the neutral helium has been mostly ionised in this region, again, resulting in a low HeI signal and poor diagnosis.

The relatively poor agreement of HELIOS T_e in figure 3.22 for $R \leq 143$ cm may be due to the viewing geometry. As stated above, this simple look-up of the emission line ratios does not contain a plasma model and therefore does not take geometry into account. In this case, the innermost viewing chords have lines of sight through low-density low-temperature SOL plasma before reaching the confined plasma. The collimation of the nozzle could therefore lead to emission from colder plasma being detected by these inner viewing chords and masking the hot emission from the confined plasma. This is an issue that will be dealt with in more detail in chapter 4.

3.5 Utilising resultant HeII emission

The primary measurements made during this work were the emission lines due to HeI; however, once the neutral helium has ionised, the H-like ion is influenced by the electromagnetic forces which permeate the plasma. It is therefore worth mentioning an additional diagnostic that can be made “for free” using the HELIOS system’s neutral gas injection system. The smeared HeII emission can be observed using the CELESTE⁵ Doppler spectrometer[135]. CELESTE shares the same optics as HELIOS and has higher spectral, spatial and temporal resolution. The Doppler shift of the HeII spectrum lines allows the speed of the H-like ions, the plasma rotation, to be measured. The thermal broadening of the spectral lines also allows the ions’ temperature to be measured. The visible spectral region around He^{+1} ($n = 4 \rightarrow 3$) at ~ 4685 Å is generally used by CELESTE for plasma rotation measurements.

The combination of using HELIOS for edge N_e and T_e measurements and CELESTE for Doppler flow velocity measurements was carried over to MAST from the COMPASS-D tokamak[40] where it was used for detailed studies of edge transport barrier formation and their temporal evolution[136]. The pairing of HELIOS and CELESTE is a good example of the diagnostic synergy highly sought after for implementation on ITER.

3.6 Conclusions

This chapter has summarised the work carried out in measuring the HeI emission using the HELIOS multi-chord spectroscopic setup. There were several main parts to this

⁵Charge Exchange Light Emission Spectroscopy for Temperature Evaluation.

experimental work, which led to measurement of both L- and H-mode plasmas for comparison with the theoretical model which will be outlined in chapter 4, namely:

- work carried out in tailoring the neutral helium puff;
- configuration of the hardware to optimise the measurements;
- alignment of the collection optics to complement the target plasmas;
- configuration of plasma to obtain the measurements required in minimum number of shots.

The results obtained from the experimental work discussed in this section provide a base on which comparisons with theory and modelling can be made. The aims stated at the beginning of this chapter required measurements in different plasma conditions, both L- and H-mode plasmas, and Langmuir probe measurements of N_e and T_e profiles in the SOL. Results were taken for a variety of plasmas, and were sufficient to allow an examination of the physical processes resulting in emission in the vicinity of the separatrix of a magnetically confined fusion plasma.

The next chapter of the thesis will outline the theoretical work carried out to model the HeI emission resulting from the thermal gas puff employed by the HELIOS diagnostic, underpinned by the fundamental data and processing discussed in chapter 2 and evaluated by the experimental work summarised in this chapter.

Chapter 4

Prediction and deduction using an emission model for MAST

The GCR modelling of neutral helium carried out as part of this work, sought to answer questions surrounding the experimental setup and diagnostic utilisation of a thermal helium gas puff on a magnetically confined fusion plasma. The main issues dealt with in this chapter are:

- representing the SOL in predictive modelling;
- effect of non-equilibrium metastable populations on predicted emission;
- determining the collimation of the injection nozzle from measured spectral emission;
- the problem of the actual profiles of line emission along the lines-of-sight for localised deductions where there is a spatially extended gas puff;
- determining temperature and density radial profiles from the spectral line ratios with non-equilibrium metastable population fractions.

This chapter will begin with a computational overview in section 4.1, highlighting the main computer codes used in this work, but with emphasis on the underlying physics. Sections 4.2 and 4.3 will continue by covering the fitting and processing of TS T_e and N_e measurements necessary for modelling the theoretical emission from the plasma. The fitted profiles are then used to investigate the localisation of the emission expected from the HELIOS spectrometer using a spatially resolved emission model outlined in sections 4.4 and 4.5. Modelling the temporal behaviour of the neutral helium in the presence of an ELM is described in section 4.7, with the limits on the modelling detailed in section 4.8. Combining many of the modelling techniques described in this

chapter, section 4.9 discusses deduction of predicted radial N_e and T_e profiles based on the HELIOS spectral line ratio measurements.

4.1 Computational overview

The predictive modelling software takes N_e and T_e diagnostic data from TS, and possibly other available sources such as Langmuir probe measurements, and calculates the metastable populations from the injection nozzle to a specified distance into the plasma. The neutral helium puff is discretised into a number of beamlets, which have an angular distribution around the radial vector determined by the injector collimation. The time taken for a calculation varies linearly with the number of beamlets specified; approximately thirty beamlets is found to be adequate to describe the system, and will be used here unless otherwise stated.

Due to the relative timescales of the HELIOS spectrometer's measurements and the helium's transit time through the plasma, the system can be considered independent of time; that is, the individual time slices can be treated separately, with no consideration of history. Therefore, the illustrative results in this chapter are generally for a single time slice of the pulse. The time used for display of results is that from the ruby TS firing time, unless otherwise stated.

The computational model is built on a number of parameters, a few numerical which are not physical in nature, and some physical which affect the calculation. The numerical parameters are:

- number of beamlets;
- number of points in the quadrature;
- distance into the plasma before stopping quadrature.

Figure 4.1 shows a schematic of the emission modelling.

The structure shown in figure 4.1 uses the TS and RP data obtained for a particular MAST shot, and predicts the HeI emission due to the HELIOS injection nozzle. This emission model is useful for investigating features of the prediction which are not easily measured experimentally; namely, spatially non-equilibrium emission.

The initial settings shown in figure 4.1 include the numerical parameters, the radial position of the injection nozzle and the atomic data to be used. With these settings, the code then accesses the ADAS atomic data, the MAST non-spectroscopic experimental data and the HELIOS calibration data necessary to carry out the spatially resolved

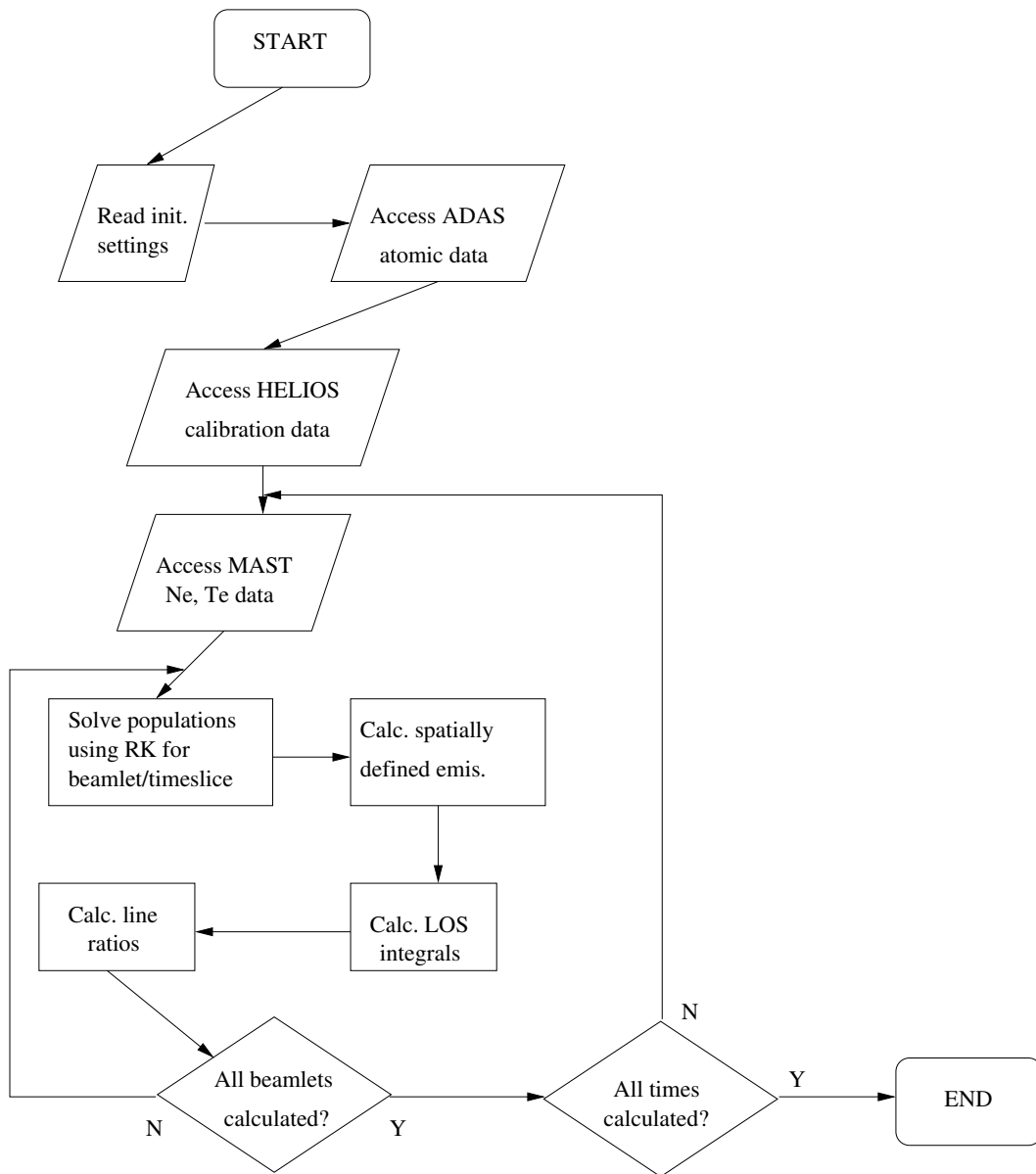
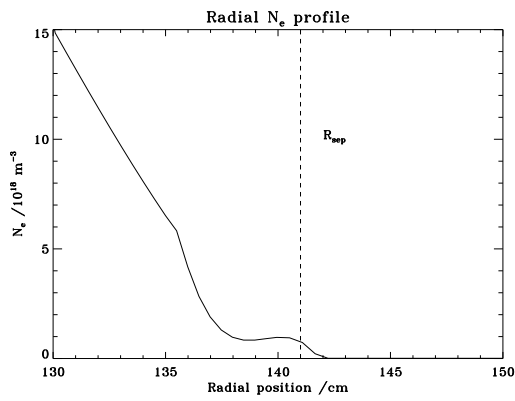
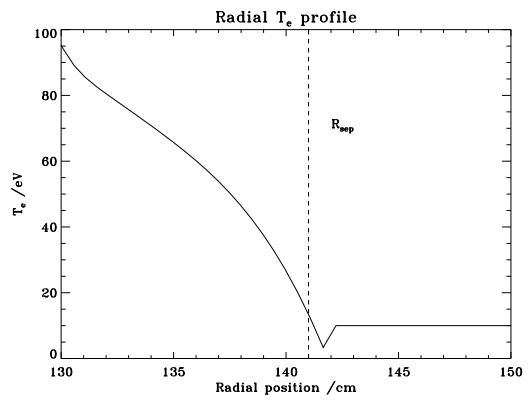


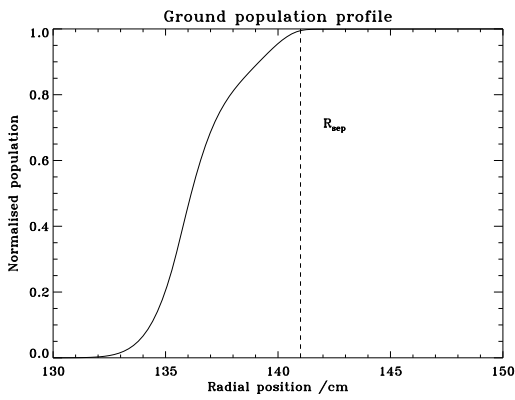
Figure 4.1: A schematic of the main body of the emission model. This will be the basis for the modelling work in this chapter and will be built upon and modified in subsequent sections to deliver the theoretically anticipated emission.



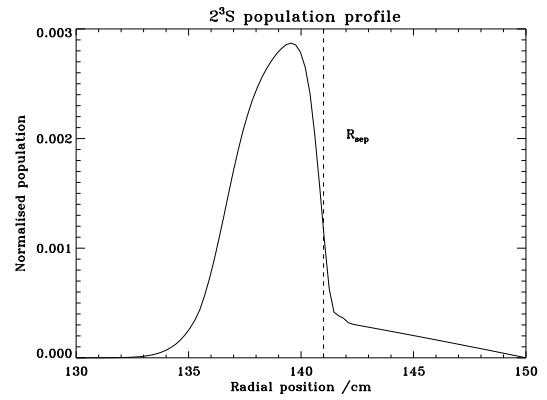
(a) Radial N_e profile



(b) Radial T_e profile



(c) Radial $\text{He}(1s^2 \ ^1S)$ population



(d) Radial $\text{He}(1s2s \ ^3S)$ population

Figure 4.2: 4.2(c) and 4.2(d) show the radial variation of the helium metastables given the density and temperature profiles shown in 4.2(a) and 4.2(b) using the procedure prescribed in figure 4.1.

metastable population attenuation calculation. Figure 4.2 shows the radial evolution of the metastable populations for given TS N_e and T_e profiles.

From the radial profiles shown in figures 4.2(a) and 4.2(b), it is evident that the N_e and T_e data taken from the ruby TS diagnostic are of low quality at the plasma edge. The uncertainties arising from the TS data mean that the edge plasma is an area of concern which is addressed in this chapter. As mentioned in chapter 3, the Langmuir RP data can be helpful in determining the conditions in the SOL; however, RP measurements could not be taken in H-mode, as explained in section 3.4, so it is not a universal solution to the problem. Due to differing quality of TS diagnostic data from shot to shot, it is necessary to use generic parameterisations for providing data for the edge. This means that the data from different sources can be merged when they are available, and a helpful, smoothed functional form can be delivered to the emission modelling. This is detailed in section 4.2.

4.2 Functional fitting of non-spectroscopic N_e and T_e profile data

The edge radial profiles shown in figure 4.2 indicate the advantage of combining different sources of data when defining the plasma conditions at the edge of the plasma. The uncertainty in the pure TS data at the edge can lead to non-physical parametric N_e and T_e profiles. An alternative to relying on TS at the edge was discussed in chapter 3; the Langmuir RP measurements can supplement the TS data in the SOL.

There are certain caveats when dealing with RP compared to TS measurements on MAST. Firstly, TS is a standard plasma diagnostic which is used during every shot. In contrast, RP measurements must be specifically requested prior to the experimental session, and the path of the probe through the plasma defined to give the best representation of the radial profiles. Although the RP measurements give useful N_e and T_e diagnosis at the plasma edge, the irregularity of probe measurements is problematic for this application. Secondly, since TS is a standard plasma diagnostic, the data held in the central MAST repository is in a standard form: in the case of the Nd:YAG TS, N_e and T_e as a function of time and position. The RP data is not held in such a useful form; extra *ad hoc* processing is necessary to extract the diagnostic data required.

Figure 4.3(a) shows the raw signal from the Langmuir RP measurement of T_e in MAST. It is difficult to discern the average T_e variation from this plot due to the high frequency noise on the signal. Figure 4.3(b) shows the same data after being processed through low pass filters with 1 kHz and 100 Hz cut-off frequencies[137]. The frequency response of the low pass filter was, in this case, given by:

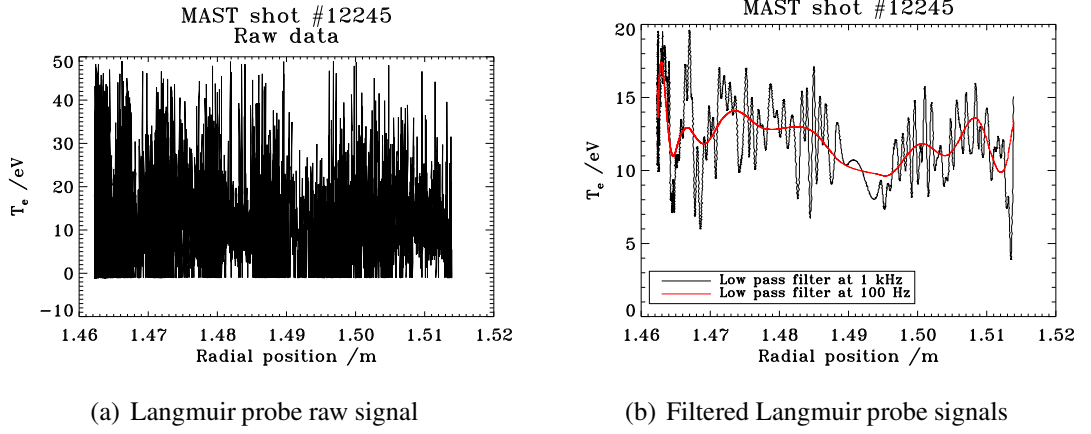


Figure 4.3: 4.3(a) shows the raw signal from the Langmuir RP measurement of T_e . 4.3(b) shows the same signal passed through a low pass filter with 1 kHz and 100 Hz cut-off frequencies. The low-frequency component of the signal gives a far clearer picture of the T_e variation.

$$G(f) = \frac{1}{\sqrt{1 + \left(\frac{f}{f_c}\right)^2}} \quad (4.1)$$

where f is the frequency and f_c the cut-off frequency[138].

As shown in figure 4.3(b), the Langmuir RP measurements are then do yield useful data. It has been the practice during this work to make use of the RP data if it exists by merging it with the TS data, and solely using the TS when RP data is unavailable.

Whether the RP data is available or not, one can take advantage of the pedestal model of the tokamak edge[139, 140]. Since there is a well-known shape for the N_e and T_e profiles, one can use the data available in a fitting routine to parameterise the plasma edge. The profile shapes suggest the use of a modified hyperbolic tangent function. The original parameterisation is[141]:

$$\text{mtanh}_{\text{orig.}}(z, \mathbf{a}) = \frac{a_1 - a_2}{2} \left[\frac{(1 + a_3 z) \exp(z) - \exp(-z)}{\exp(z) + \exp(-z)} \right] + a_2 \quad (4.2)$$

where:

- $z = (a_4 - r) / (2a_5)$;
- r is the radial position in the device;
- a_1 is the relative height of the pedestal;
- a_2 is the SOL density or temperature;

- a_3 is the linear core slope;
- a_4 is the position of the transport barrier;
- a_5 is the width of the transport barrier.

During this work there were some difficulties in using this particular parameterisation, especially for the electron density as it often returned densities which were less than zero. The representation decided upon instead is that used to parameterise the edge of ASDEX-U[142], which applies separate modifications on either side of the separatrix:

$$f = \frac{b_1 + b_2}{2} + \frac{b_2 - b_1}{2} \text{mtanh}_{\text{alt.}}(z', b_{5-10}) \quad (4.3)$$

where:

$$z' = \frac{b_3 - r}{b_4} \quad (4.4)$$

and:

$$\begin{aligned} \text{mtanh}_{\text{alt.}}(z', b_{5-10}) = & \left[(1 + b_5 z' + b_6 z'^2 + b_7 z'^3) \exp(z') \right. \\ & \left. - (1 + b_8 z' + b_9 z'^2 + b_{10} z'^3) \exp(-z') \right] \\ & \times \frac{1}{\exp(z') + \exp(-z')} \end{aligned} \quad (4.5)$$

This parameterisation works well given the detailed features observed from the relatively high-resolution non-spectroscopic diagnostics. The use of the original parameterisation in the deduction of N_e and T_e radial profiles will be discussed in section 4.9.

4.3 Levenberg–Marquardt algorithm

A modified version of the Levenberg–Marquardt algorithm[143] is used to fit the TS and Langmuir RP data to the modified hyperbolic tangent function given in equation 4.5.

The first step in fitting the diagnostic data to the required function was to evaluate the function for an initial set of fitting parameters \mathbf{b} , as defined in section 4.2. The data points have an uncertainty associated with them, Δy_k , which is used to determine the weighting attributed to the data points, w_k , such that

$$w_k = \frac{1}{\Delta y_k^2} \quad (4.6)$$

The individual free parameters, b_i , are then varied by an amount δb_i independently, and sets of similar solutions are found. From these different solution sets, the variation of the fitting function with respect to the parameters can be calculated:

$$\frac{\partial f_k}{\partial b_i} = \frac{f'_k - f_k}{\delta b_i} \quad (4.7)$$

where f_k and f'_k are the initial and altered value of the fitting function due to the parameter change δb_i , respectively.

A matrix, M , and vector, \mathbf{c} , can then be formed

$$M_{ij} = \sum_{k=1}^N \frac{\partial f_k}{\partial b_i} \frac{\partial f_k}{\partial b_j} w_k \quad (4.8)$$

$$c_i = \sum_{k=1}^N \frac{\partial f_k}{\partial b_i} (y_k - f_k) w_k \quad (4.9)$$

and improvements can be made to the free parameters by solving the linear system for $\Delta \mathbf{b}$

$$M \Delta \mathbf{b} = \mathbf{c} \quad (4.10)$$

where Δb_i are the changes to be made to the individual parameters such that the improved parameters are $b'_i = b_i + \Delta b_i$.

This procedure is iterated upon until χ^2 , defined as

$$\chi^2 = \sum_{k=1}^N (y_k - f_k)^2 w_k \quad (4.11)$$

converges on its minimal value¹. The number of degrees of freedom, d , in the fitting is defined in terms of the number of experimental data points, N , and the number of free parameters, n , as

$$d = N - n \quad (4.12)$$

which allows the normalised χ_n^2 to be defined as

¹Strictly speaking, the Levenberg–Marquardt routine iterates to a local, rather than global, minimum of χ^2 .

$$\chi_n^2 = \frac{\chi^2}{d} \quad (4.13)$$

which is useful in modelling. $\chi_n^2 = 1$ means there is a ‘perfect’ fit to the data, and $\chi_n^2 < 1$ means the data has been over-fitted; that is, there are too many parameters representing the data.

The implementation of the fitting method used in this work made use of damping factors, λ , to aid convergence. Three different M matrices were calculated such that the leading diagonal was altered to

$$M'_{ii} = M_{ii} (1 + \lambda) \quad (4.14)$$

where $\lambda \in \{0.0, 0.1, 0.2\}$. The χ^2 quantity is calculated for each of the values of λ and the best damping factor is selected. When χ^2 is far from convergence, the larger damping factor is used, and as the system approaches the optimal solution, the damping factor is removed by setting $\lambda = 0.0$.

The percentage error in a parameter can be found from the leading diagonal of the covariance matrix

$$C = M^{-1} \quad (4.15)$$

and the correlation between two parameters b_i and b_j can be defined in terms of the covariance matrix as

$$\text{cor}(b_i, b_j) = \frac{C_{ij}}{\sqrt{C_{ii} C_{jj}}} \quad (4.16)$$

where $-1 \leq \text{cor}(b_i, b_j) \leq 1$. If two parameters are linearly independent, they will have a correlation of zero. This means the effect induced by altering one parameter cannot be undone by altering another parameter. If $\text{cor}(b_i, b_j) > 0$ then the effect of increasing parameter b_i can be undone by decreasing parameter b_j . The two parameters would be considered correlated. If $\text{cor}(b_i, b_j) < 0$ then the effect of increasing parameter b_i can be undone by increasing parameter b_j . The two parameters would be considered anti-correlated. The degree of correlation between two parameters is important since one would prefer the fitting parameters used to be linearly independent. For this work, $|\text{cor}(b_i, b_j)| < 0.4$ was considered a reasonable correlation with which to work, since it results in an ‘‘explained variance’’ of 16%. That is, 16% of the variance in one parameter is explained, or predicted, by the other parameter. This is appropriate given the approximate global uncertainty of the system.

Another important use of the covariance matrix, C , is to give the uncertainty in the

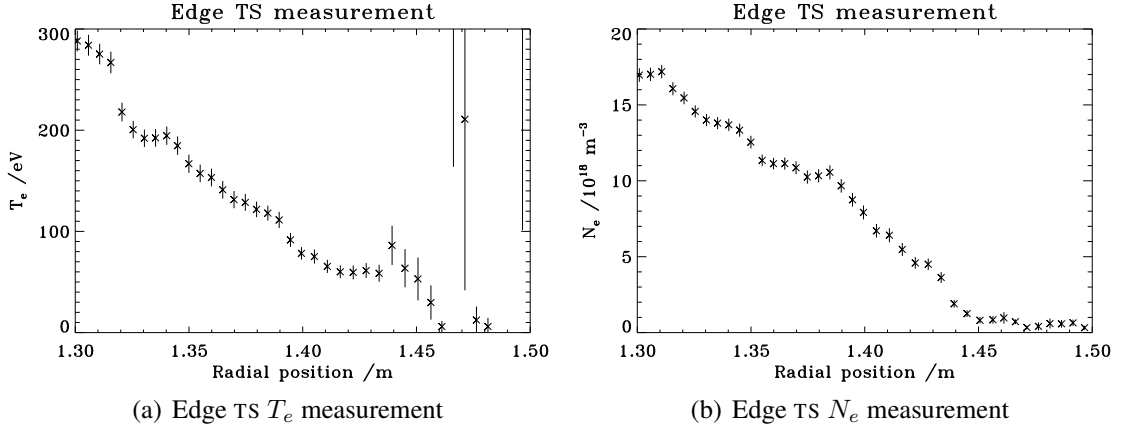


Figure 4.4: Edge TS measurements for MAST shot #12209. One can see that the uncertainty in the temperature measurement is relatively large at the plasma edge.

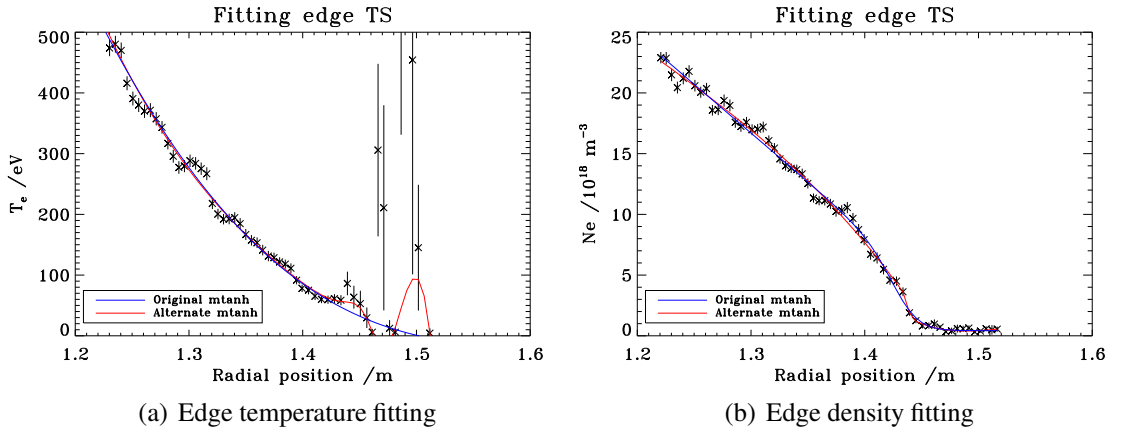


Figure 4.5: MAST shot #12209. 4.5(a) shows the original and alternate functional fittings for the TS edge temperature and 4.5(b) shows a similar plot for the density. For the density: χ_n^2 (orig.) $\simeq 1.51$ and χ_n^2 (alt.) $\simeq 1.37$. For the temperature: χ_n^2 (orig.) $\simeq 2.44$ and χ_n^2 (alt.) $\simeq 2.19$.

fitting function, f , at the experimental abscissae:

$$\Delta f_k = \sqrt{\sum_{i=1}^n \sum_{j=1}^n \frac{\partial f_k}{\partial b_i} \frac{\partial f_k}{\partial b_j} C_{ij}} \quad (4.17)$$

Figure 4.4 shows the edge TS measurements for MAST shot #12209. One can see that the uncertainty in the temperature measurement is relatively large at the plasma edge.

The TS data was fitted using the original mtanh function given in equation 4.2 and with the alternate function given in equation 4.5. Both these functions, with the given parameterisations, are shown in figure 4.5.

The behaviour of the alternate fitting function in the SOL, as shown in figure 4.5(a),

may appear strange, following erroneous points; however, this gives a good indication that the alternate function will follow the more accurate RP data in the SOL without compromising the fit on the other side of the separatrix. A comparison of the χ_n^2 quantity for both parameterisations shows that the alternate function more accurately fits the experimental data:

- density:
 - original parameterisation: $\chi_n^2 \simeq 1.51$;
 - alternate parameterisation: $\chi_n^2 \simeq 1.37$;
- temperature:
 - original parameterisation: $\chi_n^2 \simeq 2.44$;
 - alternate parameterisation: $\chi_n^2 \simeq 2.19$.

In practice, if the TS data were as erratic as that in figure 4.5(a), and there was no source of supplementary data, such as RP measurements, a simple exponential decay formulation would be used with perhaps two decay lengths over the extent of the SOL. If RP data is available, the data sources are merged and the resultant best diagnostic representation of the plasma edge is used. MAST shot #12245 is an example of the merging and fitting procedure.

To merge the TS and RP diagnostic data one has first to assign an uncertainty to the RP data. Figure 4.3 shows the raw and filtered RP data. The filtered data can be used to estimate the uncertainty in the measurement. The signal filtered at 100 Hz in figure 4.3(b) gives a good indication of the variation of the temperature as measured; the signal filtered at 1 kHz can be used to determine the uncertainty which forms an envelope around the measured temperature.

The TS measurements with high uncertainty near the edge were discarded where the RP data was taken. This merged data, with associated uncertainties, then formed the data set which was fitted with the alternate mtanh function defined in equation 4.5. The merged experimental data and the fitted function are shown in figure 4.6. The χ_n^2 for the functional fit on the merged data set is $\chi_n^2 \simeq 2.41$.

The value of χ_n^2 for the merged data is larger than that of the un-merged data. This is as expected since the relative uncertainty in the RP data is much smaller than that of the TS at the same radial position. The larger uncertainty in the TS makes it easier to fit the function to the un-merged data since the weighting of the data points is inversely proportional to the square of the uncertainty.

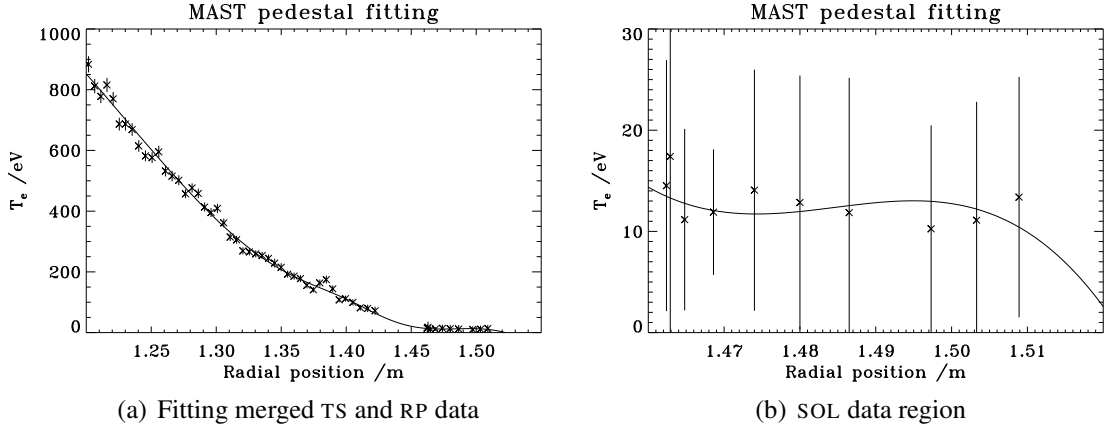


Figure 4.6: MAST shot #12245. The RP measurements have been merged with the TS data to give a composite data set. This merged data is then fitted using the Levenberg–Marquardt routine, with $\chi_n^2 \simeq 2.41$. This value of χ_n^2 is larger than that of the un-merged data due to the relative uncertainty in the RP measurements being much lower than the corresponding TS data.

It is clear from figure 4.6(a) that the parameterised fit of the merged data set has adequately followed the measurements inboard of the separatrix, as was the case in the un-merged case. It is also clear from figure 4.6(b) that the function properly follows the SOL temperature, as measured by the Langmuir RP. The merging of the density data was also successful; $\chi_n^2 \simeq 1.77$ and the fit is shown in figure 4.7.

The increased regularity of the parameterisation of the merged density and temperature data allows for a more reliable predictive model of the radial metastable populations. The fitted function is less variable, but is closer to the reality regarding neutral helium transport at the plasma edge. Figure 4.8(a) shows the parameterised density function, shown with the experimental data in figure 4.7, and 4.8(b) shows the temperature function, as shown in figure 4.6. Figure 4.8(c) shows the variation of the $1s^2\ ^1S$ and $1s2s\ ^3S$ states as calculated radially using the predictive model. One can see that the $1s2s\ ^3S$ population increases as the temperature in the SOL increases, although it does not reach equilibrium with the ground state, before decaying exponentially due to the increased temperature and density of the confined plasma. Figure 4.8(d) shows the variation of the $1s2s\ ^3S$ state relative to the ground state.

A comparison of figures 4.2(d) and 4.8(c) shows that the evolution of the metastable population is far smoother when using the merged data set rather than the un-merged; this is due to the smooth and realistic variation of the temperature and density over the entire region when both TS and RP data are used. It should be noted that there is a marked change in derivative of the curve in figure 4.8(d), which corresponds to the change in density gradient; clearly this is due to the larger ionisation cross-section of

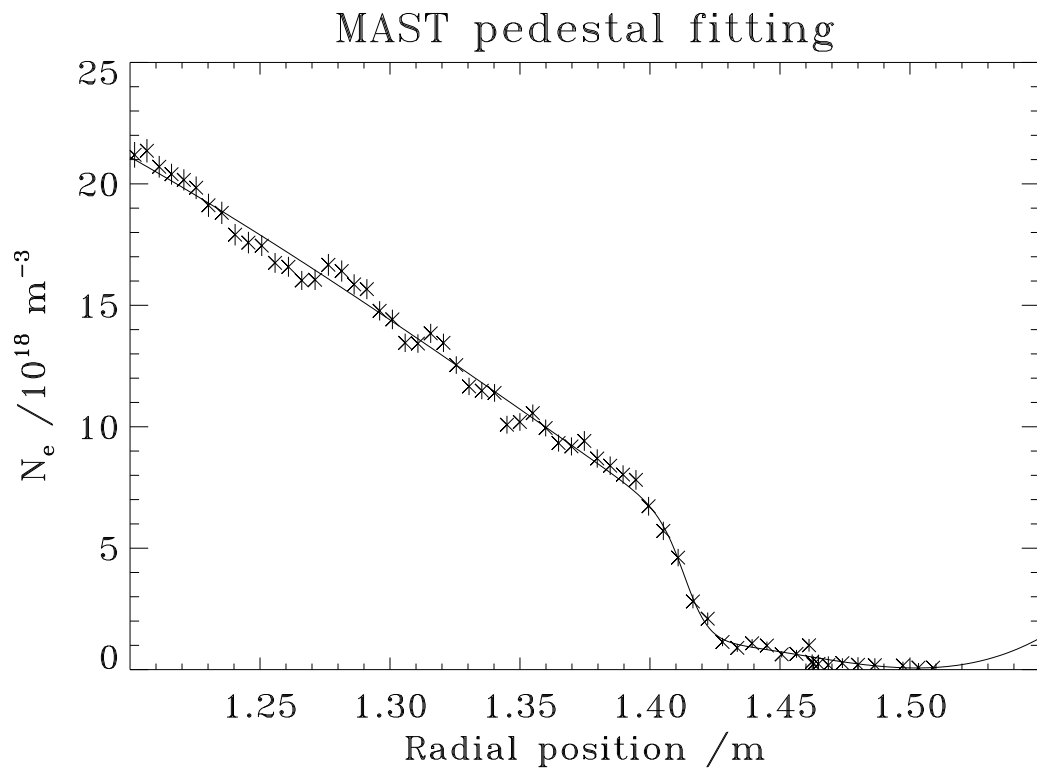
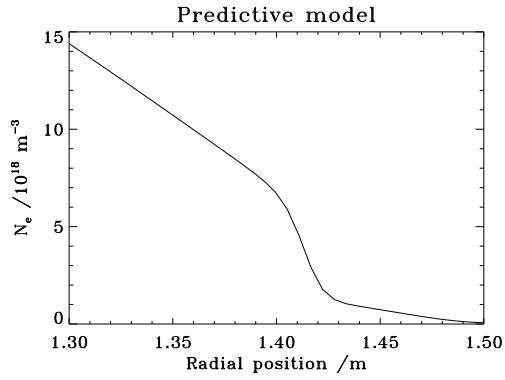
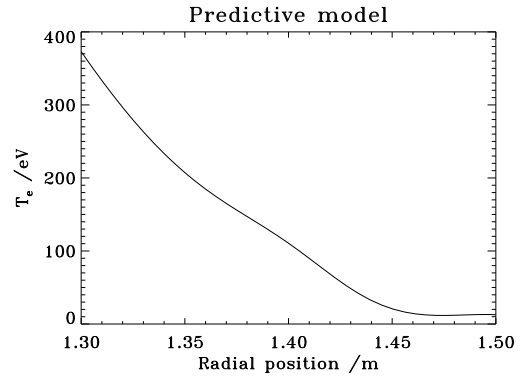


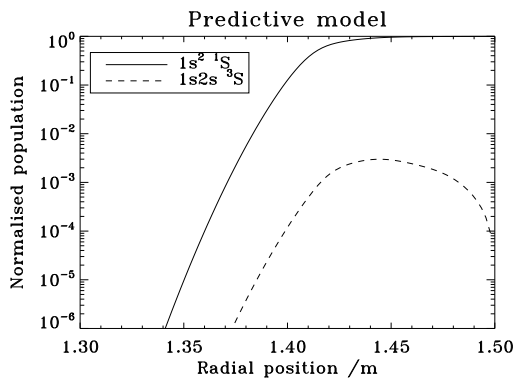
Figure 4.7: MAST shot #12245. The data has been merged in a similar way to figure 4.6 with $\chi_n^2 \simeq 1.77$.



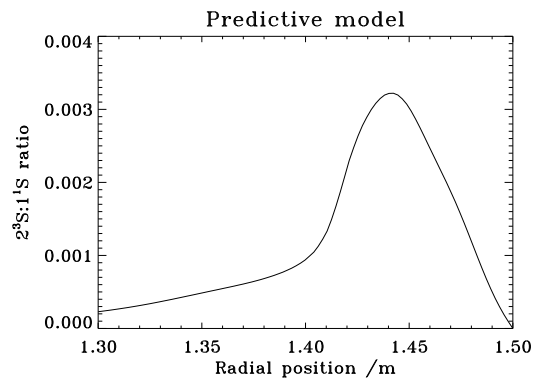
(a) Functional form of N_e



(b) Functional form of T_e



(c) Variation of the metastable populations



(d) Variation of $1s2s\ ^3S$ relative to $1s^2\ ^1S$

Figure 4.8: MAST shot #12245. Shows the variation of the metastable populations due to the functional fitting of the merged diagnostic data. See text for details.

$1s2s\ ^3S$ compared to $1s^2\ ^1S$.

The radial variation of the metastable populations is calculated using an attenuation model based on ADAS theoretical collision data. In section 4.4, the spatially resolved population structure is calculated with uncertainties in the N_e and T_e profiles included by applying a Monte Carlo statistical sampling method. These populations will then be used to calculate spatially resolved emission from the lines of interest in section 4.5 with uncertainty bars. Then section 4.6 will discuss work to represent the HELIOS spectrometer's viewing geometry so as to determine whether local T_e and N_e predictions can be extracted from the spectra. By comparing the theoretically anticipated emission calculated by the model with that measured, the collimation of the HELIOS injection nozzle will be determined and the toroidal localisation of emission will be determined using the Levenberg–Marquardt routine described above.

4.4 Calculating spatially resolved metastable populations

The Monte Carlo statistical sampling method was employed to calculate the spatially resolved metastable populations and their associated uncertainties using the merged TS and RP data from MAST shot #12245 described above. Figure 4.9 shows the different stages required in calculating the $1s^2\ ^1S$ and $1s2s\ ^3S$ populations and uncertainties for a radial attenuation of neutral helium.

The metastable populations change with position such that

$$\frac{d}{dr} \begin{bmatrix} N_g \\ N_m \end{bmatrix} = \begin{bmatrix} -S_{g \rightarrow +} - q_{g \rightarrow m} & q_{m \rightarrow g} \\ q_{g \rightarrow m} & -S_{m \rightarrow +} - q_{m \rightarrow g} \end{bmatrix} \begin{bmatrix} N_g \\ N_m \end{bmatrix} \frac{N_e}{v_{\text{puff}}} \quad (4.18)$$

where S represents the ionisation rate coefficient de-populating a state and q the rate coefficient which populates one state from the other. These rate coefficients are implicitly functions of temperature and density.

As shown in figure 4.9, the merged temperature and density diagnostic data is accessed, and the ionisation and cross-coupling rate coefficients are determined on this mesh of temperature and density. A random temperature and density are selected from within a Gaussian distribution defined by the uncertainty at the point of interest and a fourth order Runge–Kutta routine is used to solve the system above[144]. A bilinear interpolation routine is used to find the values of the rate coefficients at the intermediate points required by the Runge–Kutta algorithm. A comparison of different numbers

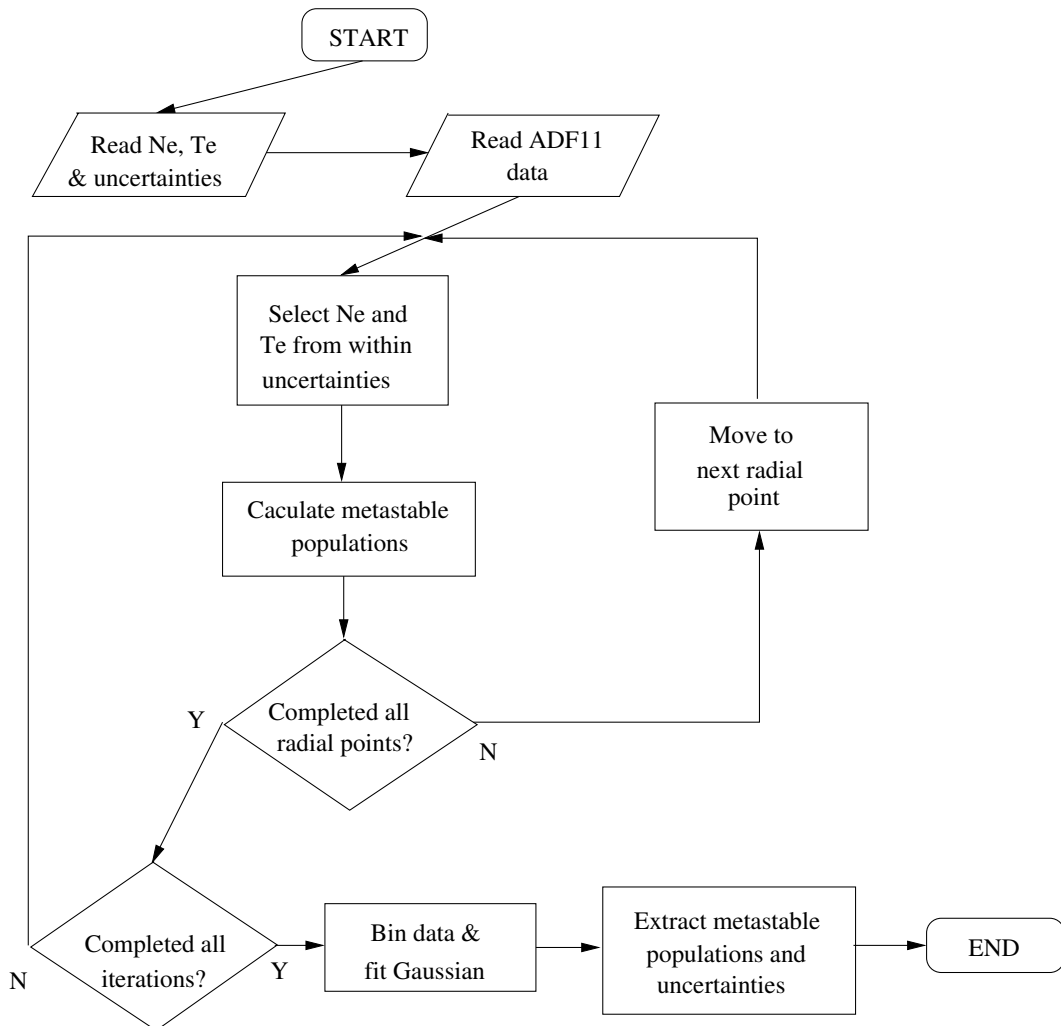


Figure 4.9: The different stages required in calculating the $1s^2\ ^1S$ and $1s2s\ ^3S$ populations and their associated uncertainties.

of iterations and the effect on the uncertainties produced was carried out and it was determined that 10^4 iterations and 100 bins was adequate to deduce the uncertainty. The process was iterated 10^4 times over all radial positions. The 10^4 values of the $1s^2^1S$ and $1s2s^3S$ populations per position were then put in 100 bins and a Levenberg–Marquardt procedure was used to fit a Gaussian to the two data sets. The peak position of the Gaussian indicated the value of the population, and the half-width indicated the uncertainty. Figure 4.10(a) shows a histogram of the binned population data along with the Gaussian fit used to extract the population and uncertainty data. Figures 4.10(b) and 4.10(c) show the radial variation of the metastable populations with their associated uncertainties².

To calculate the spatially resolved metastable populations, a similar structure to that shown in figure 4.9 was used, but moved through the different beamlets used to represent the gas puff. The flux of gas from the nozzle is set as an initial condition, and the collimation of the nozzle is used to calculate the initial helium population on a particular beamlet. For this piece of work, the angular variation of the nozzle was taken as $\cos^5(\theta)$, and the initial $1s^2^1S$ population of a beamlet at an angle θ_i to the device radius was normalised to the total input population, P_{tot} , by

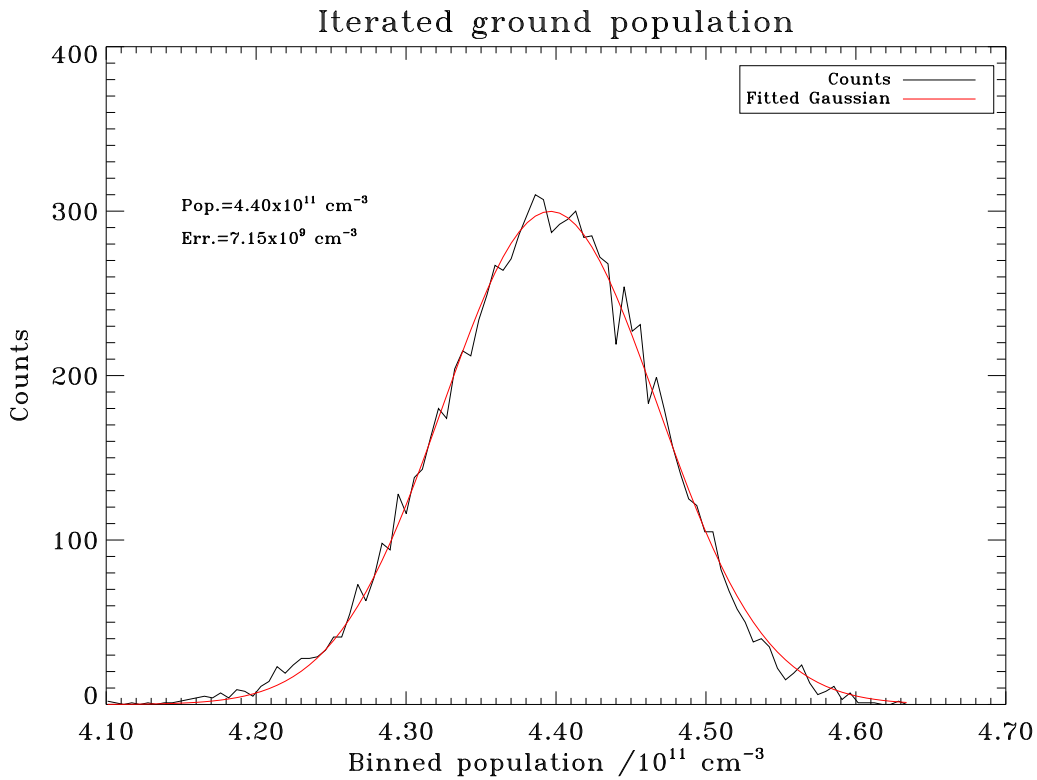
$$P(\theta_i) = P_{\text{tot}} \left[\int_{-\pi/2}^{\pi/2} \cos^n \theta \, d\theta \right]^{-1} \int_{(\theta_i+\theta_{i-1})/2}^{(\theta_i+\theta_{i+1})/2} \cos^n \theta \, d\theta \quad (4.19)$$

Equation 4.19 shows the general form of the angular collimation; $\cos^n(\theta)$ is present rather than the $\cos^5(\theta)$ used in this case. This general form will be used when attempting to determine the angular collimation of the injection nozzle; that is, the search parameter is n .

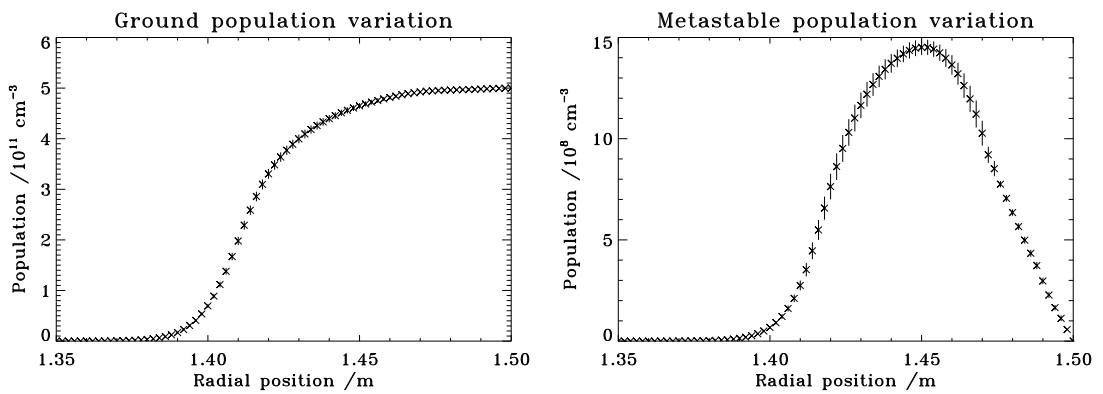
Figure 4.11 shows the metastable populations in the vicinity of the injection nozzle as a function of radial position and angle from the device radius assuming a $\cos^5(\theta)$ angular variation. As one would expect, the ground state population declines sharply along a curve of the surface; this shows the separatrix, where the density begins to increase substantially from its SOL value. One can also see the population of the $1s2s^3S$ state in the SOL due to the low density and subsequently low de-population mechanisms. This spatially resolved picture shows that there is a significant amount of neutral helium at relatively large angles from the device's radial vector; it is worth noting that, assuming a $\cos^5 \theta$ variation, the $1/e$ angle for the initial population is $\theta \simeq 35^\circ$.

The calculation of the metastable populations and their associated uncertainties

²It is noted at this point that this method assumes there is no uncertainty in the atomic reaction rate coefficients. In principle it would not be difficult to include these uncertainties; a rigorous procedure for propagating an uncertainty in Υ to the derived coefficients is currently underway.



(a) Binned population data for with Gaussian fit



(b) Radial variation of $1s^2\ ^1S$ with associated uncertainty

(c) Radial variation of $1s2s\ ^3S$ with associated uncertainty

Figure 4.10: 4.10(a) shows the binned data for one of the radial points with the Gaussian fitted to extract population and uncertainty. 4.10(b) and 4.10(c) show the calculated populations for both metastables with uncertainties.

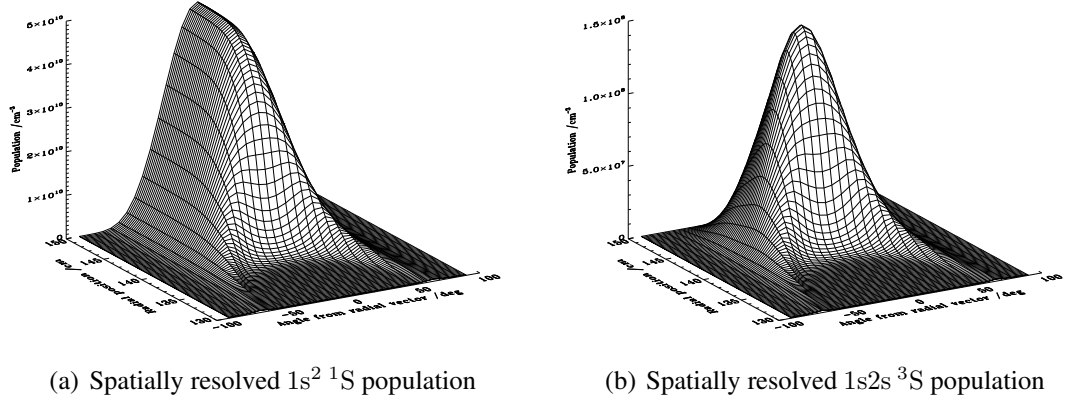


Figure 4.11: The spatially resolved metastable populations calculated using the merged diagnostic data from MAST shot #12245.

allows the theoretically anticipated emission to be calculated for the three diagnostic lines of interest, which will be discussed in section 4.5.

A simple tabular look-up method was discussed towards the end of section 3.4; this entails an assumption that the ground to metastable relative populations are in local equilibrium. It is clear from the metastable emission modelling carried out in this section that the $1s2s \ ^3S$ state is not always in equilibrium with the ground state. There is a region of non-equilibrium throughout the SOL where the $1s2s \ ^3S$ state tends towards an equilibrium value but does not necessarily reach that value. This means that a simple look-up routine is generally inadequate to deduce the radial temperature and density variation in the SOL; this leaves a region in the vicinity of the separatrix where the simple technique agrees with TS; see figure 3.22.

4.5 Calculating spatially resolved emissivities

Using GCR modelling, the spatially resolved metastable populations can be used to calculate the emission of the three lines of interest, as given in table 3.1 on page 61. The emission due to a particular transition can be written in terms of the photon emissivity coefficient, introduced in section 2.4:

$$\varepsilon_{ij} = \sum_{\sigma} N_{\sigma} N_e \mathcal{P}\mathcal{E}C_{\sigma,ij} \quad (4.20)$$

where the summation is over the number of metastables in the ionisation stage³. In the case of the neutral helium of interest in this work, the emission therefore explicitly

³Section 2.4 mentions the excitation and recombination components of the emission; however, as recombination was found to be negligible, the excitation specification has been dropped for brevity.

becomes

$$\varepsilon_{ij} = N_e (N_g \mathcal{P}\mathcal{E}\mathcal{C}_{g,ij} + N_m \mathcal{P}\mathcal{E}\mathcal{C}_{m,ij}) \quad (4.21)$$

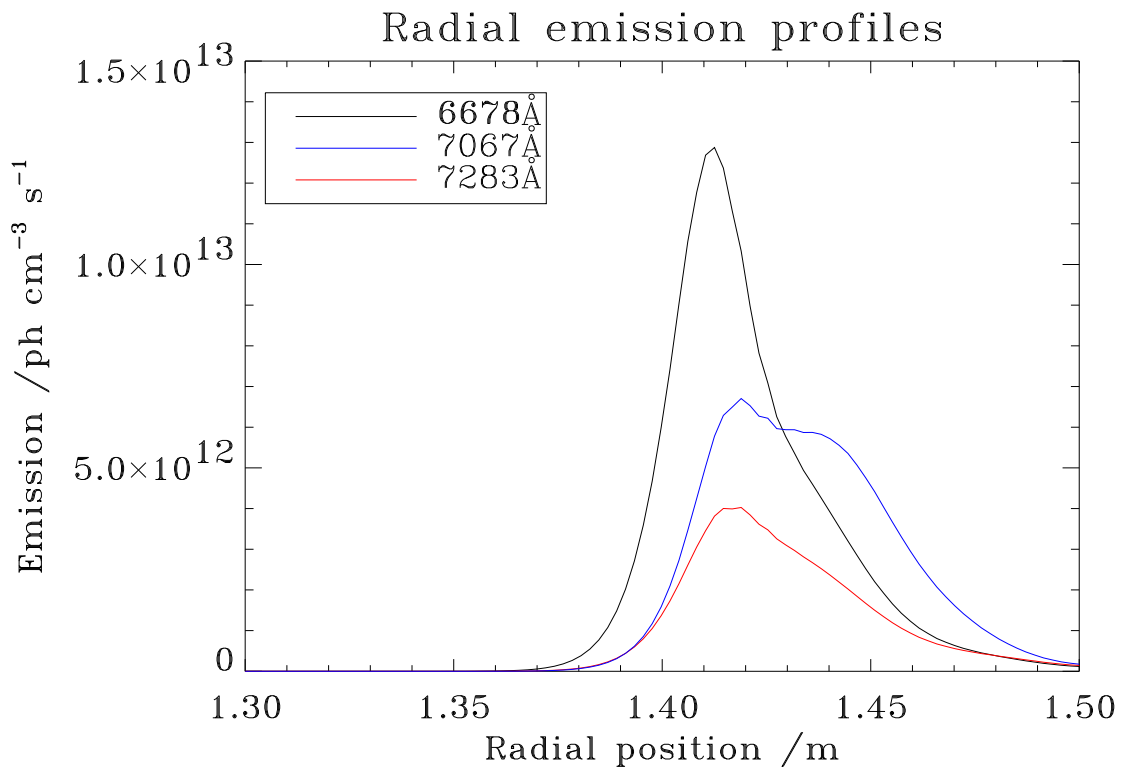
The radial variation of the ground and metastable populations, N_g and N_m , was calculated in the previous section; therefore, all that is necessary to calculate the emission on the lines of interest are the $\mathcal{P}\mathcal{E}\mathcal{C}$ rate coefficients for the two metastables and the relevant transitions.

The $\mathcal{P}\mathcal{E}\mathcal{C}$ s used in this work were calculated using the distribution-averaged collision strengths discussed in section 2.2.1, based on the RMPS calculation discussed in section 2.1, and the interval-averaging and merging techniques discussed in sections 2.2 and 2.3. A code from the ADAS package, ADAS 208, was used to produce the $\mathcal{P}\mathcal{E}\mathcal{C}$ data files. Figure 4.12(a) shows the radial variation of the three lines of diagnostic interest due to the temperature and density profiles in 4.8(a) and 4.8(b) and the metastable populations shown in figure 4.8(c). Figures 4.12(b) and 4.12(c) show the contribution due to the two metastables to the 6678 Å and 7067 Å lines respectively.

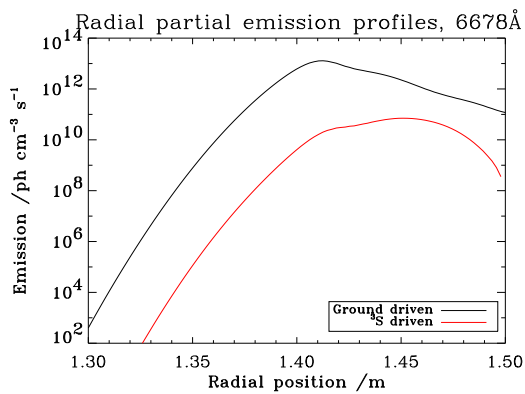
One can see that the three lines reach their peak emission at approximately the same radial position, but the 7067 Å line, due to the triplet transition, emits more in the SOL than the two singlet lines. Figure 4.12(b) shows that the 6678 Å emission driven by the ground is around two orders of magnitude greater than that driven by the ^3S metastable. In contrast, figure 4.12(c) shows that the opposite is the case for the 7067 Å line. Even though the triplet population is far lower than that of the ground state, the contribution to the emissivity from the ^3S is greater than that driven from the ground. This is an interesting finding since the majority of this line's emission is driven by a population that is not necessarily in equilibrium with the ground state. This would therefore suggest a simple look-up of line ratios would give a poor temperature diagnostic in this case. That is exactly what has been observed in the shot shown in figure 3.22. The structure of the triplet emission is noted; the effects of the differing temperature and density gradients are visible as features on the profile.

In a similar way to before, the anticipated emission from the three spectral lines can be calculated with their associated uncertainties using the Monte Carlo technique *mutatis mutandis*. The electron temperature and density are iteratively sampled from within a Gaussian distribution determined by the uncertainty limits and a bilinear interpolation procedure is used to find the relevant values of the $\mathcal{P}\mathcal{E}\mathcal{C}$ s. The metastable populations are then sampled from within their uncertainty limits and used to calculate the resultant emission. The data are then fitted with a Gaussian at each point to determine the emissivity and the associated uncertainty.

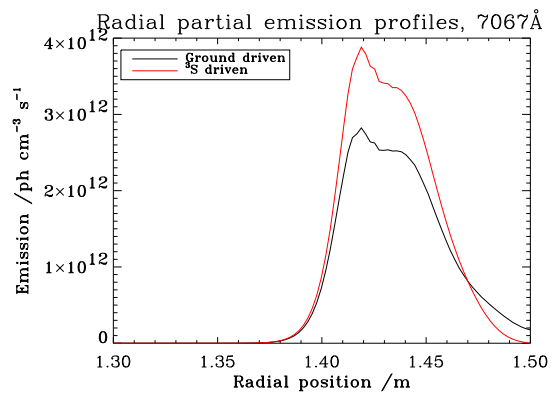
A spatially-resolved emission model clarifies specific unknowns relating to the ex-



(a) Diagnostic emission lines



(b) Contribution to 6678 Å line



(c) Contribution to 7067 Å line

Figure 4.12: The radial emission profiles of the three lines of diagnostic interest due to the temperature and density profiles given in figure 4.8. Note the logarithmic scale on 4.12(b) and the linear scale on 4.12(c).

perimental setup. These are:

- wrap-around — quantify cold emission seen by the spectrometer;
- provide data to form LOS integrals;
- ultimately, allow a Levenberg–Marquardt routine to be used to determine the nozzle collimation.

The second and third items on the above list will be dealt with in section 4.6; the wrap-around can be quantified using the spatially-resolved emission calculated above and technical schematics of the MAST device. Figure 4.13 shows contours of the triplet line emission. The angle between the nozzle position and the viewing port is $\simeq 51^\circ$ [145]. One can see from the lines of sight marked on figure 4.13 that there is significant off-radius emission seen by the detector, however, the contribution along the viewing line cannot be determined at this stage; it is noted that the relatively broad triplet line, figure 4.12(a), could be affected. This will be tackled in section 4.6.

Although line-of-sight integrals are required to study quantitatively the contribution to the observed emission along the path, a qualitative study is possible from figure 4.13. One can see that the majority of viewing chords can observe off-axis emission; that is, emission which is not localised at $\theta = 0$. The lines of sight centred around the separatrix view the most intense emission near the radial vector, but some chords, like the one viewing furthest into the plasma, observes the most intense emission far off axis. This demonstrates the existence of “wrap-around” emission; that is, off-axis emission that can be credulously interpreted as local emission from further into the plasma. This effect, coupled with the increasing attenuation, would tend to deliver poor diagnostic data for the viewing chords observing furthest into the plasma if a simple ratio look-up technique were employed. This divergence agrees with the experimental observation shown in figure 3.22.

This non-localised emission suggests that a comprehensive plasma model is essential if diagnosing plasmas using a gas puff. The agreement between the HELIOS line ratio look-up method and the TS data could be improved if one could reduce the off-axis emission due to “wrap-around”. Yet again, this highlights the crucial importance of knowing the collimation of the neutral helium gas injection system.

4.6 Simulating HELIOS lines-of-sight

Calculating spatially-resolved metastable populations and line emission profiles is of great use in investigating features of the setup that are inaccessible to measurement,

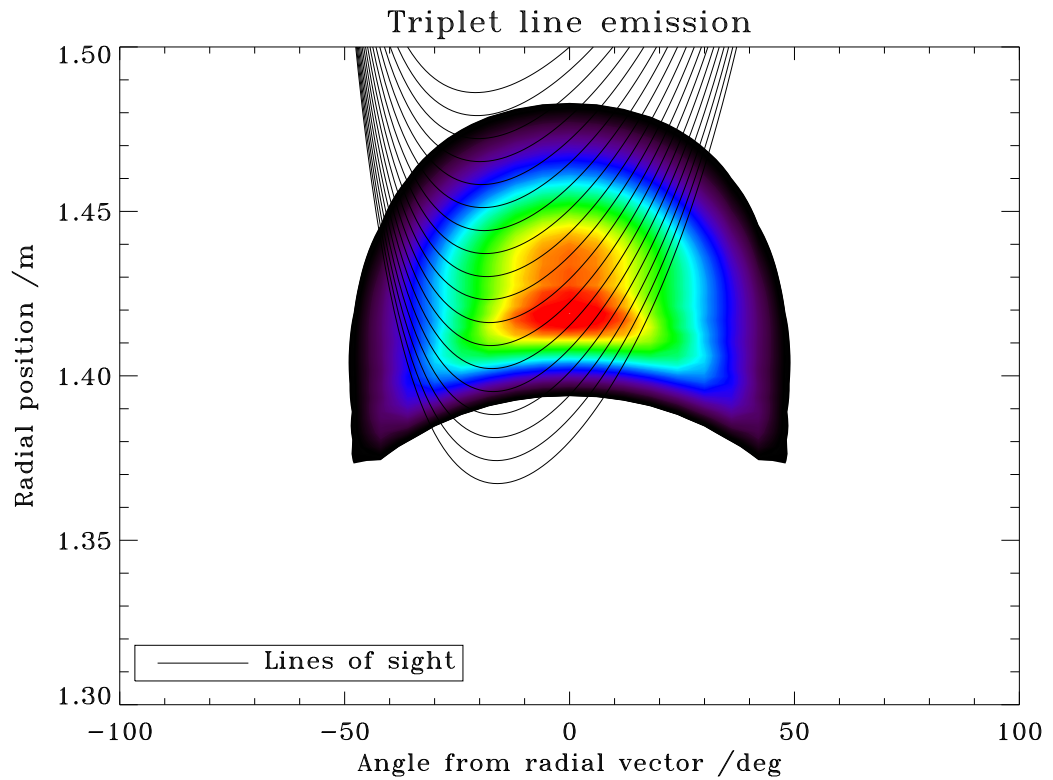


Figure 4.13: The contours on this plot are linearly spaced, with the maximum emission localised in the central region of the plot. One can see that the lines of sight, which appear curved due to the angular abscissae, pass through regions of significant off-axis emission. It is not possible at this stage to determine the contribution of these off-axis components to the lines visible to the detector, but this will be dealt with in section 4.6.

such as the issue of wrap-around emission discussed in the previous section. It is necessary, however, to acknowledge that the experimental hardware does not measure the spatially-resolved quantities calculated so far. In order to confront directly the GCR modelling and measurement, one must consider the spectrometer's view of the plasma; it detects radiation along a line of sight, not from a single position within the plasma.

The line-integrated emissivities are calculated from the grid of spatially resolved emissivities from the GCR model described above:

$$\tilde{\varepsilon}_{ij} = \int_0^{\Lambda} \frac{A}{4\pi\ell^2} \varepsilon_{ij}(\mathbf{r}) d\ell \quad (4.22)$$

where A is the collection area of the optics and ℓ is the position along the viewing chord. The quadrature was carried out using a trapezoidal routine, due to the irregular grid spacing[146]. A support function, ϕ , is used to take the emissivities to the edge of the device by fitting the last two data points to an exponential decay:

$$\phi(\ell \geq \ell_0) = c_1 \exp[-c_2(\ell - \ell_0)] \quad (4.23)$$

where ℓ_0 is on the last beamlet and c_i are fitting coefficients. In equation 4.22, Λ represents the total path length of the integral. In this work, Λ was taken to be the distance at which

$$\left| \frac{\partial\phi}{\partial\ell} \right| \leq 10^8 \text{ ph cm}^{-4} \text{ s}^{-1} \quad (4.24)$$

The contribution to the line-of-sight integrals along the path, mentioned qualitatively in the previous section, can now be investigated using the computational model. From figure 4.13 it is clear that the chords can view one of three regions:

1. a region with no significant emission — the outermost chord views the SOL;
2. a region with significant on-axis emission — the chords in the middle of the bundle view emission in the vicinity of the separatrix, and less intense off-axis emission;
3. a region with significant off-axis emission — the innermost chord views practically no on-axis emission, but does pass through a region of off-axis emission.

The naïve assumption that the HeI emission is localised along the radius of MAST can be tested in these three different cases. The contribution to the integrated emission is shown in figure 4.14. In the first case, one would expect the peak emission to be on-axis, but very weak; in the second case one would, again, expect peak emission

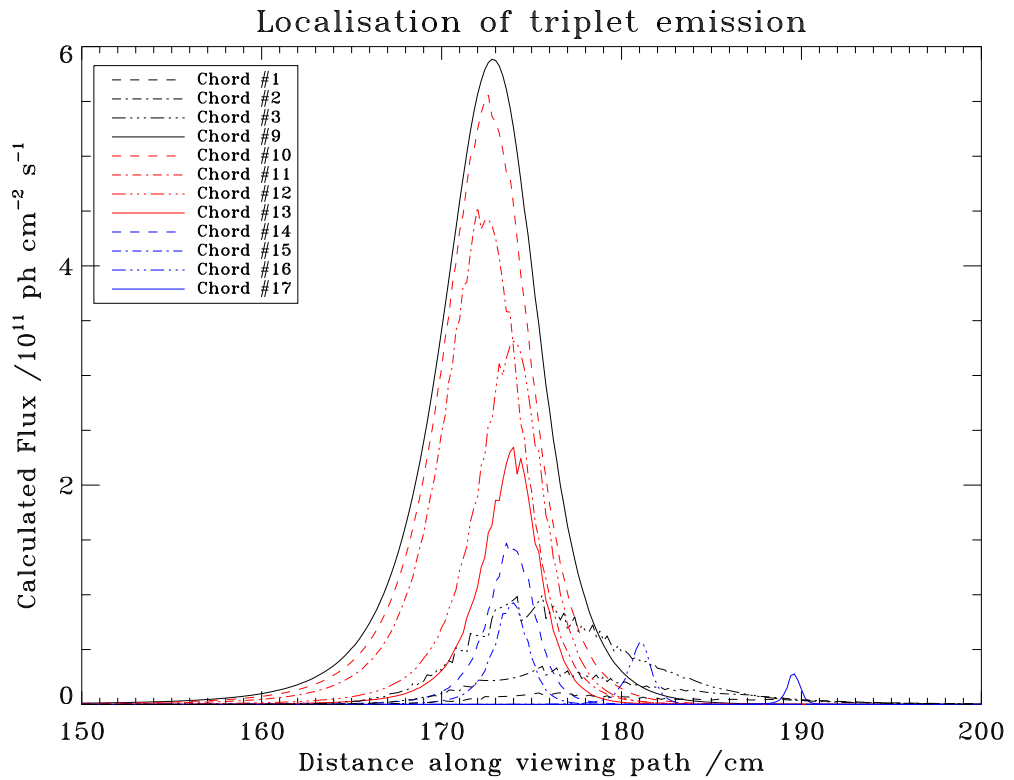


Figure 4.14: MAST shot #12245. One can see that the most intense flux is predicted on the central viewing chord, marked ‘Chord #9’ on the plot. The peak predicted emission is on the radial vector of the device; this can be seen from figure 4.13. Most of the chords anticipate their peak flux on-axis; however, the innermost chords occur well off-axis.

to occur on-axis, but be far more intense; in the third case we would expect distinct off-axis emission. This is the case for the predicted contributions shown in figure 4.14.

It is evident from the calculated contributions to the line-integrated emissivities in figure 4.14 that the innermost chord is predicted to view its peak emission well off-axis. This means the chord is viewing ‘behind’ the region of peak emission and detecting a wrap-around signal. It would therefore be inappropriate to interpret all of the spectra detected by the HELIOS spectrometer as representing locally emitted radiation given the outcome of this theoretical study; this further emphasises the need for a plasma emission model if diagnostic data is to be extracted reliably from the system. The profiles in figure 4.14 take the solid angle into account, so the relatively intense off-axis emission shown in figure 4.13 is shown to be diminished by the small solid angle due to the viewing geometry.

Up to this point, the modelling has delivered the theoretically anticipated

metastable populations and resultant emission based on an application of GCR modelling which is underpinned by the merged TS and RP diagnostic data from MAST shot #12245. With the line-integrated emissivities, $\tilde{\epsilon}_{ij}$, calculated, one can compare the anticipated emission with that measured by the HELIOS spectrometer.

A direct comparison of the measured and theoretical emissivities allows one to deduce the most important parameter in the neutral helium injection system: the collimation of the injection nozzle. The importance of this parameter lies mainly in the difficulties presented in measuring it accurately; therefore a computational approach to the problem is valuable.

As mentioned previously, the population model used to calculate the metastable populations must be given a parameter n which describes the angular variation of the initial helium population. This angular variation is given in equation 4.19. It is clear that this parameter will determine the amount of wrap-around emission observed by the spectrometer; this can be used to help determine its value.

The calculation of the predicted line-integrated emissivities can be used within a Levenberg–Marquardt least-squares fitting procedure to determine the collimation factor, n . It was found that the best fit to the experimental data occurred at a collimation factor much less than expected. Figure 4.15 shows the calculated line emission ratios for different values of n ; it was found that the best fit occurred for $n \simeq 1.2$. It is noted that the value expected, based on similar apparatus used on other experiments, was $n \simeq 5$.

This is an interesting finding and possibly explains the difficulty in measuring the nozzle collimation. The measurement was attempted by positioning a flow gauge at different positions around the nozzle's aperture. The more diffuse the gas flow, the more difficult to measure the collimation; this is clear since the $1/e$ angle for $\cos \theta$ is $\sim 68^\circ$, compared to a value of $\sim 35^\circ$ for $\cos^5 \theta$. The smaller angular gradient makes the measurement more difficult, and the attempt to measure the collimation was inconclusive.

Given the large difference between the expected and calculated collimation factors, it is apposite to conclude that the neutral helium injection nozzle was damaged. An alternative conclusion would be erroneous operation of the fitting procedure, however, this is not consistent with the outcomes of the study. The procedure does converge on a solution, and this solution has been verified in isolation from the fitting procedure using the emission model.

With the best agreement between the model and the measured line intensity ratios occurring for $n \simeq 1.2$, a more accurate contour plot can be made of the spatial variation of the emission. Figure 4.13 shows the variation assuming the expected collimation

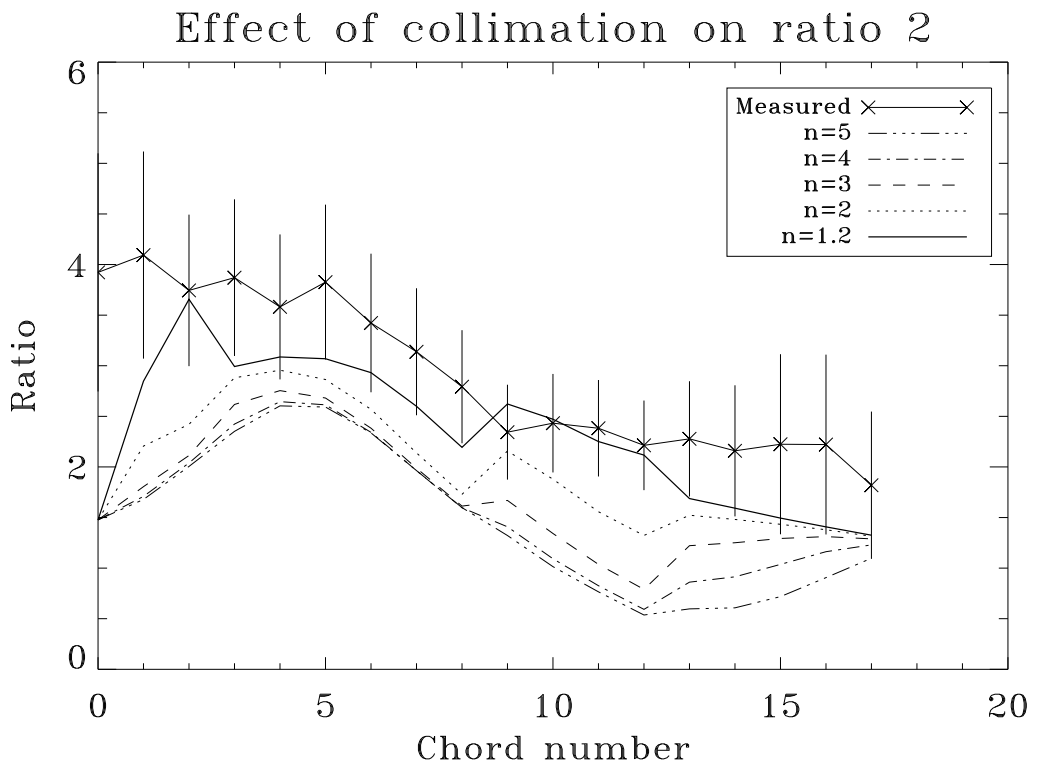
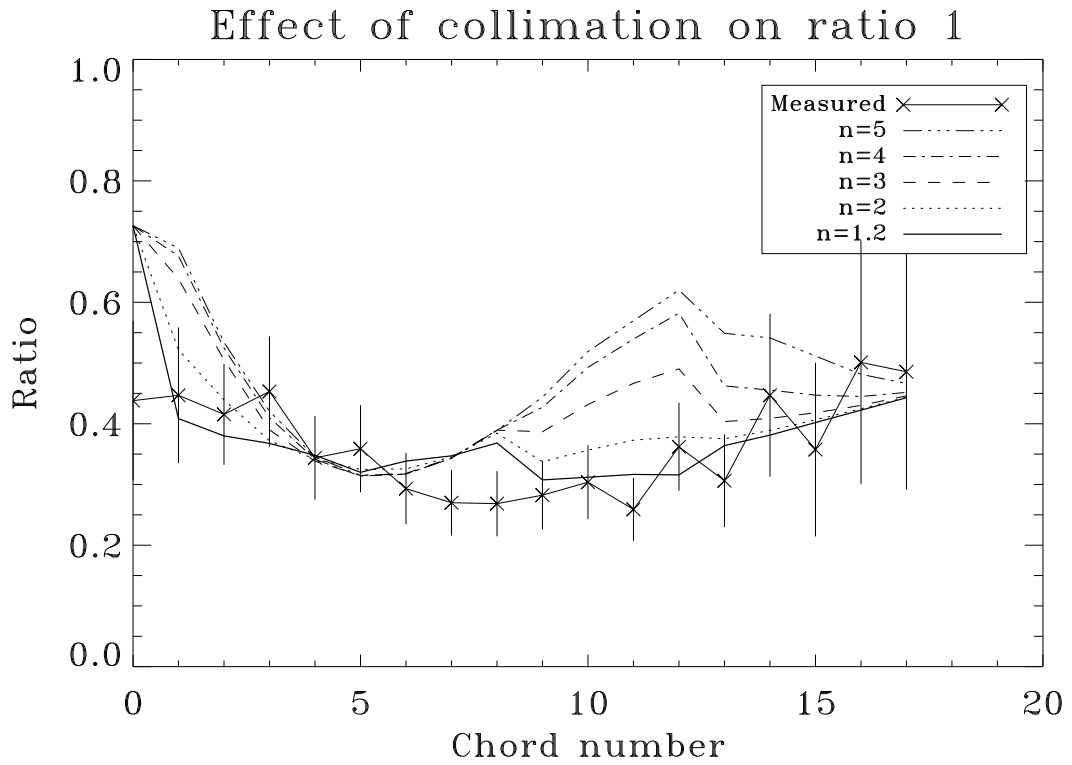


Figure 4.15: The effect of the collimation factor n on the simulated line intensity ratios. The experimentally measured line ratios are indicated by the data points.

factor of $n = 5$; a revision of this plot is given in figure 4.16(a).

It is important to note that the contours on both figure 4.13 and 4.16(a) are on the same levels. Therefore, a comparison of figures 4.13 and 4.16 shows that the collimation which best fits the experimental data leads to less intense emission on-axis, with it extending further around the edge of the MAST plasma, as one would expect. Figure 4.16(b) shows the predicted localisation of emission along the viewing chords using the revised collimation factor and can be compared directly with the theoretical variation in figure 4.14. One can see that the peak contributions are less than in the more collimated assumption, and that the outermost chords see far more emission from the plasma edge than that shown in figure 4.14. The lack of localisation associated with the best fit to the experimental data implies the following:

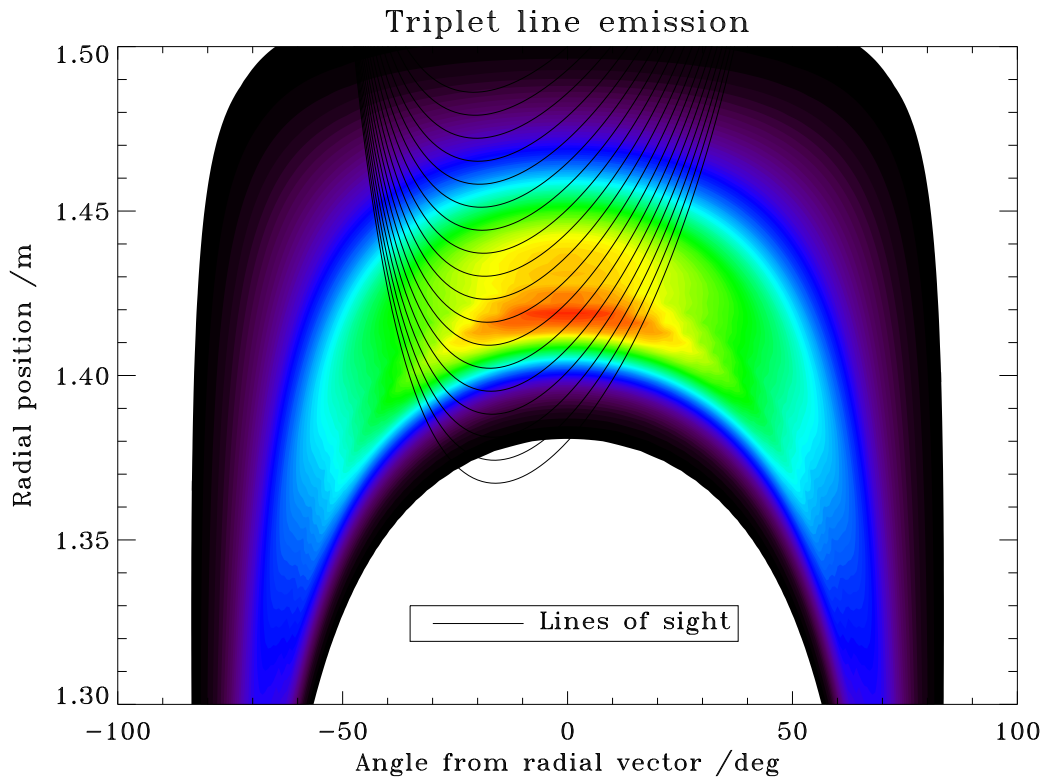
- inference of local density/temperature from the line ratios can have unsafe connection to the actual local density/temperature in the SOL along the central axis of the gas puff;
- the peaked on-axis emission of the central viewing chords indicates that the simple look-up technique would have more connection to axial local density/temperature for these chords;
- the innermost chords exhibit off-axis emission and it would therefore be inappropriate to use the simple look-up method; however, the lack of signal due to attenuation is a far more significant effect on these chords.

These implications of the GCR emission model resonate strongly with what was observed using the the simple line ratio look-up method exemplified in figure 3.22.

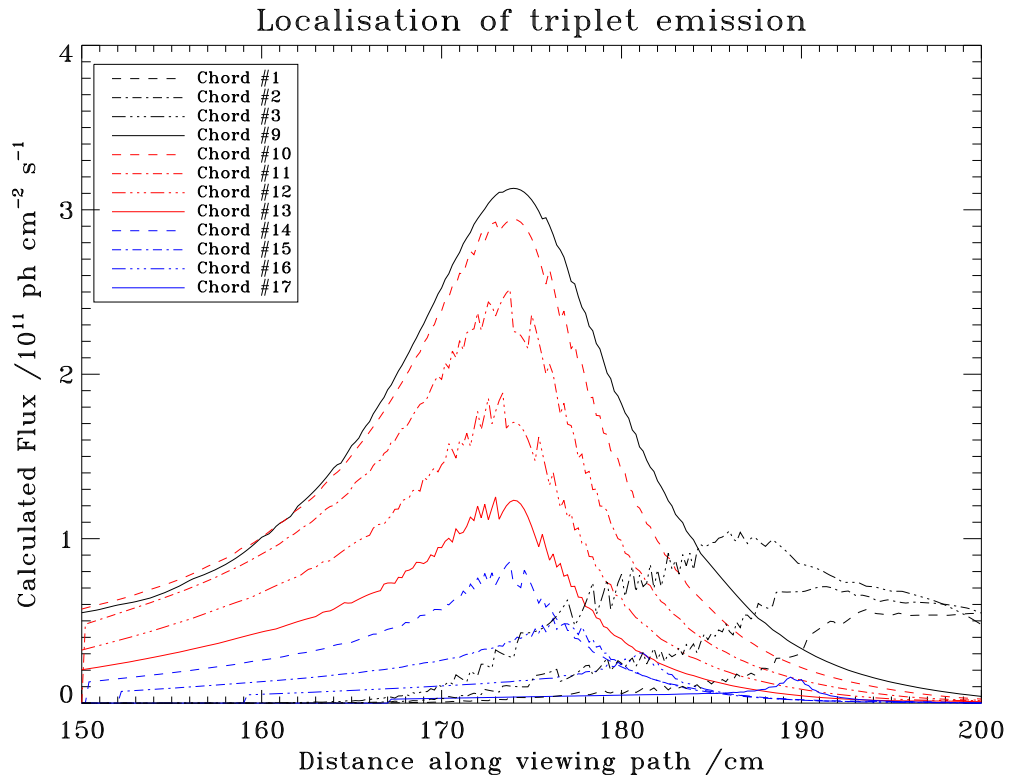
4.7 Temporal variation

As mentioned previously, the system was considered time-independent since the atomic processes responsible for the excited population structure and emission, as deduced in section 2.4, occur on a timescale much shorter than typical plasma timescales τ_{T_e} and τ_{N_e} , as defined in equation 1.4. That is, one need not consider the history of the gas when deducing the spatial variation for a particular time slice. In order to model temporal behaviour, such as plasma boundary variation with ELM activity, one requires additional measured or known data. These are:

- initial neutral helium population;
- N_e and T_e benchmarks from ruby TS;



(a) Spatial variation of triplet-line emission with $n = 1.2$



(b) Revised predicted localisation of triplet emission

Figure 4.16: The predicted spatial variation of the triplet line using a collimation factor of $n = 1.2$, as calculated by fitting the GCR modelled line ratios to the measured data using a Levenberg–Marquardt least-squares fitting procedure.

- temporal variation of N_e and T_e from Nd:YAG TS.

The initial neutral helium population can be determined as discussed in section 3.1, where the throughput evolution of the nozzle was modelled. The spatial variation of the puff can then be calculated as in equation 4.19 using the appropriate normalisation value of P_{tot} . The ruby TS system is used to take a high resolution benchmark measurement of spatial temperature and density variation, with the temporal variation of the plasma parameters deduced from the Nd:YAG system.

The temporal model is evaluated at time-slices corresponding to the trigger times of the Nd:YAG laser. The Nd:YAG configuration used in the experimental periods discussed in chapter 3 had 68 time slices, from an initial trigger at approximately 20 ms, running to approximately 350 ms.

There has been considerable effort in the theoretical modelling and experimental measurement of the radial extent and spatial localisation of ELMs. Research carried out on MAST[147] and ASDEX-U[148] has attempted to compare the spatial structure of type-I ELMs on the small spherical and larger conventional tokamaks[149]. Studies on DIII-D have shown large, rapid, variations in the SOL parameters and fast radial propagation of the ELM pulse[150]. Data has been obtained on MAST from a mid-plane RP[151], mid-plane linear D_α camera and TS[152]. On ASDEX-U, measurements have been made using mid-plane manipulator probes[153, 154] and limiter heat-flux studies[155].

Large radial effluxes of charged particles have been observed on several devices, and it would have been interesting to carry out a thorough investigation of the effect of edge variation on the contributions to line-of-sight integrals; however, this investigation was limited because the Nd:YAG TS radial resolution was insufficient. Initially, the model was used to simulate the temporal behaviour of the HeI emission at times determined by the HELIOS clock pulse. This study showed that the predicted variation agreed well with the line ratios measured using the HELIOS spectrometer, in a similar way to that shown in figure 4.15.

The model was manipulated⁴ to simulate edge density and temperature variations which one could expect during an ELM[156]. The increase in density and shortening of the distance between the injection nozzle and plasma edge meant the emission could be considered localised along the radial vector of the device. The increase in density was taken to be the particles released from the confined plasma during the ELM crash. Developing a predictive model is a notable advantage in this particular investigation since, unfortunately, the timescales of the transient temperature and density increases

⁴This investigation was carried out using the merged data from MAST shot #12245 as a base, with a simulated ELM crash, based on the work in [150] and [156], superimposed.

are far shorter than the HELIOS spectrometer can measure. The model allows one to hypothesise on the behaviour of the emission even though the measurements themselves are not possible. However, a lack of experimental measurement makes this of less practical use than the spatial modelling discussed above. The method of using the thermal neutral gas puff to characterise properly the edge behaviour is highly inappropriate and the effects of edge modes on the measured spectra is minimal due to the short timescales $\sim 100 \mu\text{s}$. The bandwidths required to measure these short timescales have been implemented on the ASDEX-U diagnostics[157], but such systems were unavailable during this work.

4.8 Limits on the modelling

The largest limit to the modelling discussed in this chapter was encountered in the simulation of temporal variation discussed in the previous section. This was in part due to the limited radial resolution of the Nd:YAG TS. This did not cause insurmountable difficulties; theoretical simulations made use of the ruby TS as a benchmark for the radial electron temperature and density, and the variation in time was inferred by comparing the limited Nd:YAG radial profiles with the finer ruby profile. However, in practical terms, the limit to the modelling was reached since the timescales involved in an ELM crash were orders of magnitude shorter than those measurable by the HELIOS spectrometer. Therefore, although predictions could be made, there was no way to confirm these by measurement.

The vertical TS system on ASDEX-U[158] is a more suitable configuration for measuring the time-dependent variation of plasma parameters. This system can be operated in a ‘burst mode’, which allows six measurements to be made in $\sim 2 \mu\text{s}$ and would provide good input to the GCR model on a resolution high enough to resolve detailed ELM activity. Even this relatively short timescale is around two orders of magnitude slower than those of the excitation and ionisation processes. The 3 MHz TS measurements should be compared with the 200 Hz measurements possible on MAST, as discussed in section 1.5.1.

Most of the modelling detailed in this chapter has made use of MAST shot #12245, which has accurate TS data supplemented by RP measurements in the SOL. This is an ideal arrangement for such predictive modelling, although RP measurements of MAST plasmas are not routine. In cases where accurate SOL measurements are not available, uncertainties in the edge plasma parameters can be large enough to hinder investigative use of the GCR model. A pertinent example of this is that determining the collimation of the neutral helium injection nozzle would have been impossible without RP data.

Another limit on the work, slightly disconnected from the modelling, is the collimation of the nozzle. A comparison of figures 4.14 and 4.16(b) show how the collimation of the nozzle affects the predicted contribution to the line-of-sight integrals, or viewing chords. One can see that the much narrower contribution curves of figure 4.14 lend themselves to being interpreted as local emission along the radius of the device; in contrast, the wider profiles, which were identified as those best fitting the measured data, cannot be so interpreted. A more collimated supersonic nozzle has been used with some success in the past on TEXTOR[115].

4.9 Improved deduction of N_e and T_e profiles from measured HELIOS spectra

This chapter has detailed work carried out to determine metastable population dynamics at the low-field edge of the MAST device, however, the model has taken TS and RP data as input. What remains to be determined is whether the predictive model and Levenberg–Marquardt procedure can be amalgamated to deliver radial temperature and density profiles conditional on the HELIOS measured spectra alone. The comparisons presented here are based on MAST shot #12209.

This fitting procedure differs from those discussed above, because the fitting parameters do not describe directly the measured data of interest. Rather, the parameterisation describes the radial electron density and temperature profiles which are used to compute the theoretical spectral line emission ratios as observed along the HELIOS lines-of-sight. These ratios are then compared with those obtained from the actual HELIOS measurements iteratively in a global optimisation.

Since the HELIOS spectrometer has eighteen viewing chords, the number of parameters used to represent the radial profiles had to be limited. The number of viewing chords precluded the alternative modified hyperbolic tangent parameterisation given in section 4.2 of the thesis. The number of parameters used to represent the electron temperature and density profiles was limited to ten, leaving eight degrees of freedom for the fit. These ten parameters correspond to a temperature and density parameterisation given by the original modified hyperbolic tangent function given in section 4.2.

The first stage of this study consisted of allowing all ten parameters to vary freely from their initial conditions. The most influential of these parameters, the radial position of the separatrix, was set at 1.4 m. The electron density and temperature fits obtained from the initial study are shown in figure 4.17 and the parameters are shown in table 4.1.

The functions shown in figure 4.17 are encouraging for an initial calculation, and

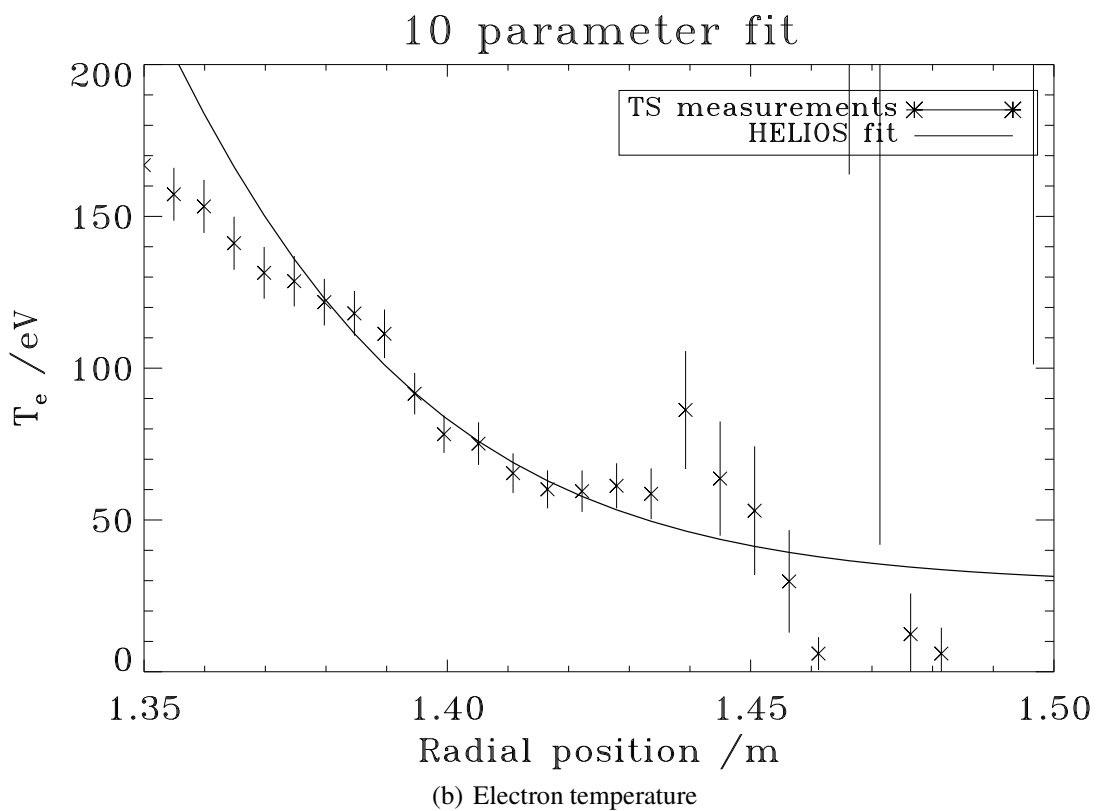
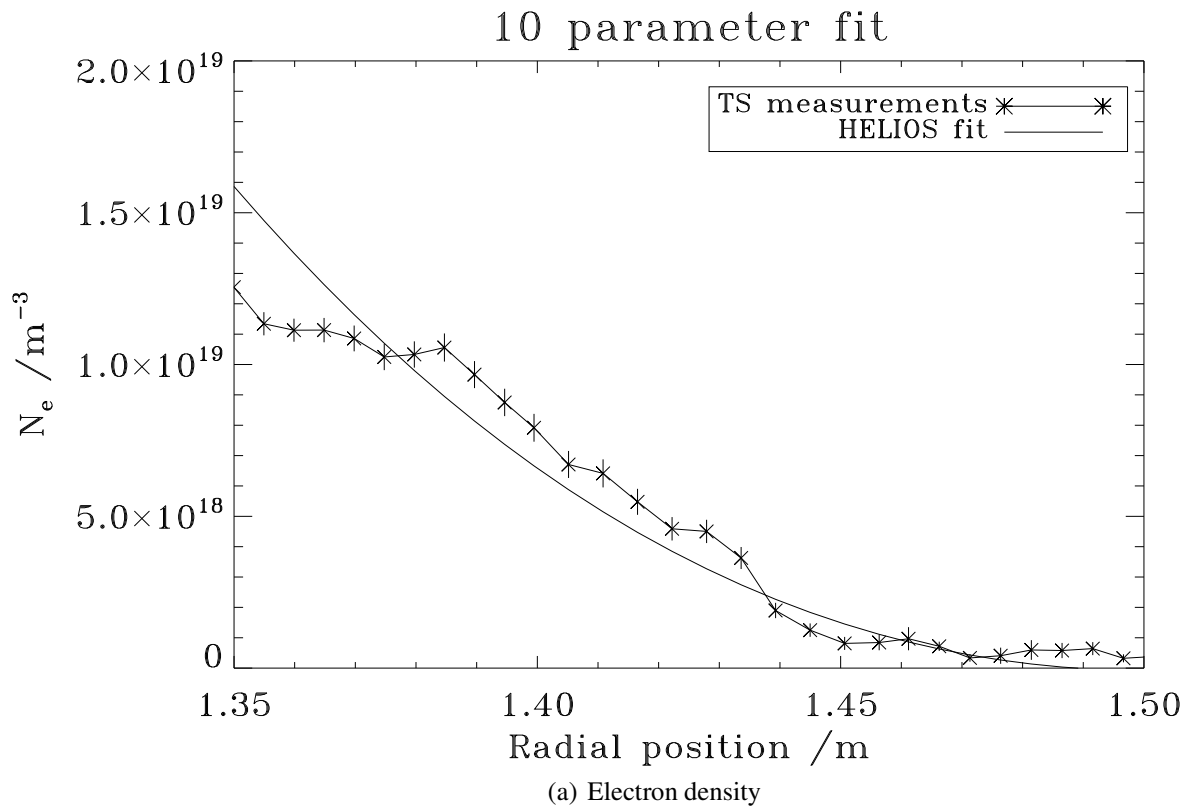


Figure 4.17: Parameterisation of the radial electron density and temperature profiles using the HELIOS-based ten-parameter fit. All of the parameters were free to vary, leading to a relatively poor representation of the profiles. The data points on the plots are the TS N_e and T_e measurements.

Parameter	Initial	Final
1	10^{18}	7.48×10^{18}
2	10^{18}	5.38×10^{11}
3	1.0	4.59
4	1.4	1.43
5	0.5	0.052
6	10^3	794.23
7	50.0	34.05
8	1.0	5.10×10^{-7}
9	1.4	1.32
10	1.0	0.030

Table 4.1: The initial and final parameters used and obtained from the first HELIOS-based predictive study.

it is evident from table 4.1 that the ten parameters are able to vary over an adequate range. The initial fit to the line ratios measured using the HELIOS spectrometer resulted in $\chi_n^2 \simeq 6.5$, which is much larger than the previous fits discussed in this chapter. As mentioned previously, the Levenberg–Marquardt procedure iterates to a local minimum of χ_n^2 , which could cause problems with fitting. It was not uncommon during this study for the fitting routine to converge on a local minimum of χ_n^2 which did not correspond to the global minimum, requiring manual input to allow the fit to continue to the global minimum, and hence the required solution. A possible solution to this problem is highlighted in section 4.10.

Although the initial investigation resulted in a reasonable representation of the radial density and temperature profiles, there were indications of where improvements could be made. Given the temperature and density profiles described the same plasma, it was considered reasonable to use the same separatrix position for both the temperature and density parameterisations. Parameter number nine in table 4.1 corresponds to the separatrix position used in the electron temperature function; it is evident that this parameter did not converge on a reasonable value, which was characteristic of the initial investigation. By implementing this change, and constraining the symmetry point of the fitting function, in this case corresponding to the separatrix position, to a reasonable range of $R_{\text{sep}} \geq 1.4$ m, the improved fit resulted in the profiles shown in figure 4.18 and the parameters given in table 4.2.

The constraints on the fitting parameters allowed the improved fit to obtain $\chi_n^2 \simeq 4.0$, substantially better than the initial study. Again, one can see from table 4.2 that the parameters are able to vary over a wide range. The most substantial difference between the two sets of fits is in the electron density profile. Figure 4.17(a) shows that

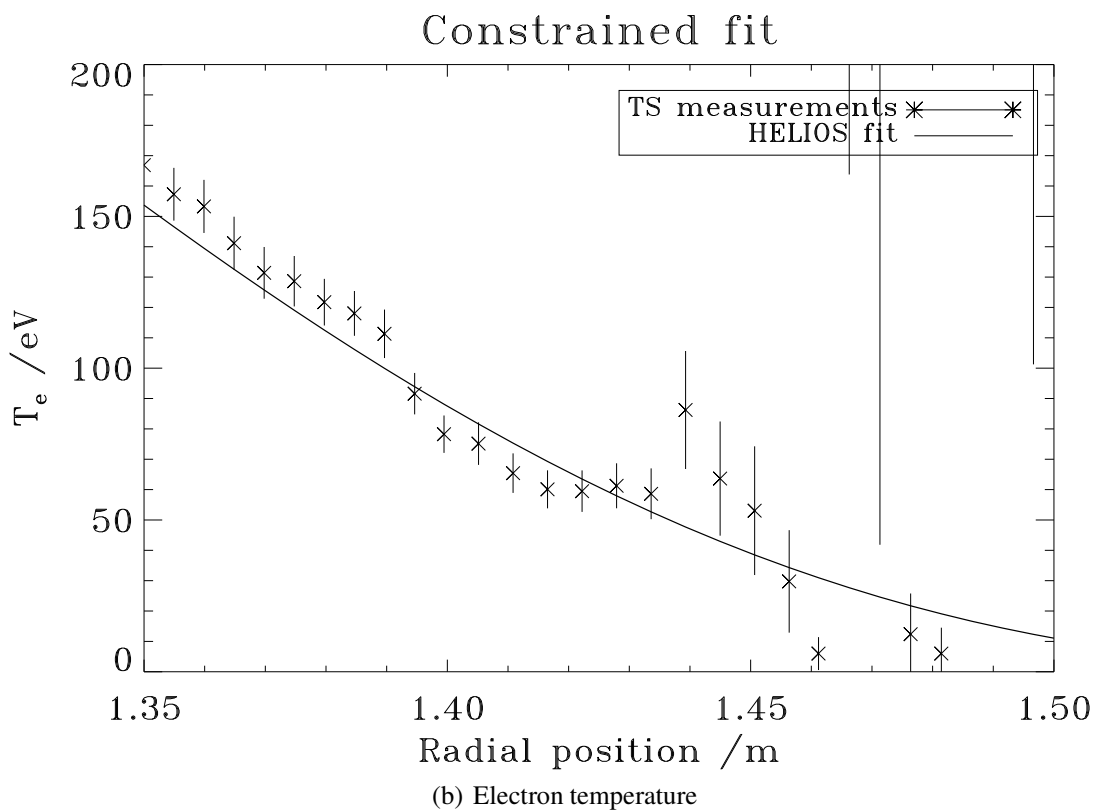
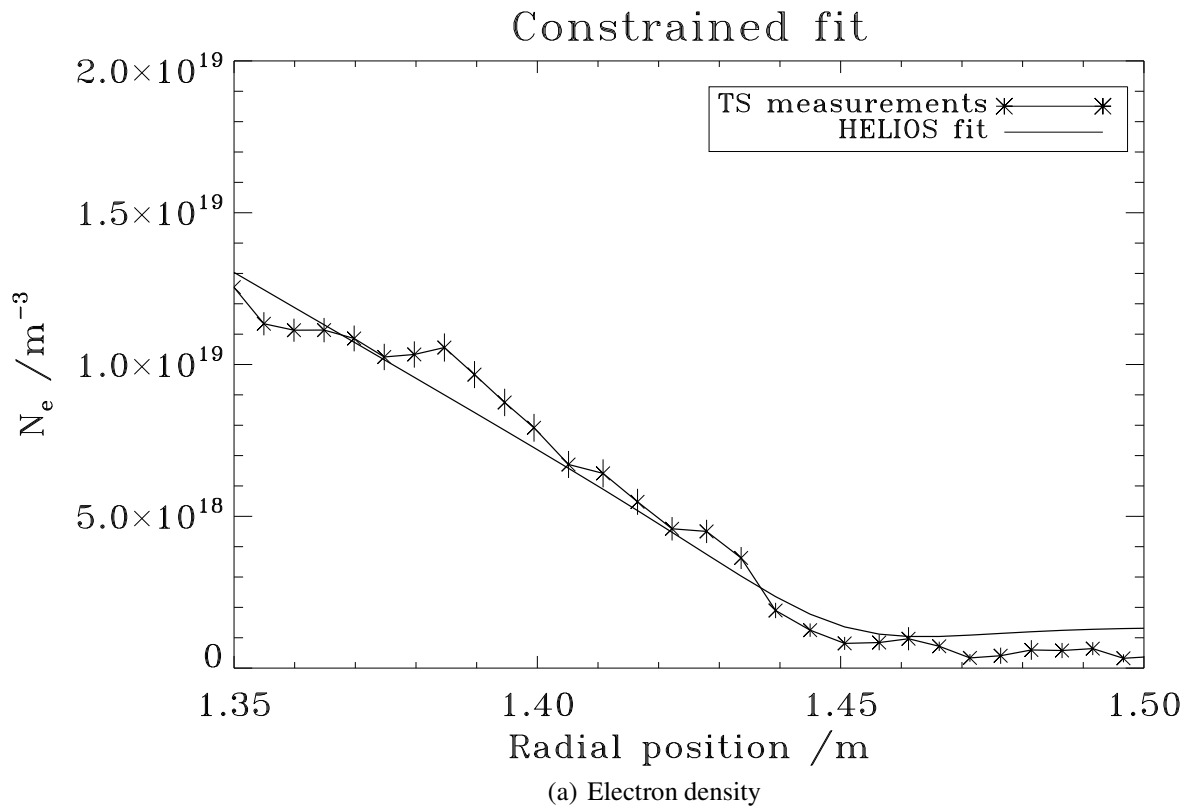


Figure 4.18: Parameterisation of the radial electron density and temperature profiles using the HELIOS-based data with constrained parameters. See text for details. These plots use an initial separatrix position of 1.4 m.

Parameter	Initial	Final
1	10^{18}	1.36×10^{18}
2	10^{18}	-1.36×10^{18}
3	1.0	778.25
4 [†]	1.4	1.45
5	0.5	0.010
6	10^3	38.53
7	50.0	-38.53
8	1.0	1.06×10^6
9 [†]	1.4	1.45
10	1.0	-0.090

[†] indicates parameters are tied.

Table 4.2: The initial and final parameters used and obtained from the constrained HELIOS-based predictive study.

the profile consists of one curve through the region of interest; this indicates that the modified hyperbolic tangent function is not being used to best effect. This is contrasted by figure 4.18(a), where the parameterisation has allowed the SOL to be fitted as a relatively constant region, with the density gradient fitted as a separate feature. Given the HELIOS measurements available, this density parameterisation is of optimal form.

Figures 4.17(b) and 4.18(b) show that the electron temperature persists as a single curve after the constraints placed on the parameters. This is not an ideal outcome since it suggests the reduction in χ_n^2 from the initial to improved study is predominantly due to the improvement in the electron density profile. Even although the form of the electron temperature function has not been improved to the same level as the density, it still compares well with the TS measurements.

This illustrates how the analysis and modelling methods outlined in this chapter can be combined to deduce the electron density and temperature radial profiles of a MAST plasma using spectral line emission ratios measured by the HELIOS spectrometer from a spatially extended gas puff without assuming equilibrium metastable population fractions. Therefore, the diagnostic sensitivity of the system and the underlying models have been substantiated given the extension to the analysis outlined in this chapter. Chapter 5 suggests further work that can be carried out in this field.

4.10 Conclusions

This chapter has summarised the work carried out in exploiting a GCR model for the metastable populations of neutral helium and the emission driven by these populations

in deduction of density/temperature radial profiles using multiple line-of-sight spectral line ratio measurements of a poorly collimated helium gas puff. There were several parts to this modelling work, with the related methods illustrated throughout this chapter. The main points of note are:

- development of a Levenberg–Marquardt algorithm to fit merged diagnostic data sets to represent the SOL;
- development of a GCR model to calculate the helium metastable populations in the vicinity of the nozzle;
- using the fundamental data discussed in chapter 2 to calculate photon emissivity coefficients for the transitions of interest;
- using these \mathcal{PEC} s to determine spatial and temporal emission profiles;
- highlight the effect of non-equilibrium metastable populations;
- development of a Monte Carlo statistical sampling simulation to determine the uncertainty associated with the metastable populations;
- estimation of the localisation of emission given TS density/temperature radial profile data;
- utilising the merged TS and RP data, the measured spectral data and the GCR model to deduce the collimation of the neutral helium injection nozzle;
- identification of nozzle damage in the neutral gas injection system;
- improved determination of radial N_e and T_e profile parameters from spectral line ratios measured using the HELIOS spectrometer.

Using the techniques developed in this chapter, spectral line emission ratios measured using the HELIOS spectrometer have been used to optimise a standard pedestal function to deliver radial electron density and temperature profiles. There was a degree of manual steering in the search for a global minimum of χ_n^2 , however, it is possible that this process could be improved in future by utilising a genetic algorithm which can determine whether the fitting procedure has converged on the global minimum of χ_n^2 . Such algorithms have been studied in optimisation procedures with some success and could be a valuable addition to this work[159].

Chapter 5

Conclusions and future work

Spectral line emission ratios measured using the HELIOS spectrometer on MAST have been analysed using a GCR emission model, allowing improved deduction of electron density and temperature radial profiles.

A state-of-the-art RMPS calculation was carried out in support of this work which resolved the resonance structure in the collision strength below the ionisation threshold[69]. The ‘interval-averaging’ technique was developed to allow the large quantity of data produced by an R -matrix calculation to be reduced to a size manageable under a database structure, such as the one which forms part of ADAS, without compromising the additional physical data provided by the resonance structure. This careful treatment of the collision strengths is particularly important when considering relatively low-temperature plasmas, such as those encountered at the edge of a tokamak.

The electron-collision excitation data for neutral helium was reappraised to produce the most reliable data set over the widest range in energy. The tabulation of collision strengths, rather than Maxwell-averaged collision strengths, was extended. Handling collision strengths has the advantage that the data are open to wider scrutiny; non-physical features such as oscillations in the collision strength due to the presence of pseudostates can be objectively analysed. One disadvantage to this tabulation in the past was the expense of computer storage necessary to archive the larger data files, which is less of an issue with current hardware.

A framework was established to estimate the uncertainty associated with a collision strength. This uncertainty was tabulated within an ADAS data format which mirrored the parent data set. These paired data provide the starting point for an uncertainty propagation analysis which can take the uncertainty on the fundamental atomic collision data, and derive the resultant uncertainty on a physical observable such as an emissivity. This work is on-going at the University of Strathclyde and JET. The result

of the reappraisal and uncertainty estimation is currently the premier electron-impact data set available for neutral helium, valid from the excitation threshold through to the asymptotic region, which should be utilised in any future work.

The electron temperature and density regime of the MAST outboard edge and the neutral gas puff system was analysed to determine the dominant physical processes. It was found that the electron-driven processes are preponderant. Furthermore, it was found that the excitation/ionisation reactions happened on a timescale far shorter than that of recombination; therefore, secondary recombination of the neutral helium need not be considered as a large emission mechanism. This quantitative evaluation of the atomic reaction processes allowed a detailed formulation of the variation of the metastable populations within the MAST edge plasma.

The detailed formulation of the neutral helium population dynamics allowed the development of a complete spatial and temporal model of the neutral helium metastable predicted populations at the plasma edge. This was extended to provide spatial and temporal resolution on the predicted emission of the three lines of diagnostic interest, given in table 3.1.

Dedicated experimental measurements were carried out on the MAST tokamak using the HELIOS experimental multi-chord spectroscopic setup, with extensive independent support diagnostics, such as TS electron density and temperature profiles, and Langmuir RP measurements. The experimental sessions provided the detailed TS and RP measurements necessary to develop the predictive GCR model, and also provided spectral emission line ratios from HELIOS used in the deduction of electron density and temperature radial profiles.

Studies were carried out on the neutral gas puff system to determine the gas throughput. This was important in both the spectral measurements, to avoid line saturation on the CCD, and in the spatial and temporal modelling to provide initial helium flux and throughput variation during the pulse. Saturation was an issue in the first phase of experiments, therefore, this was a real influence on the success of the work.

By combining the HELIOS spectral measurements with the TS and RP density and temperature radial profiles and the GCR emission model, the collimation of the neutral gas injector was deduced. This was an important result since it proved difficult to measure. The puff was found to be spatially extended beyond the approximate expected value for the collimation. It was concluded from the merging of the experimental and theoretical studies that the nozzle was damaged, resulting in a more dispersed puff.

The HELIOS spectral measurements were used within a global optimisation procedure which allowed improved deduction of electron density and temperature radial profiles from the spatially extended neutral helium gas puff independent of any non-

spectroscopic measurements. The optimisation required a degree of manual steering in the search for a global minimum of χ_n^2 , however, it is clear from the work presented in the thesis that the method of parameterising radial electron density and temperature profiles is more productive than attempting to deduce local plasma properties from individual line-of-sight measurements. This point is given prominence since successful deductions were possible supported by superior electron-impact excitation data, a complete GCR treatment of the metastable populations within a theoretical spatial and temporal emission model, in spite of a poorly collimated gas puff. The work of this thesis suggests that this is the way forward for the helium gas puff diagnostic in the general experiment.

There are some issues for future work in this field. Firstly, the manual steering of the global optimisation is not completely satisfactory for routine use of the HELIOS diagnostic. A genetic algorithm which ensures the fitting procedure has converged on the true global minimum of χ_n^2 , and hence the required solution, would be a valuable addition to this work[160]. Such algorithms have been studied in optimisation procedures with some success in a wide range of fields[161, 162]. Secondly, the success of the analysis methodologies and their application to combining spectroscopic measurements with GCR modelling are encouraging; however, further experiments with varying collimation and edge conditions would add confidence to the procedures. In particular, the MAST experiments need to be reworked with a replacement nozzle. The present study does indicate that the nozzle was damaged. Several groups have worked on more collimated systems on machines such as TEXTOR[26, 115], however, the predictive and deductive analysis framework outlined in the thesis could add to these analyses. Of particular interest would be work carried out on NSTX. A new prototype supersonic injection system is expected to improve spectral measurements significantly due to improved collimation and plasma penetration[133].

Bibliography

1. Wagner F. *et al.*, 1982. *Phys. Rev. Lett.*, **49**, 1408.
2. Meyer H. *et al.*, 2004. *Plasma Phys. Control. Fusion*, **46**, A291.
3. Peacock N.J., Robinson D.C., Forrest M.J., Wilcock P.D., Sannikov V.V., 1969. *Nature*, **224**, 488.
4. Artsimovich L.A., 1972. *J. Nucl. Fusion*, **12**, 215.
5. Wesson J., 1997. *Tokamaks*, Oxford Engineering Science Series No. 48, Clarendon Press, Oxford, 2nd edition.
6. Anderson D.T. & Garabedian P.R., 1994. *J. Nucl. Fusion*, **34**, 881.
7. Peng Y-K.M. & Strickler D.J., 1986. *J. Nucl. Fusion*, **26**, 769.
8. ITER website.
<http://www.iter.org>
9. Sykes A., 2001. *Plasma Phys. Control. Fusion*, **43**, A127.
10. Sykes A. *et al.*, 2001. *J. Nucl. Fusion*, **41**, 1423.
11. Lloyd B. *et al.*, 2004. *Plasma Phys. Control. Fusion*, **46**, B477.
12. The JET Team, 1995. *Plasma Phys. Control. Fusion*, **37**, A227.
13. Belo P. *et al.*, 2004. *Plasma Phys. Control. Fusion*, **46**, 1299.
14. Walsh M.J. *et al.*, 2003. *Rev. Sci. Instrum.*, **74**, 1663.
15. Connor J.W., 1998. *Plasma Phys. Control. Fusion*, **40**, 191.
16. Connor J.W., 1998. *Plasma Phys. Control. Fusion*, **40**, 531.
17. Suttrop W., 2000. *Plasma Phys. Control. Fusion*, **42**, A1.
18. Zohm H., 1996. *Plasma Phys. Control. Fusion*, **38**, 105.
19. Matsumoto H., 1992. *Plasma Phys. Control. Fusion*, **34**, 615.
20. ITER physics basis, 1999. *J. Nucl. Fusion*, **39**, 2391.
21. Rognlien T.D., 2005. *Plasma Phys. Control. Fusion*, **47**, A283.
22. The ASDEX team, 1989. *J. Nucl. Fusion*, **29**, 1959.
23. Field A.R. *et al.*, 2002. *Plasma Phys. Control. Fusion*, **44**, A113.
24. Burrell K.H. *et al.*, 1989. *Plasma Phys. Control. Fusion*, **31**, 1649.
25. Stewart D.T. & Gabathuler E., 1959. *Proc. Roy. Soc.*, **74**, 473.
26. Brix M., 1998. "Messung von Electronentemperatur und -dichte mittels Heliumstrahl-diagnostik im Randschichtplasma eines Tokamak". Ph.D thesis, Ruhr-Universität Bochum.
27. Bryans P., O'Mullane M.G., Paton I.D., Summers H.P., Torney M., Whiteford A.D., Bingham R., Kellet B., 2005. *Plasma Phys. Control. Fusion*– submitted.
28. Crothers D.S.F. & McCann J.F., 1983. *J. Phys. B: At. Mol. Phys.*, **16**, 3229.
29. Summers H.P. & Hooper M.B., 1983. *Plasma Physics*, **25**, 1311.
30. de Heer F.J., Hoekstra R., Summers H.P., 1992. *Atomic & plasma–material interaction data for fusion*, **3**, 47.
31. Burgess A. & Tully J.A., 1992. *Astron. Astrophys.*, **254**, 436.
32. Summers H.P., Dickson W.J., O'Mullane M.G., Badnell N.R., Whiteford A.D., Brooks D.H., Lang J., Loch S.D., Griffin D.C., 2005. *Plasma Phys. Control. Fusion*– submitted.
33. Field A.R., Carloan P.G., Conway N.J., O'Mullane M.G., 1999. *Rev. Sci. Instrum.*, **70**, 355.

34. Condon E.U. & Shortley G.H., 1951. *The theory of atomic spectra*, Cambridge University Press.
35. Andrew Y., 1999. "Development and application of a thermal helium diagnostic for the JET divertor plasma". Ph.D thesis, University of London.
36. Schweer B., Mank G., Pospieczczyk A., 1992. *J. Nucl. Mater.*, **196–198**, 174.
37. Behrendt H. *et al.*, 1997. *J. Nucl. Mater.*, **241–243**, 426.
38. Davies S.J. *et al.*, 1997. *J. Nucl. Mater.*, **241–243**, 426.
39. Fielding S.J. *et al.*, 1996. *Plasma Phys. Control. Fusion*, **38**, 1091.
40. Carolan P.G. *et al.*, 2001. *Rev. Sci. Instrum.*, **72**, 881.
41. Jones P., 2003. "An experimental investigation into tokamak edge MHD behaviour". Ph.D thesis, University of London.
42. Hutchinson I.H., 1987. *Principles of plasma diagnostics*. Cambridge University Press.
43. Arends E., 2003. "Density gradients in spherical tokamak plasmas". Ph.D thesis, Technische Universiteit Eindhoven.
44. Shafranov V.D., 1958. *Sov. Phys. JETP*, **6**, 545.
45. Komori A. *et al.*, 1988. *J. Nucl. Fusion*, **28**, 1460.
46. Huber A., Samm U., Schweer B., Mertens Ph., 2005. *Plasma Phys. Control. Fusion*, **47**, 409.
47. McCormick K., 1985. *Rev. Sci. Instrum.*, **56**, 1063.
48. Schweinzer J. *et al.*, 1992. *Plasma Phys. Control. Fusion*, **34**, 1173.
49. Aumayr F. *et al.*, 1992. *J. Nucl. Mater.*, **196–198**, 928.
50. Schweinzer J., Wutte D., Winter H.P., 1994. *J. Phys. B: At. Mol. Opt. Phys.*, **27**, 137.
51. National Institute of Standards and Technology, 2004. *Ground levels and ionization energies for the neutral atoms*. <http://physics.nist.gov>.
52. Zweben S.J. & Gould R.W., 1985. *J. Nucl. Fusion*, **25**, 171.
53. Endler M. *et al.*, 1995. *J. Nucl. Fusion*, **35**, 1307.
54. Endler M. *et al.*, 1995. *Phys. Scr.*, **51**, 610.
55. Zoletnik S. *et al.*, 1998. *Plasma Phys. Control. Fusion*, **40**, 1399.
56. Summers H.P., 2004. *ADAS user manual ver. 2.6*. <http://adas.phys.strath.ac.uk>.
57. Hebb M.H. & Menzel D.H., 1940. *ApJ.*, **92**, 408.
58. Seaton M.J., 1953. *Proc. Roy. Soc.*, **A218**, 400.
59. Seaton M.J., 1955. *Proc. Roy. Soc.*, **A231**, 37.
60. Corrigan S.J.B. & von Engel A, 1958. *Proc. Roy. Soc.*, **72**, 786.
61. Dalgarno A. & Kingston A.E., 1958. *Proc. Roy. Soc.*, **72**, 1053.
62. Burke P.G. & Berrington K.A., 1993. *Atomic and molecular processes: An R-matrix approach*. Institute of Physics publishing.
63. Burke P.G. & Robb W.D., 1972. *J. Phys. B: At. Mol. Phys.*, **5**, 44.
64. Berrington K.A., Burke P.G., Sinfailam A.L., 1975. *J. Phys. B: At. Mol. Phys.*, **8**, 1459.
65. Gorczyca T.W. & Badnell N.R., 1997. *J. Phys. B: At. Mol. Opt. Phys.*, **30**, 3897.
66. Badnell N.R., 1984. *J. Phys. B: At. Mol. Phys.*, **18**, 955.
67. Berrington K.A. *et al.*, 1985. *J. Phys. B: At. Mol. Phys.*, **18**, 4135.
68. Bartschat K., 1998. *J. Phys. B: At. Mol. Opt. Phys.*, **31**, L469.
69. Ballance C.P., 2003. *Private communication*.
70. Igual-Ruiz N. *et al.*, 2001. *J. Phys. B: At. Mol. Opt. Phys.*, **34**, 2289.
71. Delahaye F. *et al.*, 2004. *J. Phys. B: At. Mol. Opt. Phys.*, **37**, 2585.
72. Massey H.S.W. & Mohr C.B.O., 1932. *Proc. Roy. Soc.*, **A136**, 289.
73. Gorczyca T.W., Badnell N.R., Griffin D.C., Mitnik D.M., Pindzola M.S., 2000. *Atomic data needs for x-ray astronomy*, 97. <http://heasarc.gsfc.nasa.gov>.
74. Castillejo L., Percival I.C., Seaton M.J., 1960. *Proc. Roy. Soc.*, **A254**, 259.
75. Rotenburg M., 1962. *Ann. Phys. N. Y.*, **19**, 262.

76. Burke P.G., Gallaher D.F., Geltman S., 1969. *J. Phys. B: At. Mol. Phys.*, **2**, 1142.
77. Scott M.P. *et al.*, 1989. *J. Phys. B: At. Mol. Opt. Phys.*, **22**, 3055.
78. Bray I. & Stelbovics A.T., 1992. *Phys. Rev. A.*, **46**, 6995.
79. Bray I. & Stelbovics A.T., 1993. *Phys. Rev. Lett.*, **70**, 746.
80. Berrington A.K., Eissner W.B., Norrington P.H., 1995. *Comput. Phys. Commun.*, **92**, 290.
81. Bartschat K., 1996. *Phys. Rev. A.*, **54**, 998.
82. Bartschat K., 1998. *Comput. Phys. Commun.*, **114**, 168.
83. Bautista M.A., 2000. *Atomic data needs for x-ray astronomy*, 97. <http://heasarc.gsfc.nasa.gov>.
84. Burke P.G., Hibbert A., Robb W.D., 1971. *J. Phys. B: At. Mol. Phys.*, **4**, 153.
85. Burke P.G. & Robb W.D., 1975. *Adv. Atom. Mol. Phys.*, **11**, 143.
86. Bloch C., 1957. *Nucl. Phys.*, **4**, 503.
87. Lane A.M. & Robson D., 1966. *Phys. Rev.*, **151**, 774.
88. Whiteford A.D., Smith R., Witthoef M.C., Badnell N.R., Paton I.D., O'Mullane M.G., Summers H.P., 2005. *J. Phys. B: At. Mol. Opt. Phys.*—in preparation.
89. Badnell N.R., Griffin D.C., Gorczyca T.W. & Pindzola M.S., 1993. *Phys. Rev. A.*, **48**, R2519.
90. Pradhan A.K., 1983. *Phys. Rev. A.*, **28**, 2113.
91. Pradhan A.K., 1983. *Phys. Rev. A.*, **28**, 2128.
92. Summers H.P. *et al.*, 2002. *Plasma Phys. Control. Fusion*, **44**, B323.
93. Whiteford A.D. *et al.*, 2002. *J. Phys. B: At. Mol. Opt. Phys.*, **35**, 3729.
94. Whiteford A.D., 2004. “*On the spectral emission of impurity species for diagnostic application to magnetically confined fusion plasmas*”. Ph.D thesis, University of Strathclyde.
95. Krüken T. *et al.*, 2004. *J. Phys. D: Appl. Phys.*, **37**, 3213.
96. Savin D.W. *et al.*, 2002. *ApJ.*, **576**, 1098.
97. Paton I.D., Summers H.P., Field A.R., 2005. *Modelling neutral helium in the MAST device*. In preparation.
98. Bethe H., 1930. *Ann. Phys., Lpz.*, **5**, 325.
99. Mott N.F. & Massey H.S.W., 1965. *The theory of atomic collisions*. Clarendon Press, Oxford.
100. Burgess A. & Tully J.A., 1978. *J. Phys. B: At. Mol. Phys.*, **11**, 4271.
101. Ochkur V.I., 1964. *Sov. Phys. JETP*, **18**, 503.
102. Bryans P., 2005. “*On the spectral emission of non-Maxwellian plasmas*”. Ph.D thesis, University of Strathclyde.
103. de Heer F.J., 1998. *IAEA nuclear data section report INDC(NDS)-385*.
104. Ralchenko Yu V. *et al.*, 2000. *NIFS report NIFS-DATA-59*.
105. Brooks D.H. *et al.*, 1999. *Astron. Astrophys.*, **347**, 277.
106. Badnell N.R. *et al.*, 2004. *J. Phys. B: At. Mol. Opt. Phys.*, **37**, 4589.
107. Neu R. *et al.*, 2005. *J. Nucl. Fusion*, **45**, 209.
108. International Atomic Energy Authority website. <http://www.iaea.org>
109. Brezinsek S. *et al.*, 2005. *Plasma Phys. Control. Fusion*, **47**, 615.
110. Zastrow K.-D. *et al.*, 2005. *J. Nucl. Fusion*, **45**, 163.
111. Bakhtiari M. *et al.*, 2005. *J. Nucl. Fusion*, **45**, 318.
112. Bhatia A.K., 2000. *Atomic data needs for x-ray astronomy*, 41. <http://heasarc.gsfc.nasa.gov>
113. Summers H.P., 2004. *Private communication*.
114. Valovič M. *et al.*, 2002. *Plasma Phys. Control. Fusion*, **44**, A175.
115. Schweer B., Brix M., Lehnen M., 1999. *J. Nucl. Mater.*, **266–269**, 673.
116. Lehnen M. *et al.*, 2003. *J. Nucl. Fusion*, **43**, 168.
117. Faber T.E., 1995. *Fluid dynamics for physicists*. Cambridge University Press.
118. Berman A., 1992. *Vacuum engineering calculations, formulas and solved exercises*. Academic Press.
119. Field A.R., 2005. *Private communication*.

120. Sears F.W. & Salinger G.L., 1975. *Thermodynamics, kinetic theory & statistical thermodynamics*. Addison-Wesley Publishing Company.
121. Knudsen M., 1910. *Ann. Phys.*, **31**, 205.
122. Akers R.J. *et al.*, 2002. *J. Nucl. Fusion*, **42**, 122.
123. Conway N.J., 1998. "Study of ion behaviour on tokamaks using active and passive doppler spectroscopy". Ph.D thesis, University College, Dublin.
124. Lao L.L., 2004. *EFIT manual*. <http://fusion.gat.com/efit>, General Atomics.
125. Walsh M.J. *et al.*, 1999. *Rev. Sci. Instrum.*, **70**, 742.
126. Walsh M.J. *et al.*, 2004. *Rev. Sci. Instrum.*, **75**, 3909.
127. Porcelli F. *et al.*, 1996. *Plasma Phys. Control. Fusion*, **38**, 2163.
128. Mück A. *et al.*, 2002. *29th EPS Conf. on Plasma Phys. Control. Fusion (Montreux, Switzerland)*, **26B**, P-1.037.
129. Zohm H. *et al.*, 2003. *J. Nucl. Fusion*, **43**, 1570.
130. Mück A. *et al.*, 2005. *Plasma Phys. Control. Fusion*, **47**, 1633.
131. Pitcher C.S. *et al.*, 2000. *Meeting of the American Physical Society (Québec City, Canada)*, session UP1, poster session IX.
132. Carolan P.G., 2004. *Private communication*.
133. Soukhanovskii V.A. *et al.*, 2004. *Rev. Sci. Instrum.*, **75**, 4320.
134. Lao L.L., St John H., Stambaugh R.D., 1985. *J. Nucl. Fusion*, **25**, 1611.
135. Conway N.J. *et al.*, 1997. *Rev. Sci. Instrum.*, **68**, 1015.
136. Meyer H. *et al.*, 2000. *Czech. J. Phys.*, **50**, 1451.
137. Counsell G., 2005. *Private communication*.
138. Butterworth S., 1930. *Wireless engineer*, **7**, 536.
139. Horton L.D. *et al.*, 2002. *Plasma Phys. Control. Fusion*, **44**, A273.
140. Thomsen K. *et al.*, 2002. *Plasma Phys. Control. Fusion*, **44**, A429.
141. Groebner R.J. & Carlstrom T.N., 1998. *Plasma Phys. Control. Fusion*, **40**, 673.
142. Horton L.D., 2005. *Private communication*.
143. Marquardt D.W., 1963. *J. Soc. Ind. App. Math.*, **11**, 431.
144. Coulibaly I. & Lécot C., 1999. *Math. Comput.*, **68**, 651.
145. Hawkins K., 2004. *Private communication*.
146. Abramowitz M. & Stegun I.A., 1964. *Handbook of mathematical functions*. Dover publications.
147. Kirk A. *et al.*, 2004. *Phys. Rev. Lett.*, **92**, 245002.
148. Eich T. *et al.*, 2003. *Phys. Rev. Lett.*, **91**, 195003.
149. Kirk A. *et al.*, 2005. *Plasma Phys. Control. Fusion*, **47**, 995.
150. Boedo J.A. *et al.*, 2004. *30th EPS Conf. on Plasma Phys. Control. Fusion (London, UK)*, **28G**.
151. Counsell G. *et al.*, 2002. *Plasma Phys. Control. Fusion*, **44**, 827.
152. Kirk A. *et al.*, 2004. *Plasma Phys. Control. Fusion*, **46**, 551.
153. Müller H.W. *et al.*, 2002. *29th EPS Conf. on Plasma Phys. Control. Fusion (Montreux, Switzerland)*, **26B**.
154. Bobkov V., 2003. *IPP Garching Report*, IPP 4/282.
155. Herrmann A. *et al.*, 2004. *Plasma Phys. Control. Fusion*, **46**, 971.
156. Horton L.D. *et al.*, 2005. *J. Nucl. Fusion*, **45**, 856.
157. Kurzan B. *et al.*, 2005. *Phys. Rev. Lett.*, **95**, 145001.
158. Murmann H. *et al.*, 1992. *Rev. Sci. Instrum.*, **63**, 4941.
159. Ulyanekov A., Sobolewski S., 2005. *J. Phys. D: Appl. Phys.*, **38**, A235.
160. Haupt R.L. & Haupt S.E., 1997. *Practical genetic algorithms*. Wiley-Interscience.
161. Dane A.D. *et al.*, 1998. *Physica B*, **253**, 254.
162. Wormington M. *et al.*, 1999. *Phil. Trans. R. Soc.*, **A357**, 2827.